Development and experimental validation of adaptive conformal particle therapy

Entwicklung und experimentelle Validierung adaptiver, konformaler Ionenstrahltherapie
Zur Erlangung des Grades eines Doktors der Naturwissenschaften (Dr. rer. nat.)
Genehmigte Dissertation von Timo Steinsberger aus Esslingen am Neckar
Tag der Einreichung: 5. Mai 2022, Tag der Prüfung: 20. Juni 2022

1. Gutachten: Prof. Dr. Marco Durante
2. Gutachten: Prof. Dr. Marco Riboldi
Darmstadt, Technische Universität Darmstadt

TECHNISCHE UNIVERSITÄT DARMSTADT

Physics Department

GSI Helmholtzzentrum für Schwerionenforschung

Medizinphysik

Development and experimental validation of adaptive conformal particle therapy
Entwicklung und experimentelle Validierung adaptiver, konformaler Ionenstrahltherapie

Accepted doctoral thesis by Timo Steinsberger

Date of submission: 5th May 2022
Date of thesis defense: 20th June 2022

Darmstadt, Technische Universität Darmstadt

For my parents, my brother and my sister

Abstract

In radiotherapy, conforming the high dose to the tumor is of special importance to avoid toxicity in critical organs. Scanned ion beam therapy has shown its potential to reduce the dose in the healthy tissue. However, its application is limited for thoracic and abdominal tumors like lung, liver or pancreatic cancer. In those organs, respiratory motion induces considerable changes in tumor position and beam range to the tumor. In current clinical practice, this causes severe dose degradations and necessitates large safety margins that invalidate the conformity gain of ion beam therapy. In order to minimize target margins, the motion has to be compensated by real-time adaptive beam delivery. A major challenge are the irregularities of realistic tumor motion that are unknown during treatment planning.

To study the impact of irregular motion, an extension of an RBE-weighted dose calculation algorithm enabling the computation on arbitrarily long series of CT images was experimentally validated. A workflow for simulation studies with irregular motion data for the assessment of plan robustness and treatment quality was presented.

A new motion mitigation technique denoted as multi-phase 4D dose delivery with residual tracking (MP4DRT) was implemented into the research version of a clinical dose delivery system. It combines the earlier proposed multi-phase 4D dose delivery (MP4D) technique with lateral beam tracking. MP4D synchronizes the delivery of phase specific treatment plans with the observed motion. It therefore enables conformal, time-resolved 4D treatment planning for periodic motion. It considers range changes and deformations during the optimization process and therefore removes the need for real-time range adjustments. In the new technique, additional lateral beam tracking adapts beam positions in real-time to the unexpected residual component of the observed irregular motion.

The potential of MP4DRT was evaluated in a comparative experimental study that included also the other free breathing motion mitigation techniques MP4D, lateral beam tracking and ITV rescanning. Treatment plans were optimized for a digital anthropomorphic lung phantom with a nominal tumor motion amplitude of 20 mm. The plans were delivered at a clinical carbon ion therapy facility to a quality assurance like setup performing regular and irregular motion scenarios including 25 % amplitude variations with and without baseline drift. Treatment quality was assessed using detector measurements and log-file based dose reconstructions. The robustness of the delivery was tested by adding artificial errors to the motion signal during the delivery and rotational tumor motion up to 30° during dose reconstruction.

It was demonstrated that MP4DRT is able to deliver highly conformal dose distributions. A target coverage of D95 > 95 % was achieved irrespective of the motion scenario and rotation amplitude, and for clinically relevant mean absolute tracking errors of the motion monitoring up to 1.9 mm. MP4DRT synergized the complementary strengths of its predecessors and outperformed all other compared motion mitigation techniques in target coverage, dose conformity and homogeneity, organ at risk sparing, and robustness against rotational motion.

MP4DRT can deliver conformal and homogeneous dose distributions to moving tumors in a single fraction. After clinical implementation, it therefore might improve treatment quality and enable the treatment of tumors so far unavailable for particle therapy.

Zusammenfassung

Ziel der Strahlentherapie ist es, das Hochdosisvolumen auf den Tumor zu beschränken, um Toxizität in umliegenden Organen zu verhindern. Gescannte Ionenstrahltherapie kann die Dosis in gesundem Gewebe reduzieren. Ihr Einsatz gegen Tumore in Brustkorb und Unterleib, etwa Krebs in Lunge, Leber und Bauchspeicheldrüse, ist bisher allerdings nur eingeschränkt möglich. Durch die Atmung induzierte Veränderungen in Tumorposition und Strahlreichweite sorgen in der klinischen Praxis für deutlich schlechtere Dosisverteilungen und erfordern große Sicherheitssäume, die den Gewinn an Konformität durch Ionenstrahltherapie reduzieren. Um Sicherheitssäume zu mimimieren, muss sich die Bestrahlung in Echtzeit an die anatomische Bewegung anpassen. Dies wird durch die bei der Bestrahlungsplanung unbekannten Unregelmäßigkeiten realistischer Tumorbewegung erschwert.
Um den Einfluss unregelmäßiger Bewegung zu untersuchen, wurde eine Erweiterung eines RBE-gewichteten Dosisberechnungsalgorithmus experimentell validiert, die den Umgang mit beliebig langen Serien von CT-Bildern ermöglicht. Es wurde gezeigt, wie damit eine Simulationsstudie mit unregelmäßigen Patientenbildgebungsdaten durchgeführt werden kann.
Eine neue Methode zur Bewegungskompensation, die Mehrphasen 4D Bestrahlung mit residuellem Tracking (MP4DRT), wurde in die Forschungsversion eines klinischen Bestrahlungssteuerungssystems implementiert. Sie kombiniert die zuvor vorgeschlagene mehrphasen 4D Bestrahlung (MP4D) mit lateralem Beam Tracking. Die MP4D synchronisiert die Abstrahlung phasenspezifischer Pläne mit der beobachteten Bewegung. Dies ermöglicht eine zeitaufgelöste, konformale Bestrahlungsplanung für periodische Bewegungen, die Reichweitenänderungen und Verformungen berücksichtigt. Eine Echtzeitanpassung der Reichweite während der Bestrahlung ist daher nicht notwendig. In der neuen MP4DRT führt zusätzliches laterales Beam Tracking die Strahlposition in Echtzeit der unerwarteten Bewegungskomponente nach.
MP4DRT wurde in einer experimentellen Studie mit den ebenfalls für freie Atmung entwickelten Bewegungskompensationsmethoden MP4D, lateralem Beam Tracking und ITV Rescanning verglichen. Bestrahlungspläne wurden für ein digitales Lungenphantom mit einer nominellen Tumorbewegungsamplitude von 20 mm optimiert. Mit Qualitätssicherungsmessungen vergleichbare Experimente wurden an einer klinischen Kohlenstofftherapieanlage durchgeführt, wobei periodische und unregelmäßige Bewegungen mit 25 % Amplitudenvariation mit und ohne Drift der Basislinie untersucht wurden. Die Qualität der Bestrahlung wurde mittels Detektormessungen und Logfile-basierten Dosisrekonstruktionen quantifiziert. Die Robustheit der Methode wurde durch künstliche Fehler des Bewegungssignals während der Bestrahlung und zusätzliche Rotationen um bis zu 30° während der Dosisrekonstruktion getestet.
Es wurde gezeigt, dass MP4DRT hochkonformale und homogene Dosisverteilungen applizieren kann. Eine Zielabdeckung von D95>95 % wurde unabhängig vom Bewegungsszenario oder der Tumorration und für klinisch relevante mittlere absolute Bewegungsdetektionsfehler von bis zu 1.9 mm erreicht. Die MP4DRT verbindet die komplementären Stärken seiner Vorgänger und übertrifft die verglichenen Bewegungkompensationstechniken in Zielabdeckung, Dosiskonformalität und -homogenität, der Schonung von Risikoorganen und der Robustheit gegen Rotationsbewegungen.
Die MP4DRT ermöglicht die Applikation konformaler und homogener Dosisverteilungen in bewegten Tumoren in einer einzigen Fraktion. Nach einer klinischen Implementierung könnte dies die Bestrahlungsqualität verbessern und Behandlung bisher für die Teilchentherapie unzugänglicher Tumore ermöglichen.

Contents

List of abbreviations

AP	anterior-posterior	62
BSR	breath-sampled rescanning	61
CBCT	cone beam computed tomography	20
CC	cranio-caudal	18
CNAO	Centro Nazionale di Adroterapia Oncologica, Pavia, Italy	25
COM	center-of-mass	24
CPU	central processing unit	48
CT	computed tomography	20
CTV	clinical target volume	15
DDD	dose delivery data	48
DDS	dose delivery system	15
DIO	digital input/output	52
DIR	deformable image registration	43
DMA	direct memory access	48
DNA	deoxyribonucleic acid	10
DRAM	dynamic random access memory	49
DVH	dose-volume histogram	69
FPGA	field programmable gate array	48
GSI	GSI Helmholtzzentrum for Heavy Ion Research, Darmstadt, Germany	24
GTV	gross tumor volume	15
HU	Hounsfield units	20
IC	ionization chamber	47
IES	iso-energy slice	14
IMPT	intensity modulated particle therapy	16
IMRT	intensity modulated radiotherapy	16
ITV	internal target volume	16
LEM	local effect model	12
LET	linear energy transfer	8
MMD	motion mitigation data	49
MP4D	multi-phase 4D dose delivery	5

MP4DRT	multi-phase 4D dose delivery with residual tracking	44
MFUD	multi field uniform dose	16
MRI	magnetic resonance imaging	20
NSCLC	non-small cell lung cancer	1
NTCP	normal tissue complication probability	16
OAR	organ at risk	16
P2P	peer-to-peer FIFO	52
PCA	principle component analysis	43
PCR	phase-controlled rescanning	61
PET	positron emission tomography	21
PSI	Paul Scherrer Institute, Villigen, Switzerland	24
PTV	planning tumor volume	16
PXIe	peripheral component interconnect eXtensions express	48
QA	quality assurance	15
RBE	relative biological effectiveness	12
RFKO	radiofrequency knock-out	50
RMS	root-mean-square	53
ROI	region of interest	54
ROS	reactive oxygen species	10
SBRT	stereotactic body radiation therapy	16
SFUD	single field uniform dose	16
SOBP	spread-out Bragg peak	14
US	ultrasound	21
WEPL	water-equivalent path length	8
XCAT	4D extendended cardiac-thorso phantom	62

1 Motivation and scope of this work

1.1 Cancers affected by anatomical motion

Cancer is one of the main reasons of death in Germany and world wide. In 2016, 721,870 cancer incidences were diagnosed in Germany and 230,725 humans died from it [1]. As illustrated in figure 1.1, lung cancer was the second most abundant cancer for men and the third most abundant among women, but it was by far the one with the highest mortality. In 2016, 16,481 women and 29,324 men in Germany died because of lung cancer.

Lung cancers are subdivided into small and non-small cell lung cancers because of their difference in prognosis and treatment options. Quickly growing and metastatic tumors, for example the extremely deadly small cell lung cancer (SCLC), are most often treated with systemic therapies like chemotherapy. They target tumor cells based on particularities of their metabolism, for example high cell division rates. Systemic therapies act in the entire body. As cell division or other targeted biological processes are not restricted to tumor cells, this kind of therapy can cause severe side effects. On the other hand, if for specific cancers a unique pathway has been identified, chemotherapy can be highly specific, successful and relatively free of side effects.

About 80 % of all diagnosed lung cancers are non-small cell lung cancer (NSCLC) [2]. This cancer type is mainly treated with surgery and radiotherapy. These are local therapies targeting specific, spatially restricted lesions such as the primary tumor. This makes local therapies being the first choice for cancers that did not show metastatic spread, or are known to show little tendency to spread at the stage of diagnosis. The progression of lung cancers is staged based on tumor size, regional lymph node involvement and the presence of metastasis [3] in order to predict patient prognosis and select the appropriate therapy. In about half of the cases, lung cancer is diagnosed in stage IV (men 52 %, women 53 %), in which the tumor already formed metastasis [1]. As illustrated in figure 1.2, this leads to a poor prognosis. Thanks to the applicability of local therapies, NSCLC up to stage III has a significantly better survival rate.

In many cases, the tumor is not accessible for surgery or it cannot be removed entirely. Possible reasons are an attachment of the tumor to critical organs or intolerable side effects of the surgery. In this case, radiotherapy is the only option. In radiotherapy, tumor cells are sterilized or killed by ionizing radiation. The most commonly applied type of radiation is photons, but also treatments with charged particles like electrons and ions are possible. The higher the radiation dose, the more likely is a tumor control. At the same time, the risk of side effects in healthy tissue around the tumor increases. For lung cancer, especially the healthy lung, heart and esophagus have shown to be critical organs at risk. Consequently, it is necessary for dose escalation to constrain the dose distribution as much as possible to the tumor volume. A recent randomized clinical trial underlined that the dose escalation in radiotherapy of NSCLC is currently limited by toxicity to surrounding tissue [4].

Even though less abundant, also other cancers affected by organ motion, such as liver or pancreatic cancer have a poor prognosis. In Germany, liver cancer shows a 5 year survival rate of only 13 % for women and 12 % for men. For pancreatic cancers, the 5 year survival is only 8 % for both sexes [1]. A common challenge in radiotherapy of lung, liver and pancreatic cancers is that they are moving due to respiration.

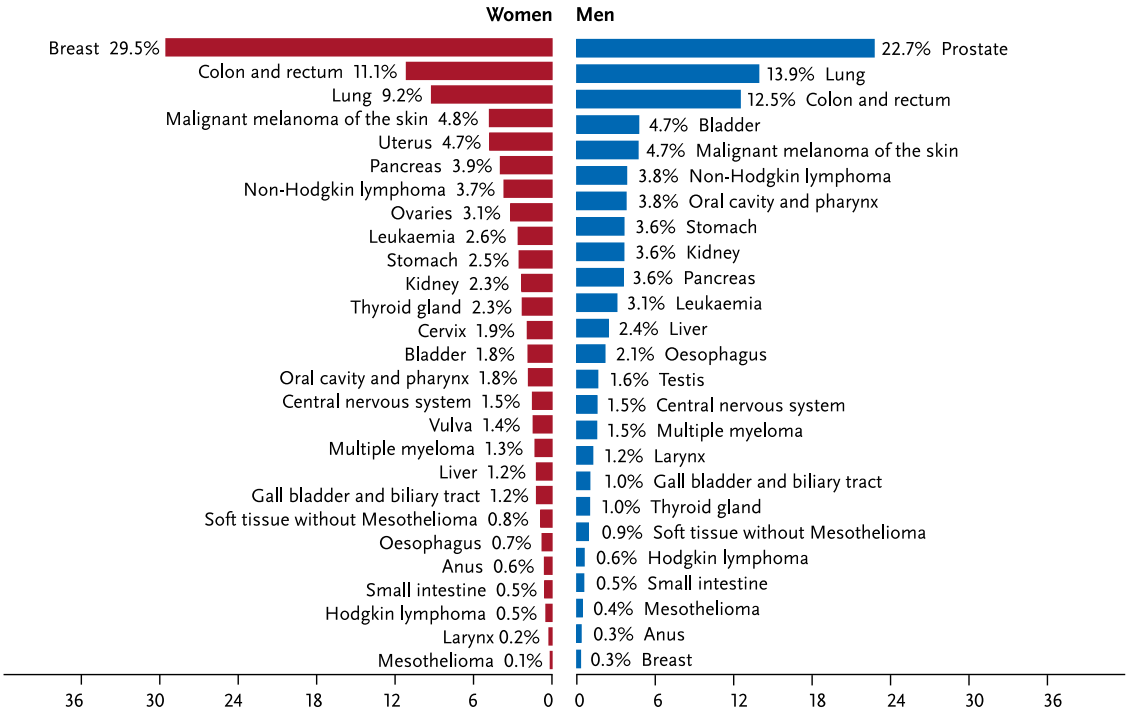

(a) Cancer incidence

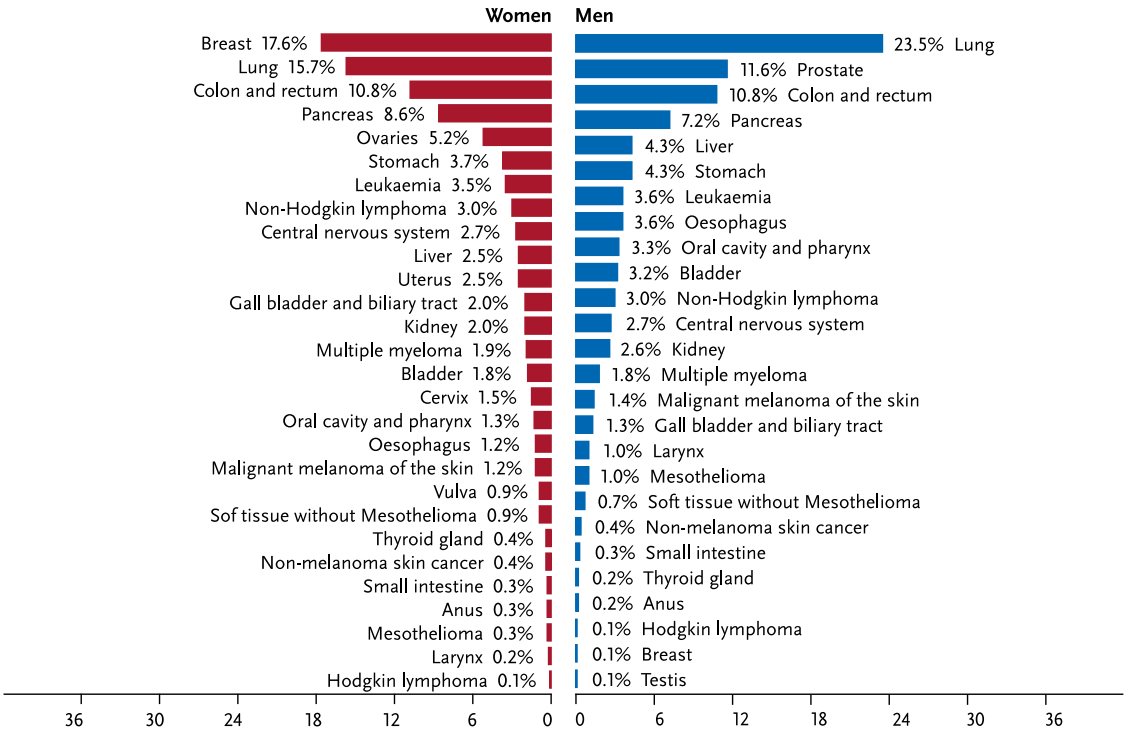

(b) Cancer deaths

Figure 1.1: Fraction of different cancer sites of the (a) total cancer incidence and (b) cancer deaths in Germany 2015/16. Figures from [1]. ©German Centre for Cancer Registry Data at the Robert Koch Institute.

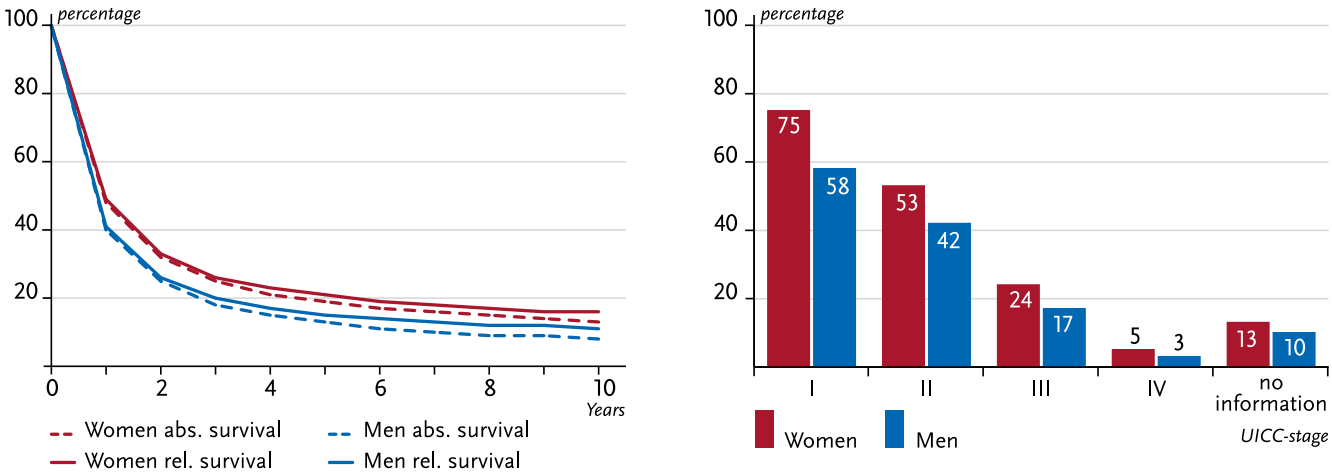

Figure 1.2: Left: Absolute and relative survival rates for lung cancer patients after first diagnosis in Germany 2015-2016. Relative survival rates were normalized by the survival of the entire population of the same age. Right: Survival by tumor stage. Figure from [1]. ©German Centre for Cancer Registry Data at the Robert Koch Institute.

1.2 Particle therapy for moving tumors

This work deals with particle therapy. This special type of radiotherapy makes use of physical and radiobiological advantages of ion beams compared to photon fields that are used in conventional radiotherapy. The depth dose distribution of a penetrating ion beam, the so-called Bragg peak, enables efficient sparing of surrounding organs. In contrast to photons, an ion beam stops inside the tumor. Its penetration depth depends on the anatomy and can be adjusted by setting the initial beam energy. Most energy is deposited at the end of range. Thus, tissue behind and before the tumor can be spared.
Several static tumors, for example in head in neck, are today frequently treated with ion beams. The dosimetric advantage makes particle therapy the radiotherapy modality of choice especially for pediatric patients, for which the appearance of radiation induced secondary cancers has to be avoided. The superior dose shaping capabilities of particle therapy therefore make this therapy a prime candidate for the treatment of NSCLC. However, a recent clinical trial did not show any advantage of particle therapy with passively scattered protons over photons for lung cancer patients [5]. In this study, the lung volume receiving a low dose was reduced for protons compared to photons. However, intrinsic limitations in the beam shaping capabilities of the passive scattering technique for the protons, as well as safety margins increased the lung volume receiving a high dose. This underlines the need for more conformal particle therapy treatments. Heavier ions than protons, like carbon ions, can deliver more conformal doses to deep-seated tumors due to the lesser degree of lateral scattering and due to an increased radiobiological effectiveness. This was recently demonstrated by spectacular survival rates in carbon ion radiotherapy studies of pancreatic cancer [6].
The target dose distribution can be shaped more conformally to the target with an actively scanned ion beam instead of the passive scattering. However, those efforts are limited by the size of the target volume. This is the entire region for which a high dose is prescribed. In currently used treatments, this volume contains 'internal' margins that cover the anatomical motion of the tumor. It is therefore desirable to enable treatments, in which the irradiated volume tracks the moving tumor. In addition, the 'interplay' of the anatomical motion and the simultaneous scanning of the beam causes hot and cold spots in the tumor and therefore a loss of target coverage which has to mitigated for a successful therapy.

1.3 Scope of this work

The effects of periodic motion on particle therapy have been studied in detail in many publications. Several 4D-optimization techniques have been developed in order to reduce the internal margins, but their clinical use is very limited. A reason is that the ability to achieve conformal treatments with sufficient target coverage was not verified for realistic, irregular motion. A potential overfitting to the periodic motion in the planning 4DCT makes conformal strategies vulnerable to unexpected anatomical motion. Consequently, the more conservative approach of increased safety margins around the tumor was chosen.
A strategy to reduce margins is to adapt the dose delivery in real-time such that the treatment field follows the tumor motion. Even though technically challenging, such a tumor tracking technique was realized in photon radiotherapy by mechanical movement of collimators or of the entire radiation source.
Lateral beam adjustments are technically much simpler in particle radiotherapy. However, those efforts were limited by the range changes in particle therapy that are negligible for photons. Attempts to optimize treatments based on motion information from imaging data available before treatment lacked the ability to adapt in real-time to unexpected changes of the motion pattern.
In chapter 2, the physical and radiobiological fundamentals of particle therapy as well as the aspects related to the treatment of moving tumors are introduced. In the following chapters, the present limitations in the development of motion mitigation were tackled in three ways:

1. Tools were developed and validated that enable the evaluation of scanned ion therapy in the case of irregular motion.
2. A new motion mitigation technique was implemented, that synergizes the conformity of a 4D optimization strategy for periodic motion with real-time adaptivity to irregular motion.
3. The performance of several motion mitigation techniques including the new one was assessed experimentally for the case of irregular motion.

For each aspect a corresponding research hypothesis was formulated and is explained in the following.

1.3.1 RBE-weighted dose calculation for irregular motion

In the last years, several tools to compute irregular series of volumetric CT images from 2D cine MRI data have become available [7, 8]. In addition, computed virtual 4DCTs [9] can be used to create artificial 4D imaging data. This enables the evaluation of the robustness of motion mitigation techniques against irregular motion. Conventional 4D dose calculation algorithms were only designed and validated for the periodic imaging data set, that was available at the time of development. Especially the memory handling was designed to hold only a limited, small number of imaging data. Consequently an adaptation to irregular imaging data is necessary and the validity of the modified algorithms has to be verified. In chapter 3, an extension of an existing dose calculation algorithm for RBE weighted doses for irregular motion is presented and validated experimentally.

> **Hypothesis I:**
> 4D dose calculation for carbon ion therapy can be precisely performed for irregular motion.

1.3.2 Implementation of a new real-time adaptive motion mitigation strategy

The conformal irradiation of moving tumors requires an active adaptation of the delivery to the actual tumor motion. In beam gating, this is done by restricting beam-on time to a predefined window of the

respiratory motion. This increases delivery time and therefore reduces patient throughput, comfort, and setup precision. In multi-phase 4D dose delivery (MP4D) [10], the sequence of the delivered raster spots is adapted to the observed breathing cycle. The combination of this synchronization with a 4D optimized treatment planning strategy enables a highly conformal irradiation. But it does not adapt to unexpected motion. Beam tracking has the ability to adapt in real-time to irregular motion. However, this adaptation is intrinsically limited for non-translational motion components, for example range changes, anatomical deformations and rotations. Consequently, it is desired to consider those changes already during treatment planning. But this again requires a synchronization of the beam delivery sequence.
A recent simulation study showed that a combination of beam tracking and MP4D can restore planned 4D dose distributions for intrafractional changes of the tumor motion and can help reduce margins required for the compensation of interfraction motion variability [11]. Hence, a new delivery technique was implemented into a dose delivery system that combines both adaptabilities: the synchronization of the beam delivery sequence to the breathing cycle by MP4D with the online adaptation of lateral spot positions by beam tracking. The technical implementation and first tests verifying the functionality are described in chapter 4.

> **Hypothesis II:**
> The compensation of irregular motion is technically feasible by a combination of multi-phase 4D dose delivery with lateral beam tracking.

1.3.3 Comparison of motion mitigation techniques

The performance of the new motion mitigation technique, as well as other, more established strategies, has to be evaluated for different, also irregular motion scenarios in an anthropomorphic anatomy. The study has to include treatment planning and delivery. As the strategies were implemented in hardware, measurements including the real-time behavior of the system are more reliable than simulations alone. Log-file based dose reconstructions can be further verified by detector measurements. For clinical implementation, the requirements on a motion monitoring system have to be defined. Such a study is described in chapter 5.

> **Hypothesis III:**
> The motion mitigation strategy MP4DRT is able to deliver highly conformal and homogeneous dose distributions to irregularly moving tumors. It synergizes the strengths of beam tracking and MP4D and therefore outperforms more established strategies.

2 Scanned ion beam therapy of moving tumors

Scanned ion therapy is a promising and emerging radiotherapy modality for various kinds of cancers. While the application to many static tumors as for example in head, neck and spine is rapidly growing, the treatment of moving tumors like in the lung is still challenging. In this chapter, first the physical and biological fundamentals of particle therapy with scanned ion beams are described. In section 2.2, a short introduction into treatment planning is given. Afterwards, the challenge of motion to scanned ion beam therapy is described, followed by available techniques for motion monitoring and imaging in radiotherapy. In section 2.5 the currently available motion mitigation techniques are summarized.

2.1 Particle therapy

External beam radiotherapy is a local therapy that aims to kill tumor cells while sparing the healthy tissue around them as much as possible. The tumor cells are killed or sterilized by ionizing radiation such that they cannot proliferate anymore. Most patients are treated with photons. This thesis, however, focuses on the therapy with charged particles. This form of radiotherapy requires a more complicated infrastructure, including particle accelerators, but offers the potential to constrain the dose better to the target than photon therapy. In this section, the fundamentals of particle therapy are introduced.

2.1.1 Ionizing radiation

Ionizing radiation are charged particles like ions or electrons, but also neutrons and photons. When penetrating into a material, they can transmit enough energy to break chemical bonds and ionize atoms and molecules in their surroundings. The energy transfer $\mathrm{d}E$ per mass unit $\mathrm{d}m$ is called the absorbed dose D and measured in the SI-unit Gray [Gy]

$$D = \frac{\mathrm{d}E}{\mathrm{d}m} \quad [1\,\mathrm{Gy} = 1\,\mathrm{J/kg}]. \tag{2.1}$$

The interactions between radiation and surrounding material are explained for photons and ions in the following.

Photons

Photons transfer their energy to the material mainly via three interactions: Photo electric absorption, Compton scattering and pair production. In all cases, the photons transfer their energy to charged particles that ionize the surrounding material via electromagnetic interaction. The intensity I of a photon field penetrating matter decays exponentially with depth x. This is called the Lambert-Beer law:

$$I(x) = I_0 \cdot \exp(-\mu x). \tag{2.2}$$

Here, μ is a material specific attenuation coefficient, and is the inverse of the mean free path until a photon interacts and is destroyed. The dose deposition along the beam direction shows a short build-up

until the maximum number of secondary charged particles is reached and then follows the exponential decay of the primary photons. Photon fields for radiotherapy are produced by linear accelerators that shoot electrons on a target and produce photons with an energy of a few MeV via bremsstrahlung. The dominating interaction for this energy is Compton scattering. As the energy deposition is concentrated to the isolated locations, where the photons interact, they are denoted as sparsely ionizing radiation. The fluence needed for clinically relevant doses causes many close-by interaction vertices from different photons and therefore a homogeneous 'dose bath' on the microscopic scale [12].

Ions

Charged particles ionize the surrounding material along their entire track by electromagnetical interaction with the atoms. In this process, secondary electrons are emitted that loose their kinetic energy by scattering within the material. The average energy transfer from the ions to the material $-\mathrm{d}E/\mathrm{d}x$, also called linear energy transfer (LET), depends on the projectile's velocity v and charge Z_p and is given by the Bethe equation:

$$-\frac{\mathrm{d}E}{\mathrm{d}x} = 4\pi\frac{e^4 Z_p^2}{m_e v^2}\cdot\frac{N_A Z_t \rho_t}{A_t}\left[\ln\frac{2m_e v^2}{\langle I\rangle} - \ln(1-v^2/c^2) - v^2/c^2\right]. \tag{2.3}$$

Here, Z_t, A_t, ρ_t, and $\langle I\rangle$ denote the charge, atomic mass, density, and mean ionization potential of the target material. The constants m_e, e, and c are the electron mass and charge, and the speed of light. When the ions penetrate the material, they are continuously slowed down and deposit most of their kinetic energy at the end of their range. The corresponding depth-dose profile is called Bragg peak (see figure 2.2). The penetration depth increases with the initial beam energy.
In clinically relevant settings, the LET for fast protons is similar to the one of photons, but increases with Z_p^2 for heavier ions. The particle fluence F an be converted to dose as

$$D[\mathrm{Gy}] = 1.6\times10^{-9}\cdot\mathrm{LET}\,[\mathrm{keV/\mu m}]\cdot\left(\rho\left[\mathrm{g/cm^3}\right]\right)^{-1}\cdot F[1/\mathrm{cm^2}]. \tag{2.4}$$

The ions might collide with the nuclei of the material, which causes fragmentation of both, projectile and target nuclei. Such peripheral collisions are described by the abrasion-ablation model illustrated in 2.1. The projectile velocity and therefore, the kinetic energy per projectile mass remains nearly unchanged. The reduction of Z_p^2 in equation (2.3) causes a lower relative loss of energy and therefore a longer range of fragments. While protons cannot fragment to lighter ions, they can still produce target fragments which affect the dose distribution. The fragmentation cross sections for heavier ions increases approximately with their geometrical cross section. The interactions of the ion beam with the material are statistical processes as they are ruled by the laws of quantum mechanics. This causes a spread of the particle range, which is denoted as range straggling. It is given by

$$\frac{\sigma_R}{R} = \frac{1}{\sqrt{M}}\cdot f\left(\frac{E}{Mc^2}\right), \tag{2.5}$$

where R and σ_R are the mean range and its standard deviation. M and E are the projectile mass and its kinetic energy. The function f is slowly varying and depends on the absorber [15].
As visible from equation (2.3), the energy loss and therefore the ion range is material dependent. For radiotherapy purposes, geometrical lengths in beam direction are converted to the range in water absorbing the same amount of beam energy, the so called water-equivalent path length (WEPL). The depth dose profiles of photons, protons and carbon ions in water are compared in figure 2.2. In lateral direction, the ion beam is broadened by elastic and inelastic scattering at the target nuclei. As illustrated in figure 2.3, light ions, like protons, are affected stronger by scattering. For this reason, the dose distribution can be

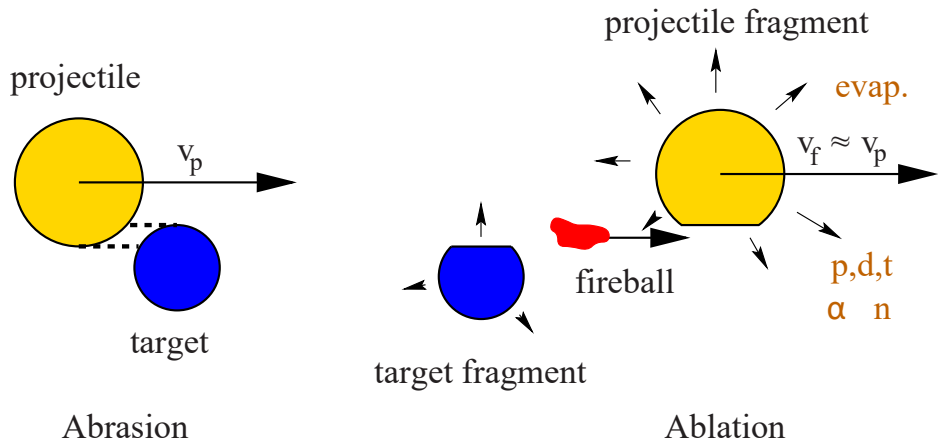

Figure 2.1: Fragmentation of target (blue) and projectile (yellow) nuclei as described by the abrasion-ablation model according to Serber [13]. Figure reprinted from [14] with permission from the American Physical Society.

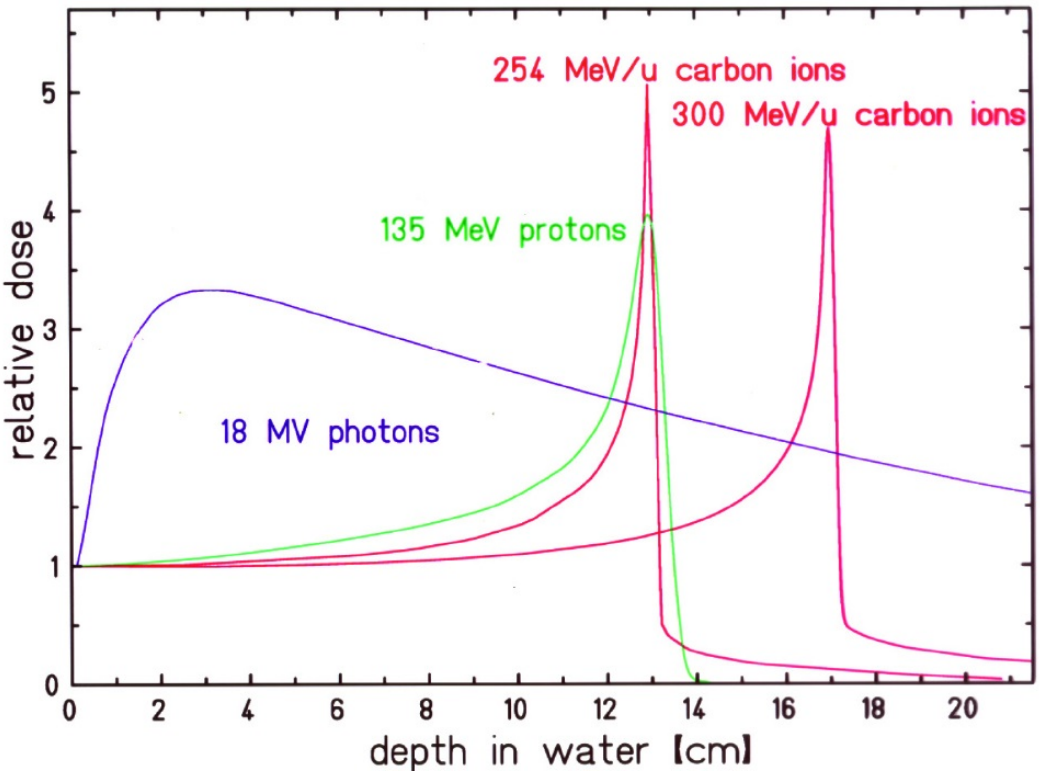

Figure 2.2: Depth dose profiles for photons from an 18 MV accelerator, protons and carbon ions. The dose was normalized to the entrance channel. Proton and carbon beam energies were selected to correspond to the same range. Figure from [16].

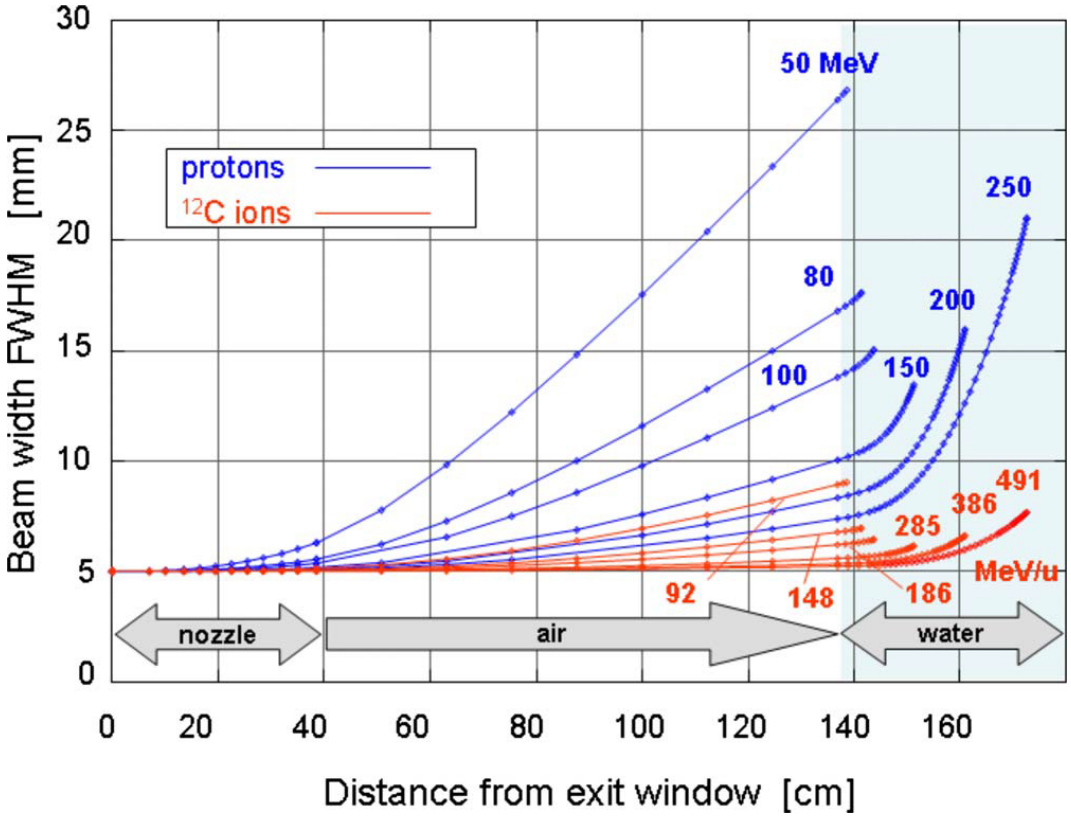

Figure 2.3: Lateral size of carbon and proton beams. For both cases, an initial beam width of 5 mm provided by the accelerator is assumed. Figure reprinted from [14] with permission from the American Physical Society.

shaped more closely to the tumor contour with carbon ion beams than with protons. The track structure represents the energy transfer to the material on a microscopic level by the motion trace of the secondary electrons. It is illustrated for proton and carbon ions of different energy and therefore LET in figure 2.4.

Radiobiology

The aim of radiotherapy is to kill or sterilize tumor cells by the mean of ionizing radiation. This is achieved by damaging the deoxyribonucleic acid (DNA) in the cell nucleus. If the cell is not able to repair the damage, it will either die in a controlled process called apoptosis or be unable to divide further. The cells are often able to repair single, isolated breaks of the DNA strands, as the complementary information is still available on the other strand. Close breaks of both strands, so-called double-strand breaks (DSB) and even more complex damages of the DNA are more difficult to repair. The DNA damage mechanisms are illustrated in figure 2.5. As direct action, the secondary electrons in the ion track break molecular bonds in the DNA. An indirect action is the formation of reactive oxygen species (ROS), typically free radicals that react with the DNA [17]. In photon radiotherapy, about 70 % of the DNA damage is caused by the indirect effect [14]. In tumors, there are often regions that are poorly supplied with oxygen, which makes them therefore more resistant to radiation. The average number of interaction vertices of the irradiation field with defined LET in proximity to the DNA increases linear with the fluence and therefore with dose (see equation (2.4)). On the local level of single cells, the number is given by a Poisson distribution. Consequently, the probability to have no lethal vertex in proximity to the DNA decreases exponentially

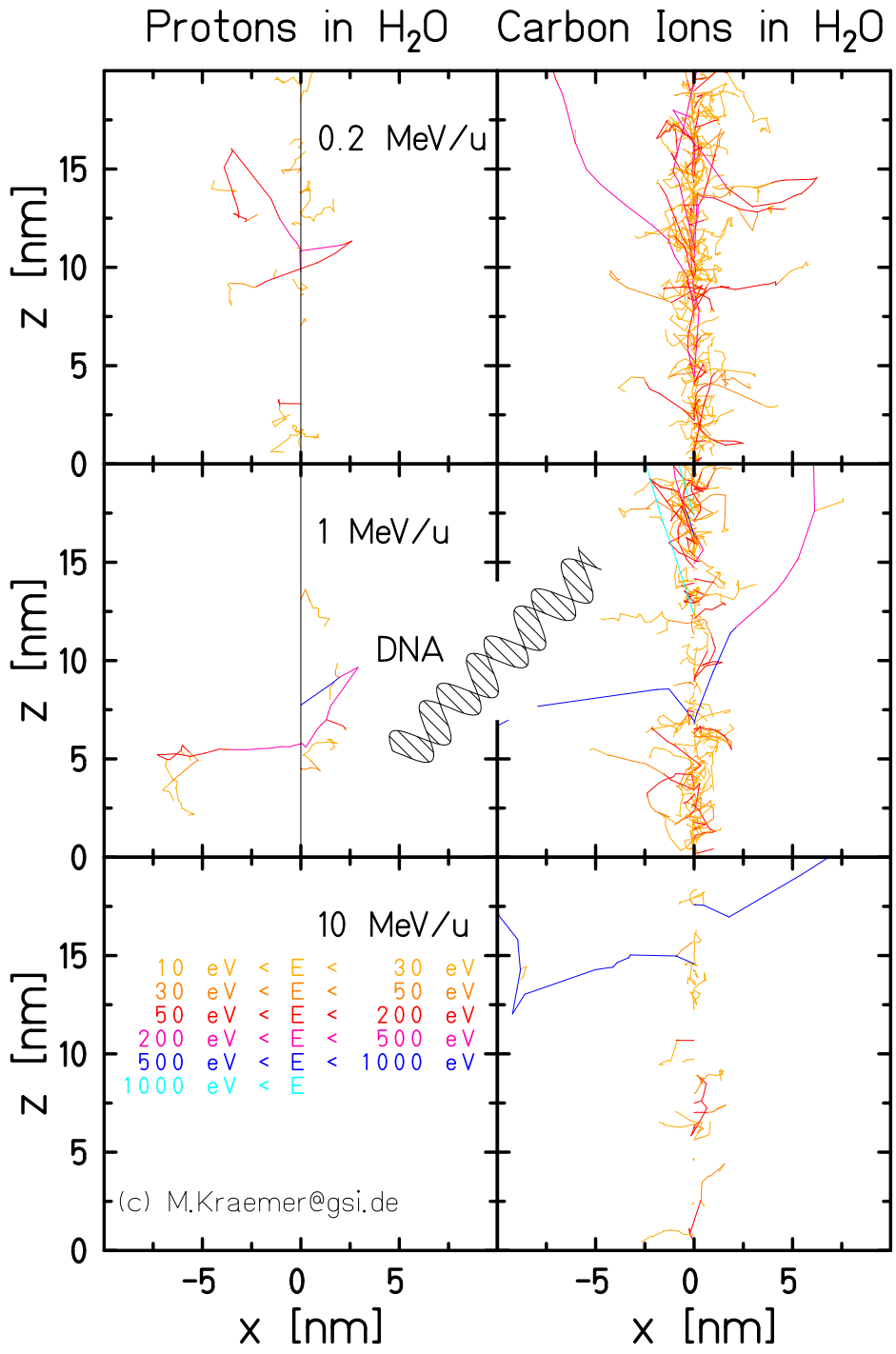

Figure 2.4: Monte Carlo Simulation of the track structure for proton and carbon ion beams. Figure reprinted from [12] with permission from Springer.

with the dose. As complex DNA lesions can be caused by contribution from several tracks, the probability for cell survival S can be approximated with a linear-quadratic model [19, 20].

$$S(D) = \exp(-\alpha \cdot D - \beta \cdot D^2). \tag{2.6}$$

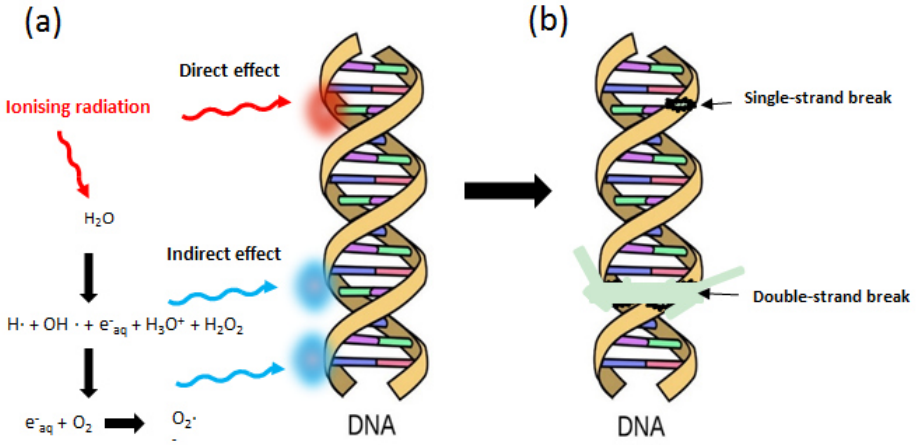

Figure 2.5: (a) Interaction of ionizing radiation with DNA. (b) Illustration of single and double strand breaks. Figure reproduced from [18].

The coefficients α and β depend on properties of the tissue as well as on the LET of the irradiation. Thanks to their dense track structure, single high-LET ions can cause complex DNA lesions by direct interaction. This makes them more efficient in killing cells with the same absorbed dose as photons, especially for hypoxic tumors [21]. Various models for computing the biological effect (i.e., the cell killing) for a given dose in particle fields have been proposed, of which the local effect model (LEM) [22, 23, 24] has been used widely in the context of carbon ion therapy. The ratio of absorbed ion dose to the photon dose yielding the same biological effect is denoted as relative biological effectiveness (RBE):

$$\mathrm{RBE} = \left.\frac{D_\gamma^{ref}}{D_{ion}}\right|_{iso-effect}. \tag{2.7}$$

The concept of RBE is illustrated with typical survival curves for photons and heavy ions in figure 2.6. For protons, a constant RBE of 1.1 is often assumed for treatment planning, even though there this is known to be a simplification [25, 26].

2.1.2 Treatment schemes

In most cases radiotherapy treatments are applied in fractions. There are biological and technical rationals:

- In cancer cells, DNA repair mechanisms are less efficient. This is the reason for their ability to mutate, but makes cancer cells more vulnerable to radiation damage. After a treatment fraction, more healthy cells in the surrounding tissue recover from the damage than tumor cells. Thus, side effects are reduced.
- Often, tumors contain hypoxic regions in their center that are far from blood vessels. The lack of oxygen prevents the formation of ROS and therefore indirect DNA damage. In a fractionated treatment, outer tumor layers are ablated and formerly hypoxic regions become more radiosensitive. This effect is more important for low LET radiation like photons and protons than for ion beams [21].
- Technical difficulties in the treatment delivery cause dose degradations. By repeated treatments, they are reduced by statistical averages.

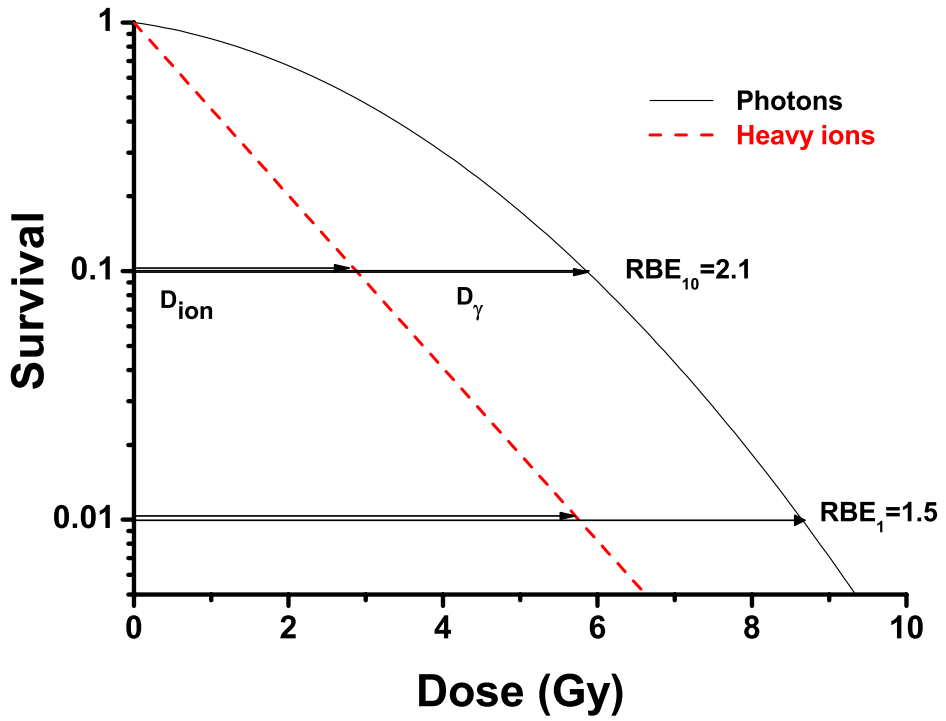

Figure 2.6: Sketch of a typical survival dose for photons and ions. The horizontal lines illustrate the definition of RBE for survival rates of 1 % and 10 %. The shoulder in the photon curve is less pronounced for heavy ions. Figure reprinted from [14] with permission from the American Physical Society.

Most patients are treated with 2 Gy to 3 Gy per fraction. Nevertheless, there is a trend towards hypofractionated treatment treatment schemes. Recently fractionation schemes with 72 Gy(RBE) in 16 fractions have been established for carbon ion radiotherapy [27]. For some tumors, even treatments in a single fraction were performed [28]. The reasons are:

- Shorter average time between imaging for treatment planning and delivery, therefore less anatomical changes.
- Patient comfort by shorter therapy.
- Patient throughput for the clinic, increasing accessibility and reducing treatment cost.
- An increased precision of the delivery enables better sparing of healthy tissue reduces the necessity of fractionation.

As the surrounding tissue is not protected by fractionation anymore, highly conformal treatments are required, in which organs at risk are spared. The lack of statistical averaging in hypofractionated treatments makes it necessary that a sufficiently high target coverage of the tumor is achieved in a single delivery.

2.1.3 Beam delivery

Photon fields are produced by small linear accelerators. The field is shaped to the tumor by collimators. Because of the relatively small size and cost, photon irradiation systems can easily be integrated into

hospitals and are the standard for radiotherapy of most cancers. However, the focus of this work lies on scanned ion beam therapy, for which larger particle accelerators are required.
Tumors are found in a water-equivalent depth from a few centimeters to more than 25 cm. The required kinetic beam energies therefore range from 60 MeV to 250 MeV for protons and 120 MeV/u to 430 MeV/u for carbon ions. For protons, these energies can be reached with cyclotrons that can produce a constant particle current of constant energy. The beam range is modified by inserting material into the beam after acceleration. For carbon beams, the use of bigger and more expensive synchrotrons is necessary. The ions are accelerated in packages up to the target energy and then slowly extracted from the synchrotron ring. The total time of extraction is called spill. It is interrupted by the times needed for acceleration and preparation of the accelerator system for the next package. Those interruptions are denoted in this work as spill pauses.
For both cyclotron and synchrotron accelerators, the beam is initially a thin pencil beam. Historically, the beam was passively broadened and shaped to the target volume by a series of scatterers, range modulators and collimators added into the beam line. Due to the limited dose conformity achievable with such a setup, passive beam shaping is widely abandoned and replaced by active beam scanning as illustrated in figure 2.7.

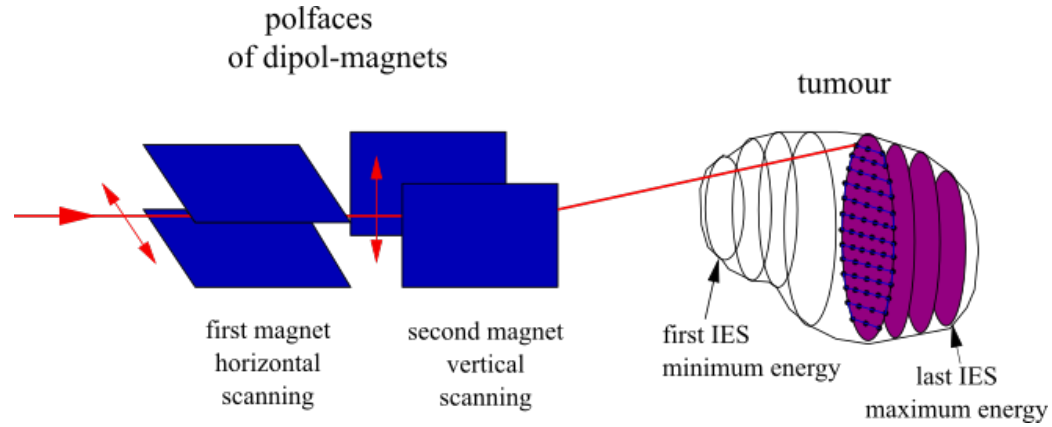

(a) Scanning system

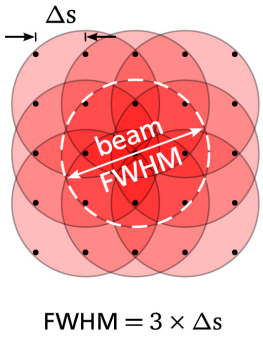

FWHM = 3 × Δs

(b) Lateral raster design

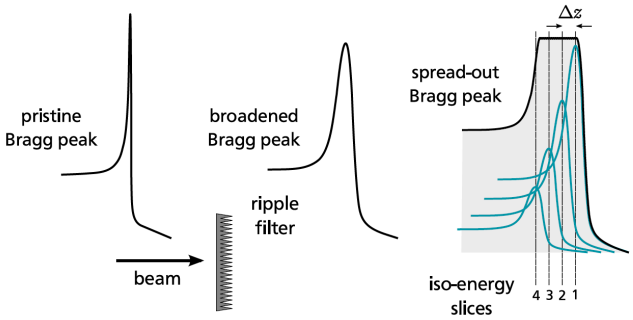

(c) Construction of SOBP

Figure 2.7: Delivery of a 3D dose distribution in scanned ion therapy. (a) Pencil beams are deflected using scanning magnets. The volume is divided into iso-energy slices (IESs) that correspond to initial beam energies. A homogeneous dose distribution is achieved by sufficient overlap of single pencil beams (b) in lateral and (c) longitudinal direction. The beam weights are optimized to achieve the desired homogeneous spread-out Bragg peak (SOBP) as the sum of the single pencil beams. Figure (a) adapted from [12] with permission from Springer and figures (b) and (c) from [29].

In order to deliver dose to a volume, the pristine Bragg peak of a single energy is unsuitable. Instead, beams of different energies are superimposed such that they add up to a flat 3D dose distribution, a so-called spread-out Bragg peak (SOBP). To increase the overlap of single energies, the Bragg peak is widened by the use of ripple filters [30]. During treatment planning, the target volume is partitioned into slices of equal water-equivalent depth in the body, so called IESs. In each slice, a lateral grid of beam spots is defined. The ion beam is scanned from spot to spot by horizontal and vertical dipole magnets. The energy slice is either changed by a range shifter that inserts different amounts of material into the beam, or by active energy variation between extractions. The number of particles assigned to each raster spot is defined in a treatment plan. The delivery of the treatment plan is controlled by a dose delivery system (DDS). It steers the beam by controlling the currents in the scanning magnets. The beam properties are measured by detectors in the nozzle, like strip and pixel detectors for beam position and ionization chamber detectors for the particle rate. More details about the DDS used in this work can be found in section 4.3.

2.2 Treatment planning

Treatment planning is the process of therapy design. It incorporates diagnostic imaging, the delineation of target volumes, the assignment of dose constraints for different organs and the computational optimization of the spot weights and beam path for the raster scanning. In clinical practice, all those steps require careful quality assurance (QA).

2.2.1 Target volumes

In accordance to the ICRU report 93 by the International Commission on Radiation Units and Measurements [31], different target volumes are defined:

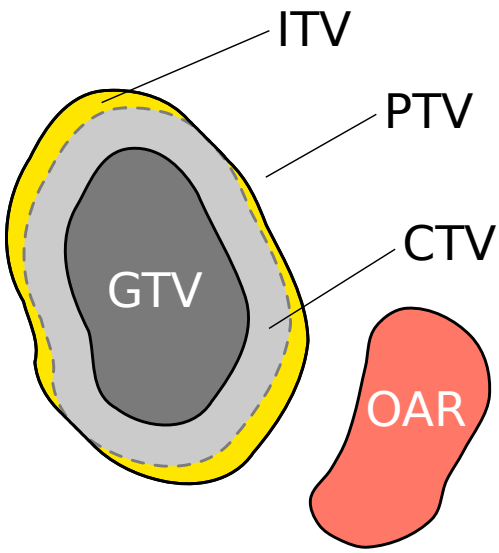

Figure 2.8: Definition of target volumes. Figure from [29].

Gross tumor volume (GTV): The GTV is the gross palpable volume of malignant growth that can be identified on diagnostic images.

Clinical target volume (CTV): The CTV is the volume where malignant cells are expected to be found. It contains the GTV and subclinical expansions, were tumor cells are too rare to be visible in the images.

The entire CTV has to be treated to avoid tumor recurrence.

Internal target volume (ITV): The ITV is the extension of the CTV by *internal margins*. The margins are used to account for possible organ motion. An ITV can be constructed by taking the union of the CTVs in different phases of a respiratory cycle either in real geometric space (gITV) or in a field specific water equivalent space (WEPL-ITV or range-ITV).

Planning tumor volume (PTV): The PTV is the entire volume, to which a dose is assigned. It is the extension of the CTV by setup margins and internal margins.

Organs at risk (OARs): OARs are healthy organs that are expected to be affected by the irradiation.

While GTV, CTV, and OAR are clinically defined volumes, the definition of ITV and PTV depends on the treatment modality, field directions, patient posture and available image guidance options. The explicit definition of a target volume is restricted to a static anatomy. For a moving anatomy, however, the same organ can occupy a different volume at different points in time. In 4D-optimization (see 2.5.5), patient anatomy and target volume in different motion states are included into the dose optimization algorithm. This is an implicit definition of the ITV [32]. Similarly, the potential setup errors that were the reasoning for the margins used to construct the PTV can be directly included into the optimization of the dose in the CTV. This is denoted as robust optimization [33].

2.2.2 Dose optimization

The treatment plans are created using dedicated software. For this work, the research software TRiP98 [23, 33, 34] was used. Treatment plans are optimized using an 'inverse' optimization technique. First desired properties of the dose distributions are defined by setting a prescribed dose to the target volume and dose constraints on OAR volumes. A cost function is defined that contains a penalty for underdosage in the target and overdose in the OARs. A raster grid of Bragg peaks is created that covers the target volume. Then an algorithm is used to minimize the cost function by optimizing the number of particles assigned to the raster spots. Different weights can be assigned to target and OAR in order to find a good compromise between tumor control and normal tissue complication probability (NTCP). As the optimization process starts with the desired dose distributions and then tries to find the corresponding, underlying raster grid, it is termed 'inverse' optimization. In contrast, the expected dose distribution for an existing treatment plan is simulated by 'forward' dose calculation.
In clinical reality, most tumors are treated with several fields from different directions in order to spare tissue in the entrance channel of the beam. In the single field uniform dose (SFUD) approach, all fields are optimized separately for a homogeneous fraction of the target dose. In intensity modulated particle therapy (IMPT), all fields are optimized simultaneously. This enables a better sparing of OARs, but is more sensitive to misalignments or range uncertainties of the single treatments fields with respect to each other than the SFUD approach [35, 36]. The name IMPT is chosen to stress the analogy to the corresponding intensity modulated radiotherapy (IMRT) for photons. As scanned ion beams are intensity modulated independent of the multi-field optimization strategy, also the term multi field uniform dose (MFUD) is used [36].
In figure 2.9, planned dose distributions for two patients with multiple metastasis in the lung are shown. The dose distributions on the left is a plan optimized for carbon ion IMPT. On the right, the corresponding stereotactic body radiation therapy (SBRT) with photons is depicted. For photons, treatment fields from all directions are required to limit maximum doses to the healthy tissue.

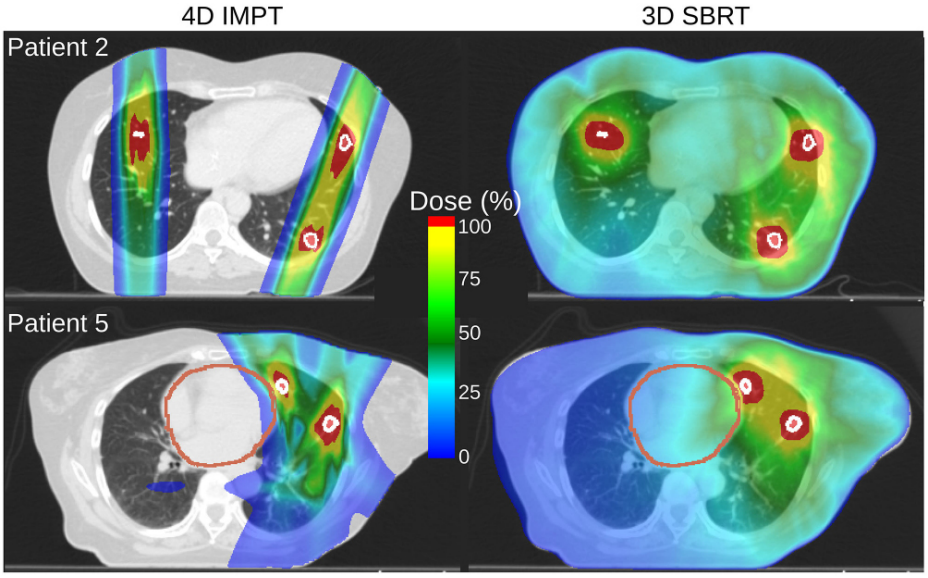

Figure 2.9: Planned dose distributions for photon SBRT and carbon ions for two patients with multiple lung tumors. Figure from [37].

2.3 Tumor motion

Organs are subject to anatomical motion. Typically, two timescales are considered:

Interfractional motion: The anatomy and breathing pattern changes in between fractions and between imaging for treatment planning and the actual delivery. The timescale is therefore days.

Intrafractional motion: Short term motion, mainly caused by respiration, heart beat and digestion. The timescale ranges from seconds to minutes.

Respiration is driven by an expansion of the rib cage and more strongly, by the diaphragm. The biggest anatomical motion is therefore observed in the lower lung and the abdomen. For lung tumors, motion amplitudes of more than 20 mm are observed. Respiratory motion contains a periodic component, but is also affected by systematic changes like organ drifts [38] and amplitude variations [39]. Because of the periodicity of breathing, respiratory induced motion is typically binned into several discrete motion phases that are assumed to repeat. In this work, the deviation of the real irregular motion from the assumed periodic, discretized motion is denoted as **residual motion**.
Organ motion challenges particle therapy in multiple ways:

1. As the tumor moves during delivery, the motion has to be considered already at the treatment planning stage. This includes the definition of target volumes.
2. The 'interplay' between anatomical motion and the scanning motion of the beam distorts delivered doses.
3. Changes of the amount of material in the entrance channel cause range changes of the ion beam.

The sharp dose gradients imposed by the Bragg peak, the primary advantage of particle therapy over conventional therapy, also pose a great challenge in the context of anatomical motion. To avoid underdosage of the target volume, or overdosage of healthy tissue and OARs, care needs to be taken when defining the ITV and PTV for particle therapy.

2.3.1 Irregular tumor motion

Respiratory motion in freely breathing patients is subject to strong inter- and intrafractional changes. Dhont et al. reported for a group of 19 lung cancer patients with average cranio-caudal (CC) motion amplitude of (16.4±7.6) mm and treated with photon stereotactic body radiotherapy radiotherapy that 16 % of all lesions had an average interfraction motion variability greater than 5 mm in cranio-caudal direction. For 42 % of all lesions, the maximum intrafraction variability was greater than this threshold. For 37 %, the difference between treatment and planning 4DCT was greater than 5 mm. Also for 37 % of those patients, an intrafraction baseline drift greater than 5 mm was observed [39]. The irregular, intrafraction motion in this study is illustrated in figure 2.10. Irregular motion also increases the PTV margins on top of the initial

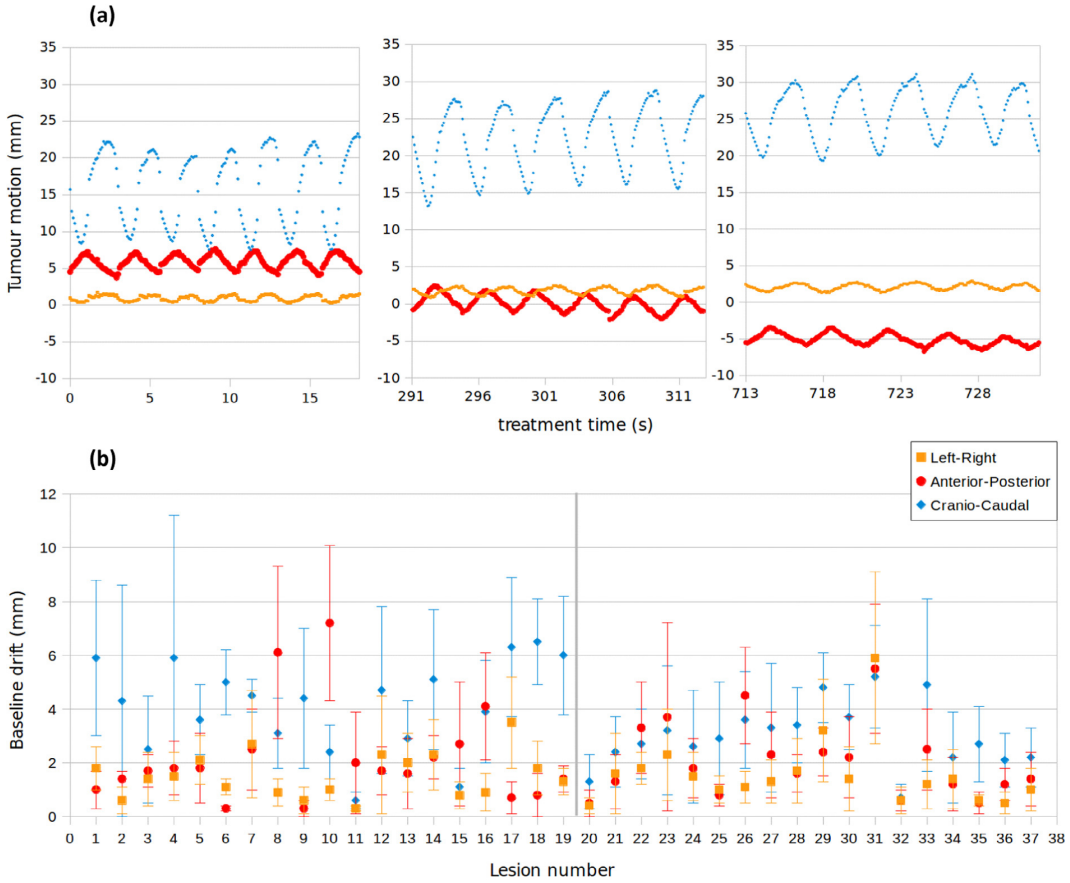

Figure 2.10: (a) Irregular tumor motion for non-small cell lung cancer patient treated with photon stereotactic body radiotherapy. (b) Baseline drifts for lung (lesion number 1-19) and liver lesions (20-37) averaged over several fractions. Reprinted from [39] with permission from Elsevier.

ITV necessary to guarantee the presence of the tumor inside the PTV over the course of treatment from 5 mm to 13.7 mm in CC direction.

2.3.2 Interplay

The interplay effect is the interference of the motion of the scanned ion beam and the irradiated tissue, which causes a distortion of the planned dose distribution. It is illustrated in figure 2.11. In an inhomogeneous geometry, the interplay is also created by range changes induced by material shifting into or

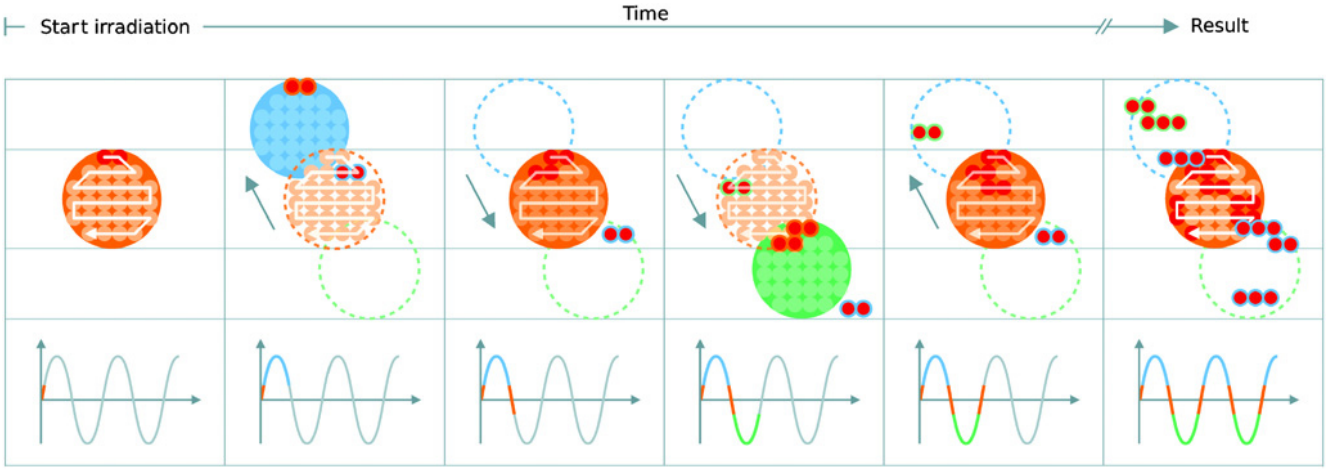

Figure 2.11: Schematic illustrating the interplay effect. The dose delivery system delivers spots on a predefined scan path in static room coordinates. In the coordinate system of the moving target, the spot positions depend on the motion phase (red, blue or green) they were delivered in. Figure used with permission of Institute of Physics and Engineering in Medicine, from [40]; permission conveyed through Copyright Clearance Center, Inc.

out of the beam path in the entrance channel. The effect of interplay strongly depends on the temporal correlation between tumor motion and delivery progress. Consequently, if no mechanisms are implemented to synchronize delivery with respiration, the exact dose distribution is unpredictable. The dependence of interplay patterns on the scan path is illustrated in figure 2.12.

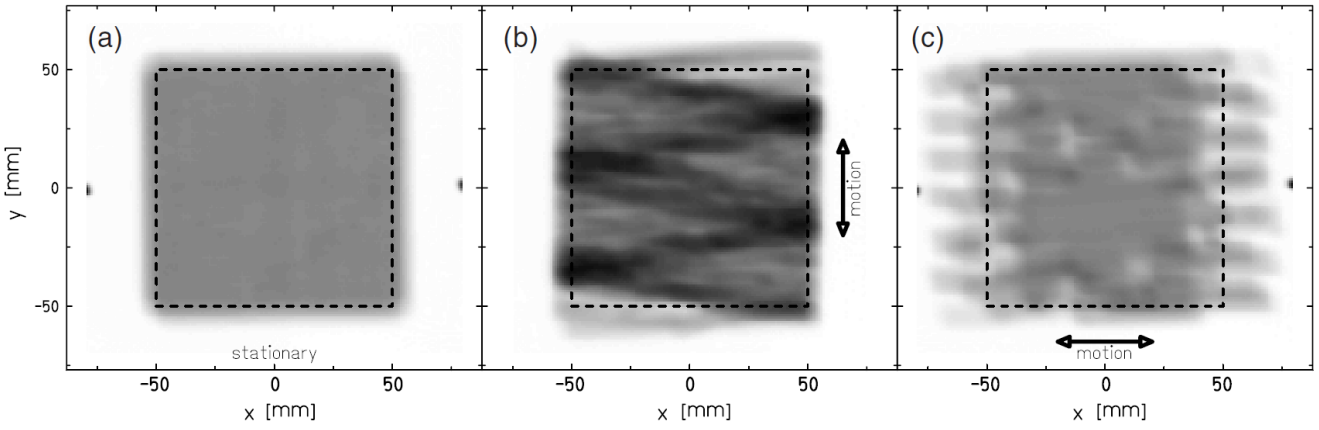

Figure 2.12: Interplay measured with a radiographic film. For the same plan, the film response for (a) static, (b) vertical, and (c) horizontal motion. The plan was scanned in horizontal lines. Figure used with permission of Institute of Physics and Engineering in Medicine, from [40]; permission conveyed through Copyright Clearance Center, Inc.

Typically, the possible range of dose distortion caused by interplay is estimated by simulating dose distributions with the start of the delivery in different motion phases [41, 42] and, less frequently, with different motion periods [41].

2.4 Image guidance

In radiotherapy, imaging is a necessary tool for diagnostics, treatment planning, patient positioning and motion monitoring, as well as outcome control and patient follow-up. The requirements placed on imaging depend on the purpose. **Diagnostic imaging** serves the purpose to identify and contour malignant tissue. Therefore often contrast agents or tracers are used that are enriched in the tumor.
Planning or **simulation imaging** is used to provide the anatomical and physical information required for treatment planning. This is of special importance for particle therapy to calculate the beam range within the patient to a high degree of accuracy [43]. Low time constraints enable volumetric and 4D imaging.
In-room imaging serves the purpose to verify that the current patient anatomy and position on the treatment couch are in sufficient agreement with the imaging data used for treatment planning. As patient alignment has to be done for each treatment fraction, dose constraints play an important role. In addition, time uptake for in-room imaging directly impacts patient throughput. Therefore, time constraints are more important compared to diagnostic or planning imaging.
Motion monitoring systems have the task to determine the tumor position in real-time. Therefore, imaging frequency and the latency caused by image reconstruction are critical parameters. In addition, as motion monitoring has to be continuously done for real-time adaptive delivery techniques during the entire delivery, dose constraints are highly relevant.
In the following, the most important imaging modalities for particle therapy are briefly presented.

2.4.1 Computed tomography

For treatment planning, high quality 3D computed tomography (CT) images are used. Those volumetric images are reconstructed from the absorption of x-rays in the tissue along different axis. Consequently, they reflect the interaction of photons with matter, which is strongly related to the electron density. The absorption coefficient μ is given in Hounsfield units (HU):$= 1000 \times (\mu_{material} - \mu_{H_2O})/(\mu_{H_2O} - \mu_{air})$. For calculating the Bragg peak position in the patient for a given beam energy, the tissue stopping power is estimated from a heuristic calibration curve, the so-called Hounsfield-Unit lookup table. Uncertainties in the conversion are typically accounted for by adding longitudinal safety margins to the target volume [43].
The CT images are taken slice by slice and then sampled to form a 3D image. For moving anatomies, the 2D projections can be sorted retrospectively into discrete motion phases. For each phase, a 3D image is reconstructed, such that all phases form a periodic 4DCT.
Before treatment, CT images of lower quality, so called cone beam computed tomography (CBCT) can be taken. The advantage of a CBCT is the reduced radiation dose to the patient compared to a normal CT, while still giving volumetric information on soft tissue, which is not available in X-ray projections. Those images are used to check sufficient agreement between the planning CT and the current anatomy during treatment.

2.4.2 Magnetic resonance imaging

Magnetic resonance imaging (MRI) offers high soft tissue contrast and the possibility for volumetric imaging without additional dose to the patient. However, several restrictions limit the application in particle therapy. No direct information about the particle range in the material can be obtained from MRI as the imaging principle is agnostic to electron density. MRI-to-CT conversion techniques require further validation for treatment sites undergoing breathing motion [44].
In-room imaging using MRI for particle therapy is under investigation [44], but so far prevented by its interaction with the treatment system. MRI suffers from minor geometrical distortion due to inherent

disturbances in the magnetic field [44]. The deflection of the ion beam due the magnetic field of the MRI has to be considered during treatment planning [44, 45]. In addition, the presence of an MRI imaging device in the treatment room is hindered by space constraints. Therefore, the most frequent role of MRI in radiotherapy is diagnosis and contouring.
Similar to a 4DCT, also 4DMRI images can be created by sorting images into motion phases. Series of single slices, so-called cine-MRI can be recorded with frequencies of typically 4 Hz to 10 Hz. This enables online tumor tracking of lung cancer tumors during treatment [46]. Anatomical motion deduced from those images can be used to compute deformed 4DCT images from a static CT [8, 47].

2.4.3 Positron emission tomography

Radioactive nuclei undergoing β^+-decay emit positrons, which annihilate together with electrons to two 511 keV photons leaving the vertex back to back. In positron emission tomography (PET), the photons are detected and the common origin is located. For diagnostics, radioactive tracers, mainly ^{18}F bound to a sugar molecule, are injected and enriched in tumors thanks to their increased glucose uptake rate [48]. As β^+-emitters are also produced by target and projectile fragmentation, PET can also be used for range verification in ion beam therapy [49]. Recent proof-of-principle experiments also investigated the use of radioactive ^{10,11}C and ^{15}O beams that would increase count rate and give a more direct access to the Bragg-peak position [50, 51, 52].

2.4.4 X-ray radiography

Online imaging of the tumor motion can be achieved by 2D X-ray radiography. Two orthogonal projection planes are interleaved to obtain the tumor motion in 3D. X-ray systems are often present in treatment rooms as they are used for patient alignment. X-ray radiography offers sub-mm resolution [53]. In order to have high contrast landmarks, it is often used in conjunction with marker implants. X-ray radiography was already investigated for online-tumor tracking in particle therapy [54]. A problem is the additional dose applied to the entire imaged volume.

2.4.5 Ultra-sound

Ultrasound (US) detects interfaces, on which sound waves are reflected. Images of single planes can be taken at a rates higher than 25 Hz [55]. US offers high contrast and resolution at interfaces between materials of different density, for example the diaphragm. This makes it suitable for liver patients [56, 57]. However, structures inside the lung cannot be imaged as the sound waves are reflected by the high density gradient at its interfaces. Another challenge is the reproducibility of images, as the quality strongly depends on the positioning and contact pressure of the ultra-sound probe [58].

2.4.6 Motion surrogates

For motion monitoring, instead of imaging the internal anatomical motion directly, it is possible to use more easily accessible data of external and internal surrogates. Possible candidates are for example optical markers on the patient surface observed with a system of optical cameras, the expansion of a compression belt, air flow through a spirometer, or the position of internal structures as the diaphragm imaged by US. The same surrogate is observed during diagnostic imaging and treatment. During diagnostic images, it is used to sort images into motion phases to create 4DCT or 4DMRI images. During treatment, it can be used to determine the current respiratory motion phase or as gating signal.

2.4.7 Hybrid systems

As direct imaging of the tumor is often not possible with the required frequency or would lead to unacceptable additional dose to the patient, hybrid systems are used that link easily accessible surrogates to internal tumor motion. A set of images of the internal motion is taken in-room before the treatment and combined with simultaneously recorded surrogate signal. A correlation model between internal motion and surrogate is created, for example by training an artificial neural network [59]. During treatment, the model is used to calculate the current tumor position based on the continuously measured surrogate signal. Sparse images of the internal motion are taken to verify if the model is still valid and for possible model adjustment. For photon therapy, such hybrid systems are in clinical use and reach a tumor tracking precision of about 1 mm [60, 61, 62].

2.5 Motion mitigation

Several approaches were developed to mitigate the adverse effects of motion on particle therapy quality. One strategy is to reduce anatomical motion by immobilization devices, breath hold and active breath control. Another strategy is to modify treatment plans and beam delivery such that they can deal with anatomical motion. So far, only gating, rescanning and breath-hold techniques are in clinical use.

2.5.1 Patient immobilization

The anatomical motion can be restricted by the use of immobilization devices, such as compression belts. Most often abdominal compression is used to limit the possible range of respiratory motion. This technique leads to patient discomfort and hindered breathing. The reduction of the tumor motion amplitude is strongly patient and tumor site specific. For some cases, even an increase in tumor motion has been observed with immobilization devices [63].

2.5.2 Gating

In gated deliveries, either directly the tumor or a correlated surrogate are observed. The beam-on time of the delivery is restricted to a window, in which the deviation of the target position compared to the planning stage, as well as its residual motion are assumed to be acceptable. The size of gating windows is facility dependent, but is usually defined, such that the expected range of residual target motion during the gating window is between 3 mm and 5 mm. Depending on the motion amplitude of the tumor, this can lead to a substantial prolongation of the treatment time. Gating can be done based on the motion phase, as well as the motion amplitude. Amplitude based gating requires to observe the tumor position during treatment. Especially in the presence of baseline drifts, the duty cycle can decrease strongly over the course of treatment [64]. Often, only the motion phase provided by a surrogate is used to define the gating window and therefore lacks information of systematic baseline drifts. To avoid dose inhomogeneity caused by the residual tumor motion within the gating window, gating is often combined with rescanning.

2.5.3 Breath-hold and breath control

It is possible to reduce anatomical motion by gating the beam on a breath-hold of the patient. This can be either voluntary or enforced by actively controlling the air flow [65]. Breath-hold times can be significantly prolonged by training and ventilation with oxygen [66]. However, this is only possible if the patient can tolerate the discomfort related to ventilation.

2.5.4 Rescanning

Interplay is the result of the temporal correlation between target motion and the scanning of the beam which was unknown at the stage of treatment planning. The idea of rescanning, also called repainting, is a statistical averaging of the random motion induced artifacts by repeated irradiation of the target volume. An ITV is used for treatment planning. If the temporal correlation between delivery of single scans and

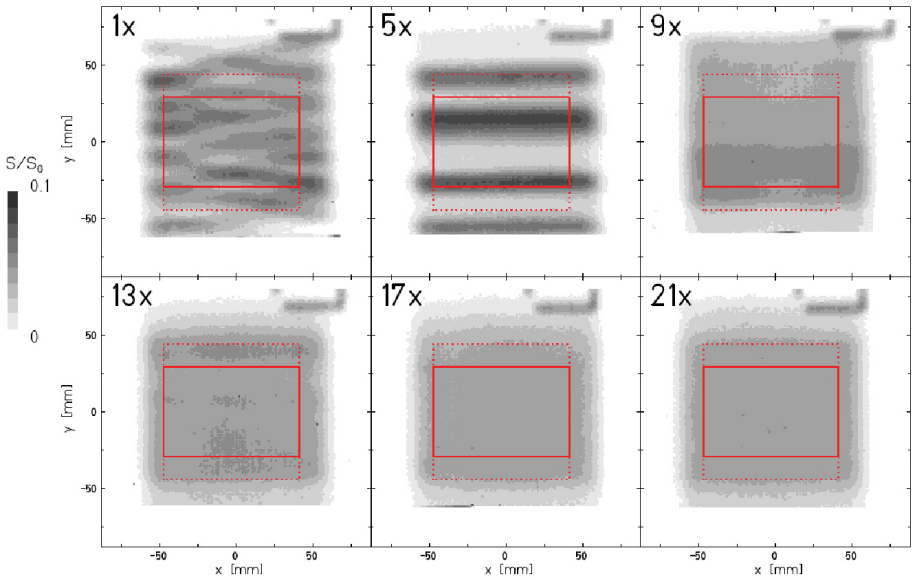

Figure 2.13: Film measurements for a vertically moving target. The dotted rectangle mark the ITV. In the CTV (solid rectangle), a homogeneous dose is achieved though statistical averaging for a sufficient number of rescans. Figure from [67].

motion is random, statistical averaging yields the convergence of the dose distribution towards the average of static dose distributions calculated in all phases. To ensure convergence, strategies were developed to distribute the rescans evenly over the expected breathing cycle. In phase controlled [64, 68], and breath-sampled rescanning [41, 42, 69] the beam intensity is adapted such that the delivery of each IES takes about an integer multiple of a breathing cycle or the expected time in a gating window. In layered or slice-by-slice rescanning, all repaints for one IES are repeated before proceeding to the next slice. In volumetric rescanning, the irradiation is repeated after scans over all slices [70]. This increases the time span between rescans and therefore avoids a fast delivery of all repaints of IES with small integral particle number in few subsequent motion phases.
Also the fractionation of treatments leads to the averaging of interplay patterns as the temporal correlation between anatomical motion and delivery progress is not fixed. It therefore can also be considered as a rescanning strategy [71]. In addition to the interplay, it also mitigates effects that are systematic for single days, like patient setup errors or anatomical changes.

2.5.5 4D-optimization

The anatomical motion observed in the 4DCT used for treatment planning can be taken into account in the treatment planning. This is achieved by defining the cost function of the optimization as the sum of the cost functions in all motion phases. Thus, no ITV has to be defined explicitly [32, 37, 72]. Instead, a static PTV, as well as static OAR volumes are delineated in each motion phase. In this strategy, the optimizer

adds dose to volumes outside of the static PTV in a single phase to achieve target coverage in the other motion phases. This can be considered as implicit construction of the internal margins of an ITV. The 4D optimization is usually combined with rescanning.

2.5.6 Beam tracking

Beam tracking is an real-time adaptive strategy. The tumor position is determined by a motion monitoring system and the beam position is adjusted to follow the tumor motion [73]. Thus, safety margins can be significantly reduced compared to an ITV. For scanned ion beam therapy, the beam can easily by adjusted in lateral direction by adaption of the magnet currents. For a fast adjustment of the beam range, a system composed of fast moving wedges at the nozzle was tested at GSI Helmholtzzentrum for Heavy Ion Research, Darmstadt, Germany (GSI) [74, 75].
A challenge in beam tracking is the question which point of the tumor to track. The position that is most simple to measure is the tumor center-of-mass (COM). However, inhomogeneous tissue in the entrance channel causes different range changes for different parts of the tumor and in rotating and deforming tumors, different parts of the tumor move differently. To deal with this problem, 3D deformable motion information has to be extracted from the motion signal. In an approach at GSI, the expected motion was determined before treatment for each motion phase based on the planning 4DCT [75]. At Paul Scherrer Institute, Villigen, Switzerland (PSI), methods to extract 3D deformation maps from 2D online imaging data were developed, which allows to the adaption to unexpected, irregular motion [54, 56, 57]. In both approaches, only the position of the Bragg peak within the target is used to compute the required adjustments to the pencil beam lateral position and range. This neglects the dose contributions of the entrance channel and the lateral penumbra of the beam. For tissue rotations, this is illustrated in figure 2.14. Hence, dose differences in the tissue leading up to the Bragg peak are not explicitly mitigated, and may even be induced. Since the healthy tissue leading up to the target moves differently than the target itself, beam tracking can cause an 'inverse' interplay effect, where instead of in the target, dose inhomogeneity patterns are present in the healthy tissue. The combination of beam tracking with rescanning is denoted as retracking. In simulations, no clear advantage of 3D deformable tracking over 2D retracking of the tumor COM was shown [54].

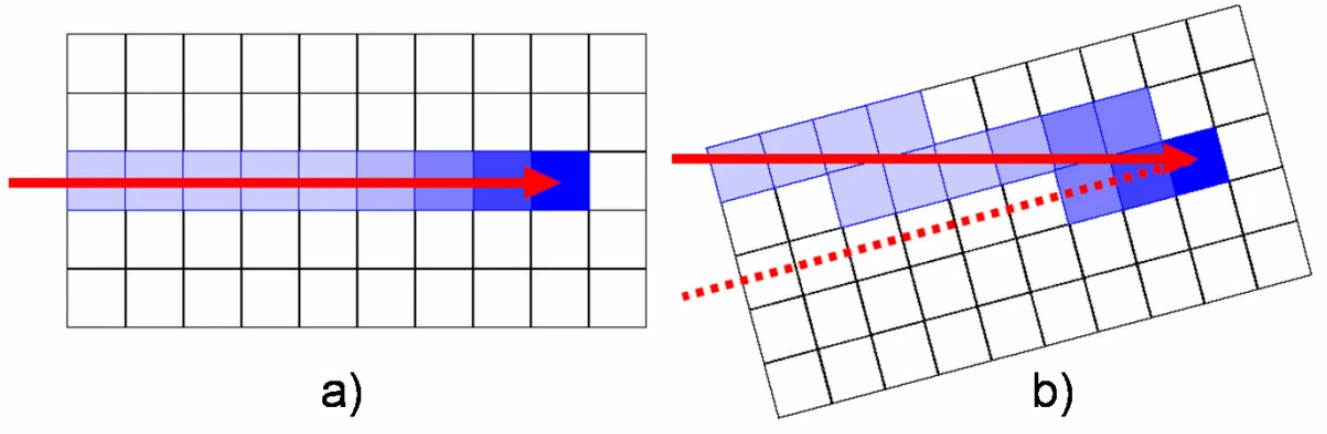

Figure 2.14: Effect of tissue rotation in beam tracking. In (a), the planned dose of a single pencil beam is shown. In (b), the tissue rotated. Beam tracking was applied, such that the Bragg peak is still in the same voxel, but the dose in the entrance channel is now deposited differently compared to the planning. Figure from [76].

2.5.7 Multi-phase 4D delivery (MP4D)

Multi-phase 4D dose delivery (MP4D) is a beam delivery strategy that synchronizes the delivery progress with the observed anatomical motion. It therefore enables time-resolved 4D-optimized treatment planning. The concept of the beam delivery was first proposed in conjunction with the now abandoned 4D sectors treatment planning approach [77]. It is illustrated in figure 2.15. The more recently used strategy was first proposed as '4D rescanning' or 'single phase uniform dose (SPUD)' approach [78]. The treatment planning is based on a 4DCT, which is a series of CT images each representing a motion phase. For each phase, a quasi-static and therefore conformal treatment plan is optimized for a homogeneous fraction of the target dose. The fractions are selected such that the sum of all phase plans add up to the overall target dose of the treatment. The library of 3D treatment plans forms the 4D treatment plan.
The delivery proceeds energy by energy. The breathing motion of the patient is monitored using a surrogate

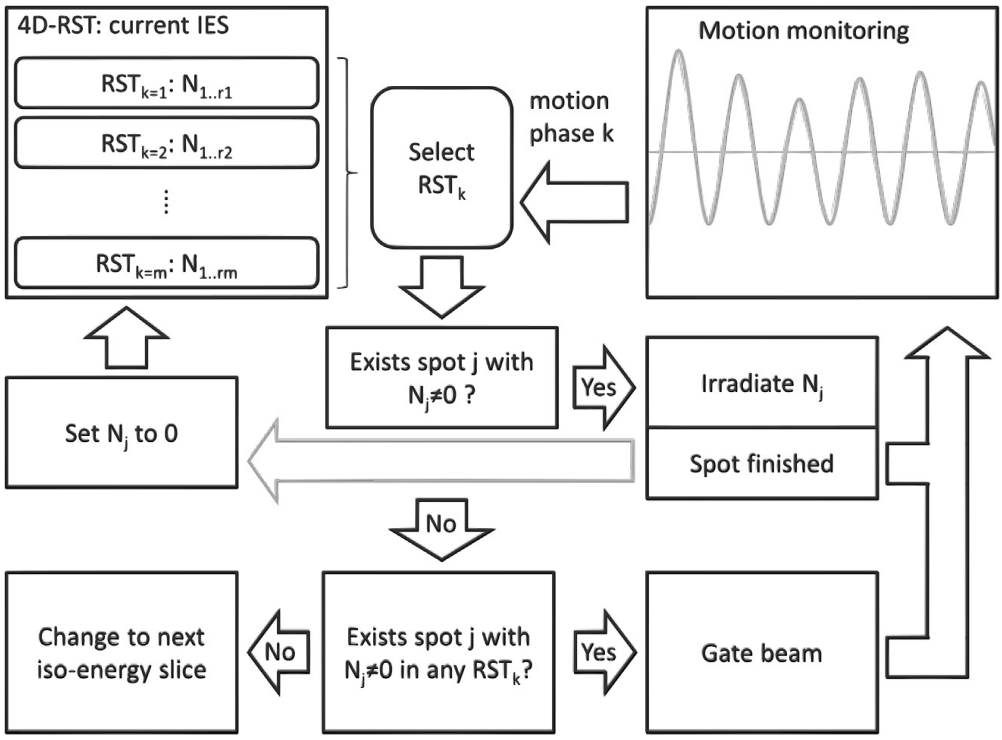

Figure 2.15: Flow chart describing the procedure of an MP4D delivery. Image taken from [77]. Here, treatment plans of single motion phases are denoted as RSTs.

and the motion phase is calculated online. The DDS switches without delay between treatment plans and ensures that always the plan optimized for the current motion phase is being irradiated. If all spots for this phase and energy were already delivered, the beam is interrupted with a gate. Only after all phase plans for the current energy were completed, the delivery proceeds with the next IES. MP4D was first implemented into a research version of the clinical dose delivery system of Centro Nazionale di Adroterapia Oncologica, Pavia, Italy (CNAO) [10]. It offers several advantages:

- For each phase plan, safety margins compensating the motion in other motion phases are not necessary.

- Range changes and tumor deformations are correctly compensated and the 3D raster forming the dose in each phase plan stays unaffected.
- The motion of OARs close to the tumor can be fully accounted for during the treatment planning. This enables efficient sparing.
- The separate irradiation of the multiple treatment plans in different motion phases provides an intrinsic breath-sampled rescanning. This leads to a compensation of residual intra-phase motion.
- Assuming a periodic breathing motion, a 4D QA procedure was demonstrated [79].

Treatment times in MP4D treatments strongly depend on accelerator characteristics. On the one hand, reduced target size compared to ITV rescanning decreases irradiation time. On the other hand, for each IES, the irradiation of each phase plan requires the beam-on time to last at least one motion period. If the spill length of a synchrotron is shorter than one motion period, at least two acceleration cycles per IES are necessary.
The treatment plans in MP4D can be tailored closely to the periodic motion in the planning 4DCT. This contains the risk of a potential overfitting. Robustness to irregular motion changes can be restored by increased target margins [80], spoiling the advantageous conformity of this technique.
In this thesis, an approach to extend MP4D to irregular motion is investigated by a combination with lateral beam tracking.

3 RBE-weighted 4D particle dose calculation for non-periodic motion

This chapter was published in 2021 in Physica Medica 91, Timo Steinsberger et al. ”Extension of RBE-weighted 4D particle dose calculation for non-periodic motion”, pp. 62-72 Copyright Elsevier (2021)[81].

3.1 Introduction

Scanned charged particle therapy has become an established therapy for static tumors, offering more conformal dose distributions than photon therapy [82, 83]. This high degree of conformity poses geometric and dosimetric uncertainties when accounting for inter- and intrafractional motion [73, 84, 85]. Tumors in the thorax and abdomen are strongly affected by respiratory motion and its variability [38, 39]. Therefore, treatment methods have been developed in attempt to handle tumor motion during radiotherapy including gating, ITVs, rescanning, tumor tracking [73, 86] and 4D optimization [87], as well as robust optimization [33, 72, 88].
Delivery quality assessment is an integral part of clinical radiotherapy. Typically, treatment planning, simulations and dose reconstructions are performed to simulate expected dose distributions and assess delivered dose distributions respectively [89]. However, only periodic repetition of the respiratory motion is currently assumed for treatment planning on a time-resolved computed tomography (4DCT) [90], which depicts an averaged tumor motion. 4D dose calculations take into account the inter- and intrafractional motion variability of recorded motion signals when assigning motion phases, but still assumes that one 4DCT would be representative for an entire treatment fraction [91]. This means that a variable breathing periods can be accounted for, but varying amplitudes or baseline drifts cannot. Dhont et al. [39] reported interfractional variations in the motion amplitude of more than 5 mm in nearly half of the patients with average tumor motion amplitudes greater than 7 mm and intrafractional changes in the motion amplitudes of up to 10 mm, increasing with total motion amplitude. Typical baseline drifts of greater than 5 mm in cranio-caudal direction were reported over the course of treatment for lung tumors and baseline drifts greater than 2 mm were reported for liver lesions. Consequently, dose calculation algorithms, which are able to handle complex motion patterns, are needed to investigate and accurately assess treatments with various motion mitigation techniques and to determine adequate safety margins during planning.
Current online imaging and motion monitoring methods are not sufficient to verify 4D dose calculations and do not measure directly stopping powers along the entire beam path. 4DCT images cannot be acquired for the time span of an entire treatment delivery, due to the unacceptably high doses and required imaging frequency [84], even though techniques to reconstruct 3D CT images from 2D cone beam CT images were presented [53]. Tumor motion itself can be monitored directly using 4D cine MRI [45], ultrasound [92], and fiducial markers [93] or indirectly by measuring a surrogate signal with known correlation to the tumor position [94]. Reviews about imaging techniques in particle therapy can be found in the literature [73, 95, 96]. Online images, such as cine MRI and cone beam CT images, do typically not include deformations of the surrounding tissues directly. In order to deduce the resulting changes of the penetration depth of the ion beam, the obtained images have to be translated into stopping powers by registering them to a CT image.

To overcome this problem, Phillips et al. [97] proposed a method that deduces water equivalent path lengths (WEPLs) from a single CT and translates them into a beam-specific WEPL space. Tumor motion is then simplified as a translation in the WEPL space and deduced from surrogate data. Deformations of the surrounding tissue are neglected. Meschini at al applied this method to RBE-weighted dose calculations for carbon beams [98, 99]. The reduction of needed 4D imaging of the tumor makes this method applicable only for dose calculations based on 2D information about the tumor motion. That data can be recorded during treatment, which makes this method clinically applicable. However, this method is limited in case of strong soft tissue deformations.
Full information about geometry changes is necessary and already available in two kinds of application: First, simulation studies can be used to identify tumor locations with critical dose degradation due to irregular motion. The required long image sequences can be created by using deformable image registration based on one reference 3DCT and time-resolved magnetic resonance imaging (4D-MRI) data [100, 101]. Alternatively, image sequences can be generated with virtual phantoms, such as the 4D extended cardiac-torso (XCAT) phantom [102], which was used in this study. Second, testing and benchmarking of new motion mitigation techniques can be done in simulations and experiments with simplified and anthropomorphic phantoms [103, 104, 105]. In this case, detailed information about the phantom motion is known and virtual CTs can be generated.
For densly ionizing irradiation, the biological effect on irradiated cells is higher than for a photon irradiation with the same dose. The concept of relative biological effectiveness (RBE) and RBE-weighted doses links absorbed ion and photon doses with the same biological endpoint. For protons, a constant cell killing RBE of 1.1 can be assumed [106]. For carbon beams, in contrast, the RBE depends on many factors as the particle spectrum and local energy transfer (LET) and is non-linear with dose [22, 107, 108, 109]. Consequently, dose warping from on phase CT to a reference CT cannot be applied. Instead, the contributions of single pencil beams need to be added properly in the reference CT.
The objective of this study was to provide an experimentally validated dose calculation algorithm that can calculate absorbed and RBE-weighted dose distributions on arbitrarily long sequences of CT images, as well as giving an example of the workflow to apply this algorithm in simulation studies.

3.2 Materials and methods

In order to be able to calculate doses on an arbitrarily long sequence of CT images, the treatment planning system TRiP98 developed at GSI [22, 23, 34, 107, 110] was modified. The changes are described in section 3.2.1. We experimentally validated the calculations of absorbed dose distributions for irregular motion, described in sections 3.2.2 and 3.3.1. Finally, we applied the algorithm for RBE-weighted dose calculations to a virtual phantom as described in sections 3.2.3 and 3.3.2.

3.2.1 The dose calculation algorithm

The TRiP98 4D-dose calculation algorithm [34] was designed for the calculation of biologically effective doses in particle therapy on 4DCT imaging data, which were assumed to be periodically repeating. The required data therefore consist of the 4DCT and corresponding transformation maps relating the several motion states to one reference state. This limited amount of data can be read at once and held in memory during the entire dose calculation. In the case of irregular motion, CT sequences covering the entire course of treatment can be substantially larger. In order to handle the additional amount of data, the 4D-dose calculation algorithm was altered to sequentially calculate the dose contributions of the motion states and only hold the data necessary for the current motion state in memory.

In this section, the order of calculation steps in the existing dose calculating algorithm is outlined. Then, the changes made to the algorithm are detailed.
The relative biological effectiveness is defined as the ratio of a photon dose and a particle dose yielding the same biological effect. In order to calculate the biological effect of an irradiation with ions, the dose dependent cell survival S is estimated with a linear-quadratic model (LQM) [19, 20]:

$$S(D) = \exp(-\bar{\alpha} \cdot D - \bar{\beta} \cdot D^2). \tag{3.1}$$

For the 4D dose calculation, an irradiation of points on a 4-dimensional grid is assumed. The first coordinates of a spot, labeled by index i, is the motion state s during which it was irradiated. The other coordinates are the position x_i and y_i in the iso-energetic slice (IES), which corresponds to the initial beam energy B_i. In order to take into account the entire particle spectrum, the dose averaged coefficients

$$\bar{\alpha} = \bar{L}^{-1} \left(\sum_l w_l \frac{dE}{dx}(l) \alpha_l \right) \tag{3.2}$$

$$\sqrt{\bar{\beta}} = \bar{L}^{-1} \left(\sum_l w_l \frac{dE}{dx}(l) \sqrt{\beta_l} \right) \tag{3.3}$$

with the normalization factor

$$\bar{L} = \sum_l w_l \frac{dE}{dx}(l) \tag{3.4}$$

are calculated based on the local effect model (LEM) [22] in the low dose approach. As described by Krämer and Scholz in [107], the virtual index l of the beam component comprises the irradiated raster spot i, particle type T, energy E and the water equivalent depth of the beginning and end of the corresponding voxel in the body. The weight w_l represents the number of particles with these properties that contributes to the dose. The particle spectra in T and E and the resulting contributions L_{ik}, α_{ik} and $\sqrt{\beta_{ik}}$ were precomputed for available initial beam energies and water equivalent depths k and stored in a data base. This reduces the calculation of the dose averaged coefficients to

$$\bar{\alpha} = \bar{L}^{-1} \sum_i N_{spot,i} \sum_k \zeta_{ik} \alpha_{ik} \tag{3.5}$$

$$\sqrt{\bar{\beta}} = \bar{L}^{-1} \sum_i N_{spot,i} \sum_k \zeta_{ik} \sqrt{\beta_{ik}} \tag{3.6}$$

$$\bar{L} = \sum_i N_{spot,i} \sum_k \zeta_{ik} L_{ik}. \tag{3.7}$$

Here, $\zeta_{ik}, k = 1, 2$ is the weight in a linear interpolation for the voxel between precomputed water equivalent depths before and behind the actual depth. In the standard algorithm for periodic motions, computation proceeds voxel by voxel on one CT defined as reference. The loop over the motion states is nested inside the outer voxel loop. The changes in voxel position between the reference CT and other motion state CTs are looked up from a precalculated transformation map. The sums in equations (3.5) to (3.7) are updated by calculating their addends on the corresponding state CTs. Finally, the normalization of equations (3.5) and (3.6) is performed. The physically absorbed dose in the reference state CT voxel is given by

$$D_{phys}(\text{Gy}) = C \cdot \bar{L}(\text{MeV}/(\text{g}/\text{cm}^2)) \tag{3.8}$$

with $C = 1.602189 \cdot 10^{-8}$. From equation (3.1) follows the biological effect

$$-\ln S = \bar{\alpha} D_{phys} + \bar{\beta} D_{phys}^2. \tag{3.9}$$

The RBE-weighted dose is then determined by finding the x-ray dose with the same survival S as the one calculated for ions by inverting equation 3.1:

$$D_{bio} = \sqrt{-\ln S/\beta_X + (\alpha_X/(2\beta_X))^2} - (\alpha_X/(2\beta_X)). \tag{3.10}$$

Final results are stored into a grid with the same dimension as the CT image and then, computation proceeds for the next reference CT voxel.
To perform dose calculations considering irregular motion, long series of CTs and transformation maps need to be handled. This is achieved by treating the motion states sequentially. This means that the loop over the motion states is changed to be the outer-most one. Inside each motion state, all possible calculations proceed voxel by voxel. In the following, the necessary changes to the algorithm are described. The normalization of equations (3.5) and (3.6) can only be performed when the treatment was completed and, thus, the sum in equation (3.7) was completed too. In order to collect the contributions to those three equations, additional three CT sized grids are introduced. To reduce the amount of required working memory for the motion state loop, only the CT and transformation map for the currently considered motion state are held in storage. The contributions to equations (3.5) to (3.7) (without normalization) were calculated for all points irradiated during this motion state, mapped to the corresponding position in the reference state and added to the corresponding grids. After iterating over all motion states, the normalization of equations (3.5) and (3.6) is performed and physical and RBE-weighted dose distributions in the reference state are computed using equations equations (3.8) to (3.10). In order to study the dynamics of an entire delivery, an output of results for single motion states was implemented. For this, one slice of the reference CT can be selected. The dose absorbed in this slice during each single motion state is stored. These slices were then appended to form a new CT where the slice index indicates the motion state. In the same manner, an integral slice, showing the physical dose that was accumulated up to the indexed motion state, was also stored in order to reconstruct the build-up of the absorbed dose over time.

3.2.2 Experimental validation

For the experimental validation, the goal was to test if the modified dose calculation algorithm is able to reproduce inhomogeneous dose distributions caused by the interplay between scanned beams and irregular motion patterns. Experiments were performed at the horizontal beam line in treatment room 1 at CNAO, Pavia, Italy. The experimental setup is schematically displayed in figure 3.1. A 2D ionization chamber (IC) array detector (PTW Octavius 1500XDR; PTW, Freiburg, Germany) was mounted on a programmable linear stage (PI M-414.2PD, controller PI C-884.4DC; Physik Instrumente, Karlsruhe, Germany). The detector consists of 4.4x4.4x3 mm^3 big IC chambers in a chessboard like arrangement. Measurements were performed in a time resolved mode with a frame length of 200 ms. It is placed inside a dedicated holder behind 5 mm of PMMA. The linear stage was programmed to move in sinusoidal patterns of the form

$$d(t) = A_k \cdot \sin^2\left(\frac{\pi}{T_k} \cdot (t - t_{0,k})\right) \tag{3.11}$$

with amplitude and period variations between subsequent periods, each period ranging from one minimum to another. Here, A_k and T_k denote the motion amplitude and period of the of the current motion and $t_{0,k}$ the time of the precedent minimum. The average period T was set to 5 s. Motion periods and amplitudes A_k were varied to uniformly distributed random values in the range $[A - \Delta A, A + \Delta A]$ and $[T - \Delta T, T + \Delta T]$, respectively. A series of seven measurements labeled I to VII with different motion patterns was performed. The motion settings are summarized in table 3.1.
238.63 MeV/u scanned carbon ion beams with 5×10^6 particles per spot were delivered across a 60x60 mm^2

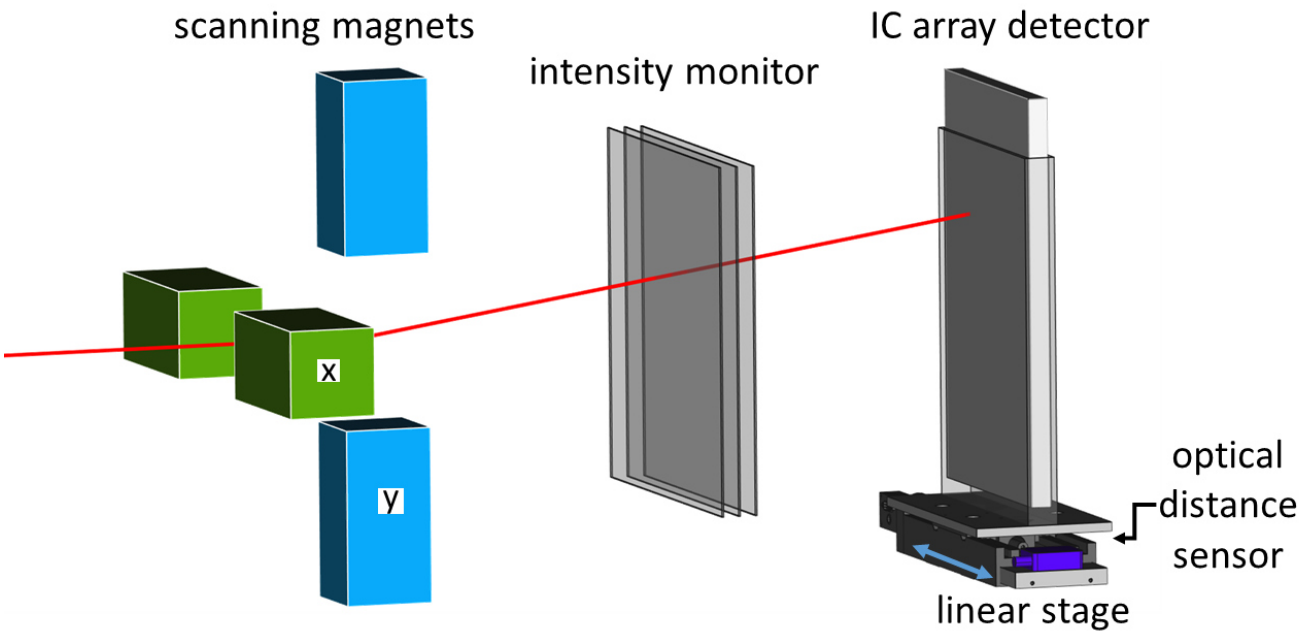

Figure 3.1: Schematic of the experimental setup.

Table 3.1: Settings of the motion trajectory for the seven measurements.

Motion	A (mm)	$\Delta A/A$ (%)	$T(s)$	$\Delta T/T$ (%)
I	10	0	5	0
II	20	0	5	0
III	30	0	5	0
IV	20	25	5	0
V	20	50	5	0
VI	20	0	5	50
VII	20	50	5	50

grid. Spot spacing was 2 mm and the beam was assumed to be Gaussian shaped with a full width half maximum of 5.78 mm. The beam was scanning line by line with alternating direction over the target volume. The motion of the detector was measured with an optical distance laser sensor (SICK OD100-35P840; SICK AG, Waldkirch, Germany).

Each detector time frame was defined as one motion state. The position and number of particles for the beam spots irradiated during one time frame were retrieved from the delivery system log files [10] by a LabVIEW based software developed in house. This delivery information was extracted from the magnet currents of the scanning magnets and the signal from the IC intensity monitor integrated in the nozzle. To synchronize the clocks of the IC array detector and the dose delivery system (DDS), the correlation coefficient between the signal recorded by the intensity monitor and the recorded energy deposition in the IC array detector during the same detector time frames was maximized. To do so, a first estimate of the clock offset was deduced by matching the end of the last frame with measured dose and the timestamp of the last delivered beam spot. Then the correlation was sampled by scanning possible values for the clock offset in range of 2000 ms centered around this estimate with a resolution of 100 ms. The hardware

counts of the intensity monitor were logged by the DDS at every progression to the next raster spot or at least every 50 ms. At the transition between two subsequent detector time frames, the IC counts of the corresponding log entry were split between those time frames according to the time fraction in each frame. In a second step, the scan range was reduced to the range between the sampled value before and after the maximum and the correlation was sampled again, but with a ten fold smaller step size. This procedure was repeated once more to get a final step size of 1 ms. The average detector displacement during one detector frame was used as the translation vector for dose calculations.
The log-files were converted to TRiP98 file format. The absorbed dose distribution was calculated using the new algorithm inside a 1 mm grid in water. The physical dose distribution was calculated and compared to the measurement of the IC array detector in a water equivalent depth of 13.3 mm. This is the sum of the water equivalent thicknesses of the PMMA holder (WEPL=1.15 [111]) and the reference point of the PTW Octavius 1500XDR.
A generalized 3D gamma analysis [112] with local dose criterion was used to quantify the agreement of measurement and dose reconstruction for the expected inhomogeneous dose distribution. The measured dose in each IC was used as reference dose to determine if this IC passes the gamma test. Acceptance criteria of 3 %/3 mm and of 2 %/2 mm were selected. Below a dose threshold of $D_{thresh} = 0.15$ Gy, corresponding to 5 % of the planned dose of 3 Gy that would have been delivered to the homogeneous target region of a static delivery, an absolute dose acceptance criterion of $\Delta D_A = 0.08$ Gy was used. In addition, Pearson's correlation coefficient R between the dose values in the dose reconstruction and the measured IC dose values was calculated. For both comparisons, only IC detectors with a non-zero dose were considered. The evolution of R over the course of the treatment was calculated for the dose distributions inside single detector time frames (in the following called differential dose distributions) as well as with intermediate integral doses up to a given motion state. In order to determine the number of motion states per period required for precise dose reconstructions, the entire dose reconstruction procedure was repeated, binning subsequent detector frames in various multiples to one motion state and the $\gamma(3\,\%/3\,\text{mm})$ pass rate of the final dose distribution was compared dependent on the time resolution.

3.2.3 Dose calculation for irregular motion using a virtual phantom

In this section, a demonstration on how the dose calculation algorithm can be used in combination with a virtual phantom to study the effects of irregular motion on the quality of patient treatments are presented. As a preliminary test of the ability of the dose calculation algorithm, a limited set of $N = 25$ virtual CTs was created using the software XCAT [9, 102]. From this set, a long sequence of images depicting non-periodic motions was created. The procedure is described in the following:
A spherical tumor with a diameter of 40 mm was placed inside the right lung of a phantom (see figure 3.2). 25 virtual CTs depicting half a respiratory cycle from end-exhale (state 0) to end-inhale (state 24) were created. As parameters, a motion amplitude of the diaphragm's dome of 40 mm and an anterior-posterior motion of the rib cage with an amplitude of 20 mm were set and both displacements were set to increase linearly with the state index. The used diaphragm and anterior-posterior motion amplitudes are twice as big as the values recommended for an average breathing cycle. For the respiratory motion during treatment, a motion pattern as proposed by Lujan et al. [113] was selected. During breathing cycle k, so for $t \in [t_{0,k}; t_{0,k} + T_k)$, the displacement d of the diaphragm's dome from its standard end-exhale position in cranial direction was given by the equation

$$d(t) = A_k \cdot \sin^4\left(\frac{\pi}{T_k} \cdot (t - t_{0,k})\right) + d_0 - v_d \cdot t. \tag{3.12}$$

Here, A_k and T_k represent motion amplitude of the diaphragm's dome and period for respiratory cycle k, respectively. d_0 is the start position of the first breathing cycle and v_d is the velocity of a linear baseline drift. Three motion scenarios were considered for the dose calculation:

Periodic: Periodic motion from equation (3.12) with $A_k = 20\,\text{mm}$ and $T_k = 5\,\text{s}$ for all periods and no baseline drifts.

Fixed baseline: Nonperiodic motion, with A_k and T_k randomly generated with a uniform distribution between $\pm 25\,\%$ around $A = 20\,\text{mm}$ and $T = 5\,\text{s}$, and no baseline drift.

Baseline drift: The same motion as in the fixed baseline scenario, but with an additional linear baseline drift of $v_d = 0.015\,\text{mm/s}$.

Treatment delivery progression was simulated for the GSI facility with a constant beam intensity during a spill for single scan deliveries and 20 slice-by-slice rescan deliveries. For the deliveries with a single scan, the irradiation lasted 124 s for field 1 and 128 s for field 2. For deliveries with 20 rescans, the irradiations lasted 804 s for field 1 and 642 s for field 2. Each breathing period was divided into ten motion states of equal length. For each state, the center-of-mass of the displacement of the diaphragm was computed. An offset $d_0 = 12.5\,\text{mm}$ was chosen such that for the baseline drift motion scenario and 20 rescans, the smallest diaphragm displacement corresponds to the simulated end-exhale CT with index 0. All motion patterns started at $d(t = 0\,\text{s}) = d_0$, corresponding to CT number 7. For the dose calculation, this motion state was defined the reference state i_{ref}. The mean diaphragm displacement for each motion state j was calculated and the precomputed state $i = i(j)$ with the closest diaphragm displacement was selected. A series of more than 1000 CTs was created that is a series of selections of the 25 virtual CTs created before.
In addition to the CT images, the corresponding transformation maps, that link the state CTs to the

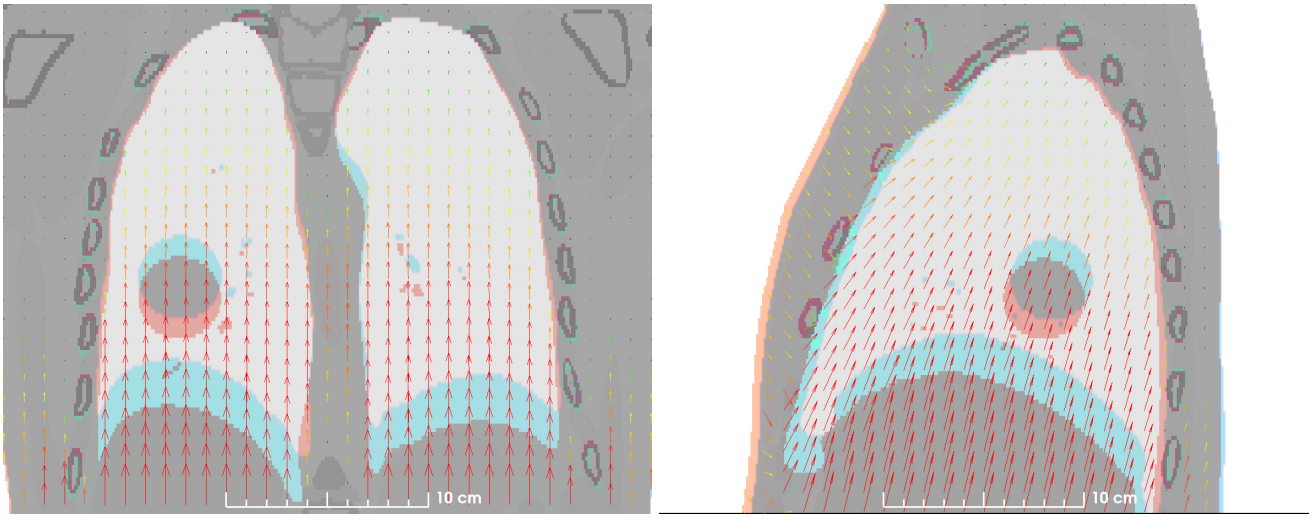

(a) Coronal view (b) Sagittal view

Figure 3.2: Virtual CT containing a spherical tumor created using XCAT. The image shows a superposition of the motion states 7 and 19, which correspond the end-exhale and inhale states of the planned motion. The arrows are used to visualize the corresponding transformation map.

reference CT, are needed. The forward transformation vector fields $i_{ref} \to i$ for $i > i_{ref}$ were directly exported from XCAT. For each voxel in the reference state i_{ref}, they define a vector to the corresponding position in the other states i. For $i < i_{ref}$, the transformation was obtained by mapping from state i_{ref}

to the repetition of state i in a second, identical breathing cycle, $i' = i + N$. In order to get the inverted transformation fields, XCAT was rerun for each motion state i. The state i was assigned to be the start phase and the first repetition of the reference state $i'_{ref} = i_{ref} + N$ was the end state. Now the vector field $i \to i'_{ref}$ was exported. The output data produced by XCAT are the attenuation in binary format for the virtual CT images and vector fields in a text format for the transformation maps. Those files were converted into the corresponding input formats for TRiP98 using a software developed in house. The series of transformation files for the dose calculation was created with the same map $j \to i = i(j)$ as for the corresponding CT images.
For the purpose of treatment planning, the motion was assumed to be periodic. The motion used during treatment planning was split into ten phases of equal length with a mean displacement corresponding to the simulated CTs 7, 8, 11, 15, 19, 19, 15, 11, 8 and 7. This corresponds to a maximum tumor displacement of 9.83 mm in cranio-caudal direction, -3.82 mm in antero-posterior direction and -0.18 mm in left-right direction. The union of the tumor contours in these 10 states was defined as the ITV. Two opposed fields were optimized simultaneously for a homogeneous RBE-weighted dose of 8 Gy in the ITV. The same motion pattern was assumed for both fields. This high dose was selected due to encouraging results in recent dose escalation studies with carbon ions for non-small cell lung cancer [114] and hepatocellular carcinoma [115]. The resulting dose distributions were compared by calculating the DVH metrics such as V_{95}, D_5 and D_{95} on the gross tumor volume. V_{95} is the fraction of the volume which receives a dose $\geq 95\,\%$ of the prescribed dose and quantifies target coverage. D_5 and D_{95} denote the dose that is exceeded in 5 % and 95 % of the target volume, respectively. The difference $D_5 - D_{95}$ quantifies the width of the dose fall-off in a dose volume histogram around the prescription dose. The smaller it is, the more homogeneous is the dose distribution with a mean dose close to prescription.

3.3 Results

3.3.1 Experimental validation

We provide detailed results for each analysis step of measurement VII with motion amplitude and period both varying by 50 % as this is the most complex motion. Final results for all other measurements are listed in table 3.2.
The recorded motion for VII is displayed in figure 3.3.Figure 3.4 shows the correlation between the

Table 3.2: Comparison of dose reconstruction and measured dose distribution for measurements with different average motion amplitude A and variabilities of motion amplitude and period T. The average motion period was always set to 5 s.

Motion	A (mm)	$\Delta A/A$ (%)	$\Delta T/T$ (%)	γ pass rate (%) 3 %/3 mm	γ pass rate (%) 2 %/2 mm	R_{tot}	R_{median}
I	10	0	0	100.00	88.14	0.9924	0.9553
II	20	0	0	100.00	90.00	0.9913	0.946
III	30	0	0	100.00	90.65	0.9889	0.93855
IV	20	25	0	100.00	89.68	0.9915	0.94765
V	20	50	0	99.20	88.00	0.9872	0.94805
VI	20	0	50	100.00	84.13	0.9889	0.9431
VII	20	50	50	100.00	86.78	0.9912	0.9528

measured counts of the beam monitor and the integral dose in the single ICs for each matched frame of

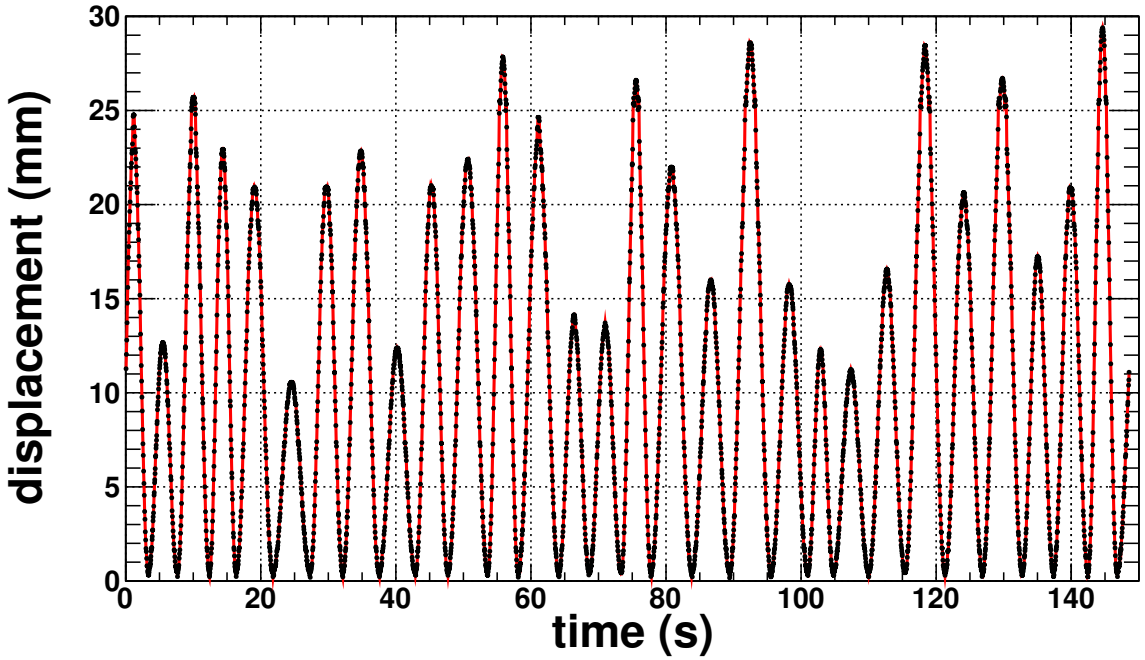

Figure 3.3: Recorded motion of the ionization chamber array detector for measurement VII. Black dots represent measured positions, the red line is an interpolation.

the IC detector array. A squared correlation coefficient of $R^2 = 0.99269$ was obtained.The reconstructed

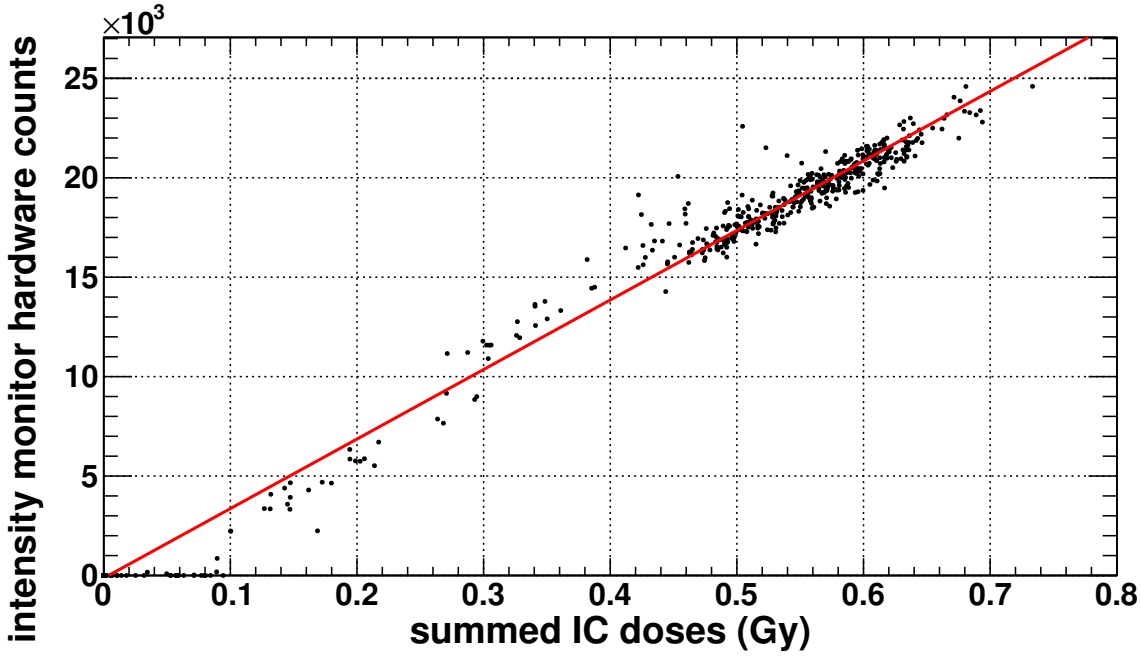

Figure 3.4: Scatter plot showing the measured number of counts in the intensity monitor over the detector response of the IC array detector for each $200\,\mathrm{ms}$ time frame for measurement VII. The red line shows an unconstrained linear fit and was added to guide the eye.

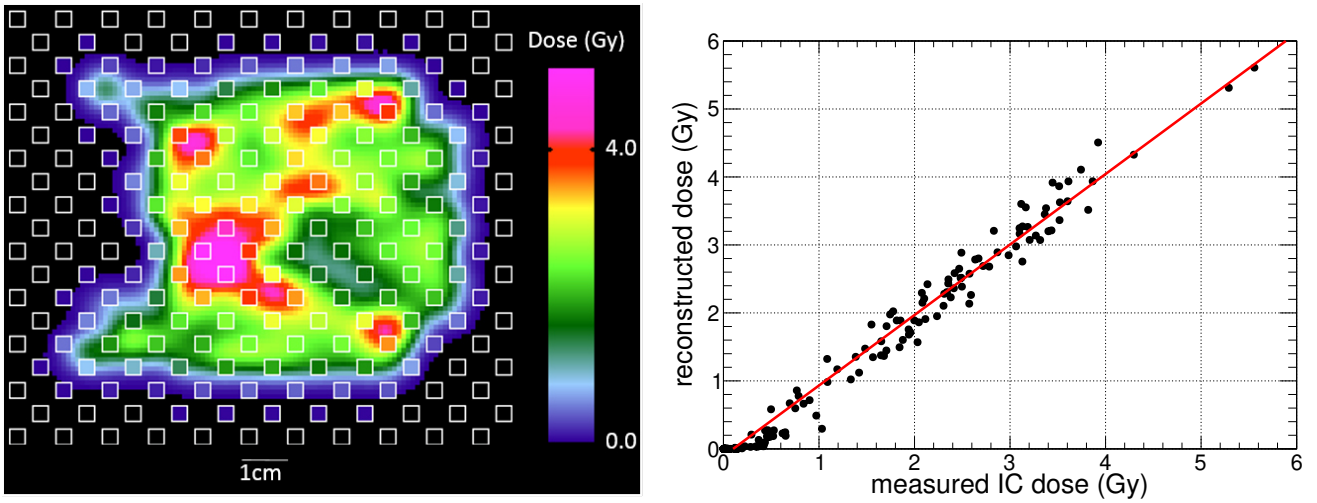

(a) Inset of reconstructed and measured dose distribution.

(b) Correlation of reconstructed and measured dose distribution

Figure 3.5: Comparison of reconstructed and measured dose distribution for measurement VII. (a) The small homogeneous squares in the foreground show the measured dose values in the single ionization chambers (IC). The IC contour size was reduced for better visibility. In the background the reconstructed dose distribution is displayed with 1 mm resolution. (b) Correlation of measured and reconstructed dose distribution for all ICs with measured dose. The red linear fit was added to guide the eye.

dose is compared with the measurement in figure 3.5. The simulated dose was convoluted with the size of the single IC detectors in the array. In figure 3.5a an inset of reconstructed and measured dose is shown. In figure 3.5b the corresponding correlation plot of measured vs. reconstructed dose is shown. A linear regression yields a correlation coefficient $R_{tot} = 0.9912$. The correlation coefficient was also determined for single time frames of the ionization chamber array detector. In figure 3.6, the evolution of Pearson's R over the course of the delivery is displayed. The green dots show the correlation coefficient of the dose only in the single time frames of the detector. The black line shows how the correlation coefficient of the integral dose and the simulation evolves.The results for the integral dose distributions of all measurements are summarized in table 3.2.

The evolution of the correlation coefficient between measured and simulated integral dose distribution is displayed in figure 3.7 for all seven cases. The correlation is stable above 0.9 and converges quickly. All measurements show a common evolution. In figure 3.8, the distributions of correlation coefficients for the differential dose distributions in the single detector frames is shown. Detector frames without dose, which occurred for example during spill pauses, were excluded from the selection.The median of the correlation coefficient for each measurement R_{median} is listed in table 3.2. The dependence of the γ pass rate on the length of each motion state is depicted in figure 3.9. It can be seen that for an average motion amplitude of 20 mm, a frame duration of 400 ms still yielded a pass rate greater than 99 % in all cases. In motion scenario III with an amplitude of 30 mm, in contrast, the pass rate drops already for this frame rate to 97.84 %. For motion I with an amplitude of 10 mm, the pass rate remained 100 % up to a frame duration of 800 ms.

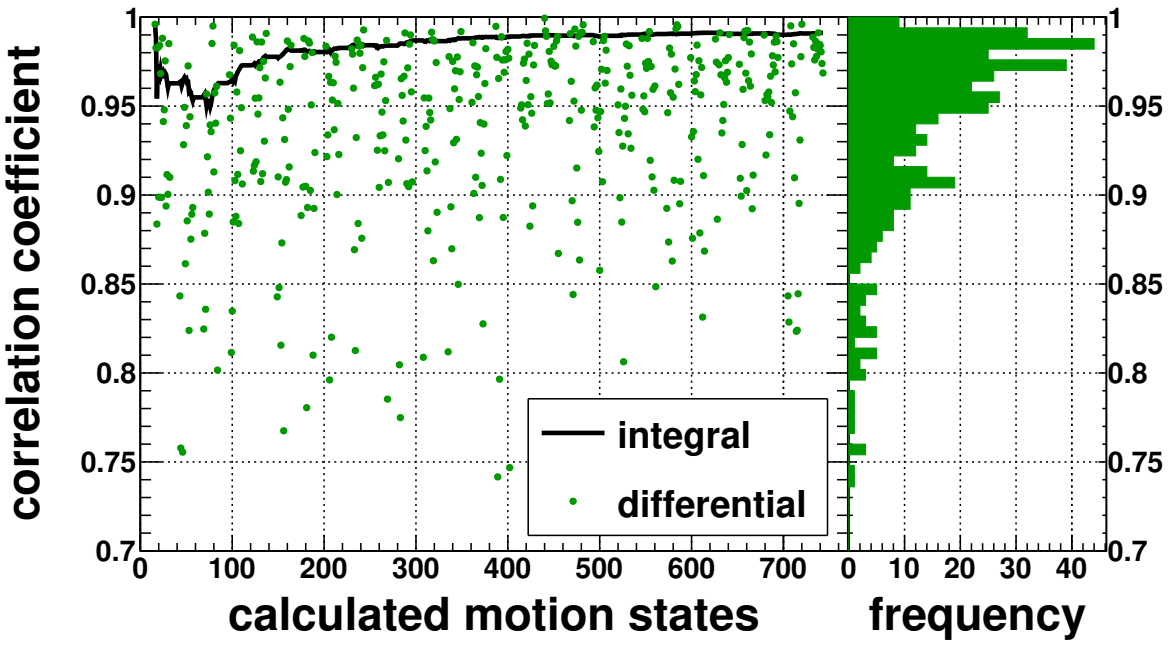

Figure 3.6: Left: Time resolved evolution of the correlation coefficient for measurement VII. Right: Binned projection of the correlation coefficients of the differential measurements on the y axis.

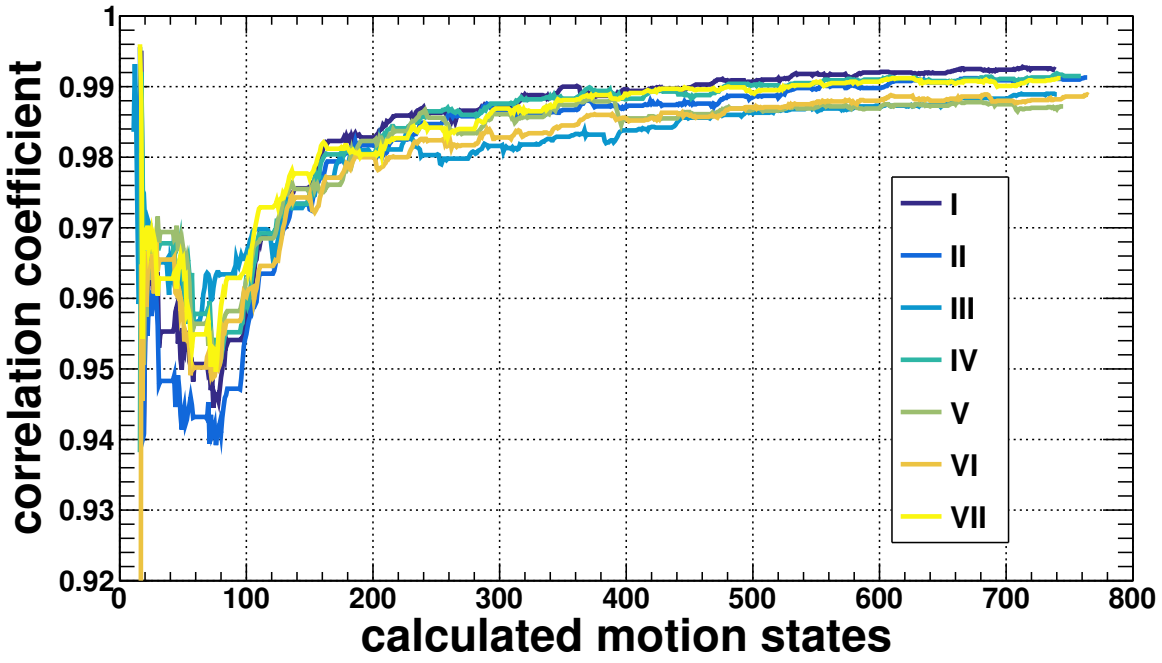

Figure 3.7: Evolution of the correlation between the measured and reconstructed integral dose distributions over the course of the measurements listed in table 3.2.

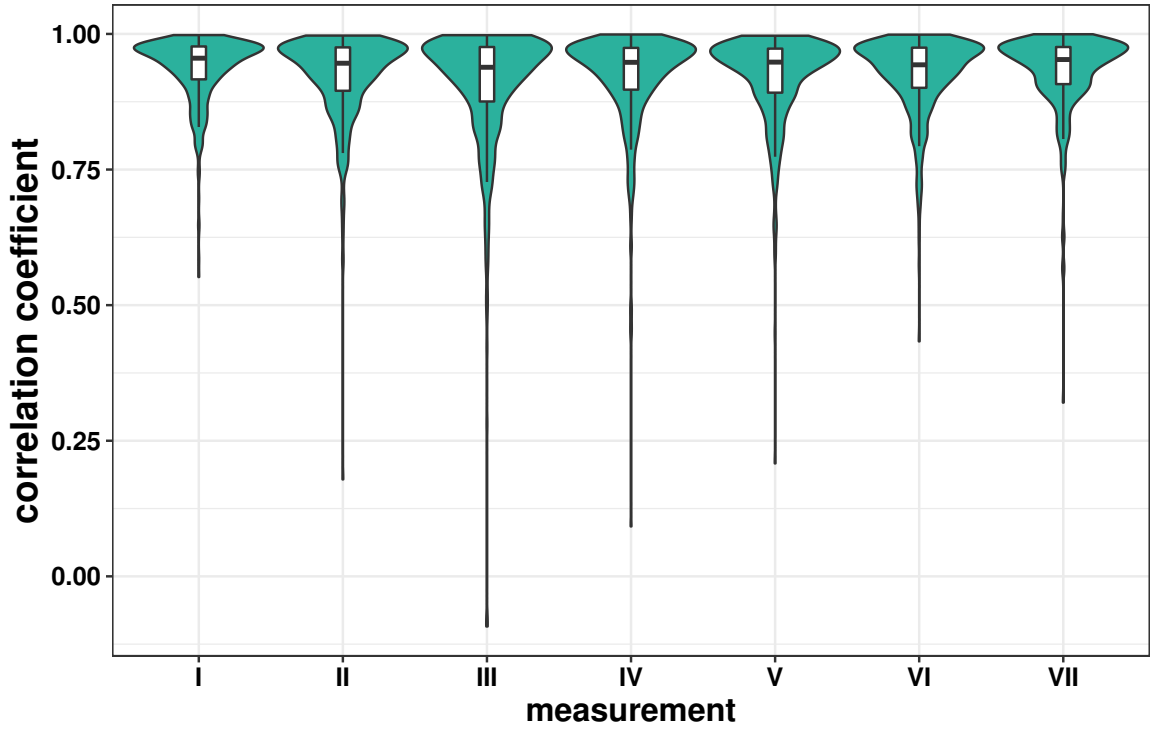

Figure 3.8: Distribution of correlation coefficients between reconstructed and measured differential dose distribution for single detector frames for all seven measurements. The histograms were created the same way as the one on the right of figure 3.6 and are shown as violin plots overlaid with box plots. The horizontal lines depict the median and the boxes the interquartile range of the distribution.

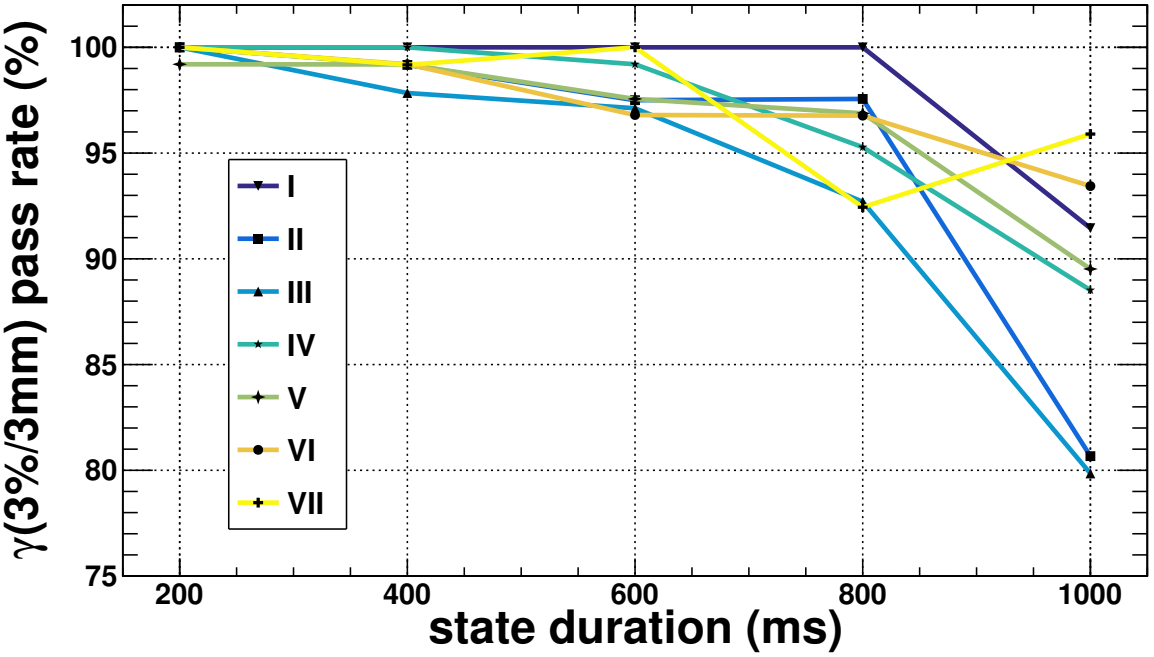

Figure 3.9: Dependence of the $\gamma(3\,\%/3\,\mathrm{mm})$ pass rate on the duration of each reconstructed motion state.

3.3.2 Dose calculation for irregular motion using a virtual phantom

The simulated distributions of RBE-weighted dose for the motion scenarios described in section 3.2.3 are displayed in figure 3.10.

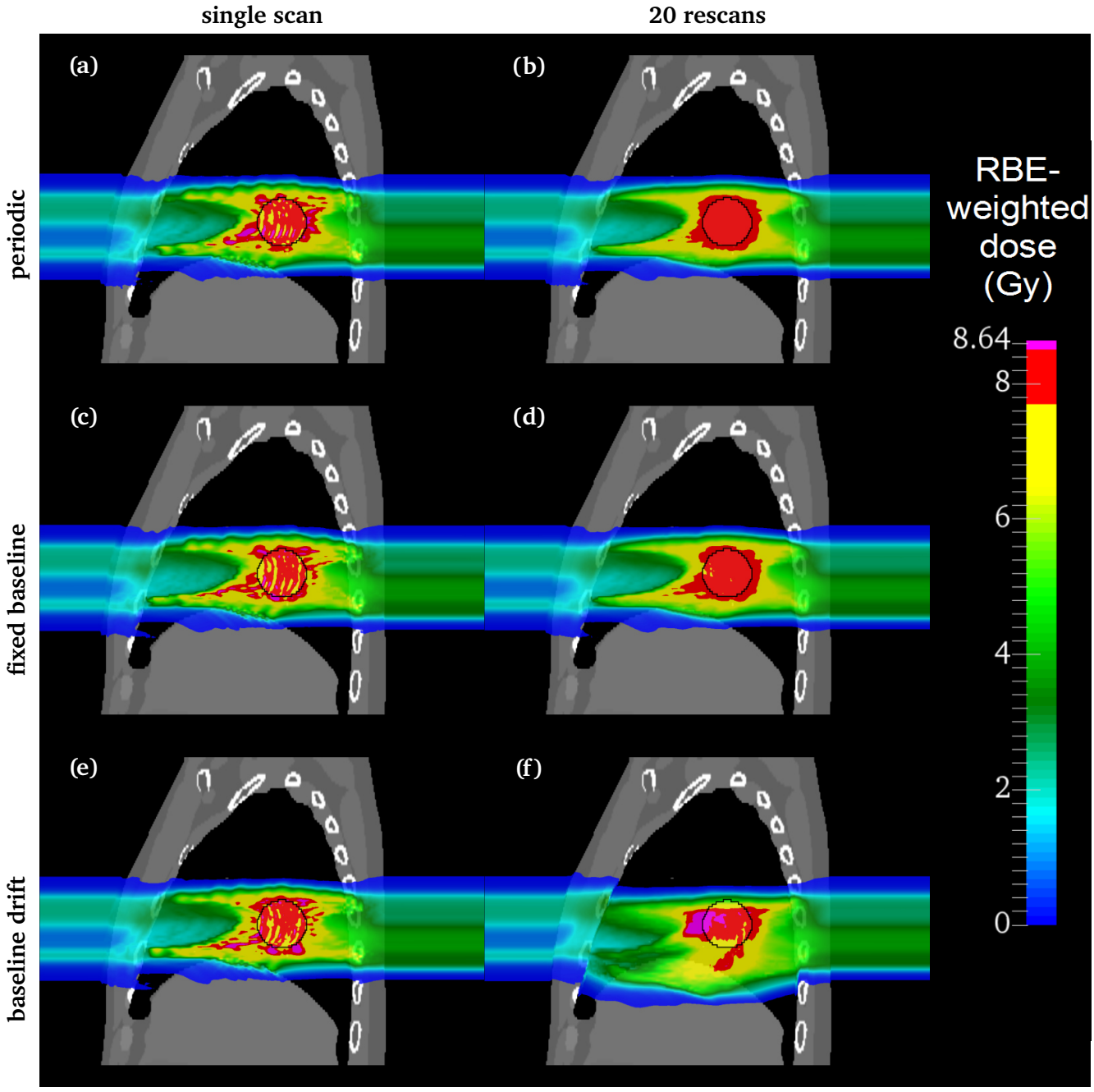

Figure 3.10: Calculated RBE-weighted dose distributions for the three motion scenarios described in section 3.2.3 (a), (c), and (e) for a single scan and (b), (d), and (f) for 20 rescans. The black circle marks the contour of the spherical lesion.

The resulting DVH metrics for D_5, D_{95} and V_{95} are listed in table 3.3. It can be seen, that for the short

Table 3.3: Results of the dose calculation for the three motion scenarios and two treatment modalities, where $HI = D_5 - D_{95}$ depicts the homogeneity index.

motion scenario	# rescans	D_5 (%)	D_{95} (%)	HI (%)	V_{95} (%)
periodic	1	106.9	90.0	16.9	81.2
	20	101.6	96.9	4.7	99.6
fixed baseline	1	102.5	89.0	13.6	76.6
	20	101.4	96.0	5.4	98.5
baseline drift	1	106.4	89.4	17.0	79.0
	20	108.1	89.0	19.1	83.7

single deliveries, the interplay effect causes inhomogeneities of similar size. Rescanning improves dose homogeneity and target coverage in all three scenarios, but for the linear baseline drift scenario, the increased treatment duration causes the tumor to move significantly out of the target volume, causing a lower target coverage of $V_{95} = 83.7\,\%$ (see figure 3.10f).

3.4 Discussion

In this work, we presented a dose calculation algorithm to calculate RBE-weighted doses for complex motion patterns on arbitrarily long sequences of CT images. This algorithm was validated experimentally by performing logfile-based reconstructions of the absorbed dose distributions for seven different motion scenarios and comparing them to measurements with an IC array detector. Excellent agreement between dose reconstructions and measurements was achieved for integral doses as well as for the dynamics of the dose delivery down to the level of single 200 ms time frames. It was demonstrated that the algorithm can be applied for the calculation of RBE-weighted doses by using images from a virtual phantom.
The experimental validation of the dose calculation showed, that the modifications necessary for dose calculations with complex motion patterns cause no relevant additional uncertainties compared to the ones already present for periodic motion. The experimental data strongly supports the reliability of simulation studies performed with the described dose calculation algorithm. In addition, the results demonstrate the high reliability of the methods used to create the log-file based dose reconstructions. In experimental studies, this allows for examination of the quality of a delivery not only inside a detector plane, but also in volumes, for example calculated on a patient 4DCT. Nevertheless, it is recommended to use a detector to verify the quality of the dose reconstruction in at least one plane if possible. This is done for example by Lis et al. [10] for the standard algorithm for periodic motion. Another important finding is that for an average motion amplitude of 20 mm, about ten motion states per period are required to guarantee a $\gamma(3\,\%/3\,\mathrm{mm})$ pass rate greater than 99 %, which corresponds to a state duration of between 400 ms and 600 ms in the measurements presented here. As expected, the required time resolution must be finer for bigger motion amplitudes and can be coarser in the case of smaller amplitudes. This result is in perfect agreement with the one presented by Bert et al. [116] and extends it from regular to irregular motion. Deviations between measured and calculated doses were observed in regions with high dose gradients. This is apparent from the high gamma pass rates. Dose differences are caused by the residual motion during calculated motion states that were not accounted for by the dose calculation. In a clinical case, motion mitigation techniques would be necessary for motion amplitudes as big as the ones used during this study. In a motion compensated treatment, dose gradients are small inside the target regions. Therefore, the precision of the algorithm should be sufficient.

The simulations of the RBE-weighted doses demonstrated a workflow how the virtual phantom XCAT can be used for simulation studies in order to test motion mitigation techniques and to identify tumor locations were the dose distribution is sensitive to irregular respiratory motion. In the given example, the technique of rescanned ITVs was able to deliver a homogeneous dose to a tumor even in the case of variable motion amplitude and period with stable baseline. In the case of a linear baseline drift, in contrast, significant underdosage was observed at the edges of the target volume. This finding underlines the need of sufficient safety margins, an active motion mitigation technique or the restriction of the treatment to a stable gating window [117].

The results of the simulations on the virtual phantom presented in this paper are strongly supported by the experimental validation presented in section 3.2.2 and section 3.3.1. The experimental validation was only possible for absorbed doses and was performed only in one water equivalent depth in the plateau region of the Bragg peak. Nevertheless, it incorporates all motion related features that also apply to the calculation of RBE-weighted doses. The TRiP98 dose calculation algorithm was validated experimentally for periodic motions using radiochromic films [116], ICs in a 3D phantom [34] and cell survival studies [118]. As only the management of motion in the dose calculation was altered and the functionality of this component was shown to work in 2D, we assume that the results can be translated to 3D dose distributions and RBE-weighted doses. Nevertheless, more experiments are necessary and will be published in the future. The results of this work will enable to evaluate the quality of dose distributions during the future development of motion mitigation techniques, capable of handling irregular motion. This is true for both, simulations on virtual or real patient imaging data, and in experiments where it gives information about regions not covered by detectors, dose distributions inside a patient instead of in a phantom and about the time structure of the dose delivery. It was shown that the dose calculation algorithm is able to reproduce the final dose distributions as well as the dynamics of the dose build up during treatment. This makes it possible to identify even the effect of short interruptions of regular breathing like coughing.

The experimental validation of the dose calculation algorithm is limited by the simplicity of the geometry, which was selected for this proof-of-principle study. More measurements with complex or anthropomorphic phantoms [103, 104, 105] would be desirable and will be carried out in the future. However a more complex geometry also makes the interpretation of the measurement data more challenging.

The calculation of the biological doses described in sections 3.2.3 and 3.3.2 are limited to the purpose of demonstrating the abilities of the dose calculation algorithm described in section 3.2.1. Systematic studies about the effect of irregular motion during carbon ion therapy need to be performed in the future. A study with real patient 4DCT-MRI data would allow for a more realistic study [101]. The feasibility to create suitable data sets was demonstrated for another dose calculation algorithm for carbon ion beams [99, 100], even though the amount of work is not feasible for clinical practise now. With further automation, 3D imaging data might become available. For current research purposes, in contrast, XCAT was shown to be a versatile tool to create virtual CT data sets for exploratory studies as it allows for the isolated examination of the effect of different motion patterns as uncertainties induced by imaging, changes in patient anatomy and deformable image registration can be eliminated. The problems in the creation of CT data sets using XCAT described in [119] are known to the authors. The post-processing tool presented in this reference will be included into the workflow for later studies. From the simulations, it is apparent that rescanned ITVs are a possible approach to achieve homogeneous dose distributions and good target coverage for the cases of variable motion amplitudes. But this comes with the detriment, that increased treatment times cause a significant impact of baseline drifts. Robust 4D optimization [33, 78, 87] was proven to deliver homogeneous and more conformal doses faster for moving targets [10]. Developments to combine this technique with residual real time tracking are ongoing [11]. Here, only a linear baseline drift was considered. The used drift velocity for the tumor is in good agreement with the mean trend reported by Takao et al. [38]. Also sudden changes of the baseline position were observed in real patient motion [117].

It is expected that higher variation in baseline drifts will further exacerbate the dose degradation and will pose a challenge in the development of future motion mitigation techniques.

3.5 Conclusions

In this work, we presented an algorithm for 4D dose calculation in carbon ion therapy that is able to handle irregular motion. An experimental validation demonstrated its ability to reproduce measurement data for absorbed doses with high precision. We presented a case study, in which the algorithm was used in combination with a virtual anthropomorphic phantom to perform simulation studies. In the future, this procedure can be used to identify tumor locations with high sensitivity to motion irregularities. The presented algorithm will be used to test motion mitigation techniques as real time tracking [73, 86], 4D optimization [33, 78, 87] and a combination of both [11] in the presence of irregular motion experimentally and in simulations.

4 Implementation of a new motion mitigation strategy that combines 4D optimization and beam tracking

This chapter describes the implementation of a new motion mitigation technique into a dose delivery system used for research at the clinical particle therapy center Centro Nazionale di Adroterapia Oncologica, Pavia, Italy (CNAO) and in the medical cave M of GSI Helmholtzzentrum for Heavy Ion Research, Darmstadt, Germany (GSI). Technical details and first tests are presented that investigate if the implementation is working properly. The clinical impact of the new motion mitigation technique is investigated in the subsequent chapter 5. Extracts of this chapter and large parts of chapter 5 form a submitted manuscript.

4.1 Introduction

Tumors affected by anatomical motion, such as in the lung, liver and pancreas, are responsible for more than 30 % of all cancer deaths in Germany [1]. At the stage of diagnosis, they are often inoperable. Therefore, radiotherapy is often the only treatment option. However, it was shown clinically that current photon treatments of lung cancer are limited by the dose to surrounding organs [4]. It was also shown that the conformity gain by using passively scattered protons instead of photons did not lead to an improved patient prognosis [5]. Consequently, further improvements in the dose delivery are required. Actively scanned ion beams can be used to tailor a dose distribution precisely to a static target volume thanks to their depth dose distribution, the so-called Bragg peak.
As introduced in section 2.3, anatomical motion degrades the delivered doses due to the induced range changes and the interplay between tissue motion and beam scanning. Dose delivery techniques that do not react actively to the anatomical motion rely on internal margins which increase the irradiated volume compared to a static PTV. In order to spare organs in close proximity to moving tumors such as healthy lung and heart, real-time adaptive delivery strategies are required.
Tumor tracking was intensively investigated [54, 57, 73, 75, 120, 121], but not used clinically so far. Lateral tracking of the tumor motion can be relatively easily achieved by adjusting the magnet currents of the scanning system. But this does not lead to satisfactory target coverage due to the uncompensated range changes and tissue deformations.
A common approach in particle therapy to obtain optimal conformity is deformable tracking [54, 75]. For each raster spot, a dedicated tracking vector is calculated. Raster spot specific range changes and the motion of tumor voxels relative to each other are difficult to detect, though. Furthermore, deformable image registration (DIR) is affected by uncertainties, as image contrast is insufficient and there is typically no unique solution [122]. This affects the calculation of raster spot specific tracking vectors before treatment. Real-time measurements of deformation maps using principle component analysis (PCA) [123] also require DIR as input and are therefore affected, too. Thus, a tracking strategy independent of DIR would remove this potential source of error. The tumor center-of-mass (COM) is easier to measure using online imaging, for example with template matching algorithms [46, 55].
Implementations of 3D-deformable tracking that calculate the correction vectors solely from binned, pseudo-static 4D-imaging data recorded before treatment partly loose the ability to adapt to unexpected, irregular

and intra-phase motion. An improved performance was reported for systems using phase based range change information from the planning 4DCT and real-time lateral tracking based on the observed actual motion [120].
An intrinsic problem of spot-wise tracking is that it is often unclear which point to track. The intuitive solution to preserve the position of the Bragg peak in the tissue neglects the dose deposition in the entrance channel and lateral penumbra of the beam. Especially for large spot width, the range change can be significantly different across the spot, but the range per spot can only be corrected with a single value. The real-time correction on a spot-by-spot basis distorts the 3D raster scanning grid for which the treatment plan was optimized [76]. Consequently, deformable 3D tracking does not deliver dose distributions that are substantially superior to simple lateral tracking of the tumor center-of-mass (COM) combined with rescanning [54].
The real-time adaptation of the beam energy of single beam spots by a range shifter system was shown to be technically feasible [74]. However, the latency of such a system requires a minimum delivery time per spot of the order of 20 ms, preventing faster treatments or the combination with rescanning.
This motivates the conclusion that beam delivery strategies are needed that enable the adaptation to range changes without real-time modification of single spot energies and that also preserve the lateral spot grid as much as possible while tracking the tumor motion. Range changes and deformations should be included into a time-resolved 4D treatment plan. This requires a synchronization between the planned delivery progress and the actual tumor motion. The lateral component of the motion can still be compensated by beam tracking of the tumor COM in order to react to unexpected motion. Strategies incorporating rescanning are expected to be more robust against unavoidable deficits in beam delivery and motion monitoring than strategies without.
Recently, the motion mitigation technique 'multi-phase 4D dose delivery (MP4D)' was presented [10, 78, 79, 124, 125]. This technique explicitly compensates anatomical motion expected from the planning 4DCT by switching online between dedicated conformal treatment plans for different motion phases. The synchronization between planned and observed respiratory motion is achieved by a real-time adaptation of the beam delivery sequence. As a homogeneous dose distribution is delivered in each motion phase, MP4D imposes breath-sampled rescanning that implicitly compensates for residual intra-phase motion and random deviations from the expected motion. Each phase plan is optimized individually and independent of DIR using the single phase uniform dose optimization strategy. It was shown that MP4D is able to deliver conformal and homogeneous dose distributions for a periodic target motion, as assumed during treatment planning [10, 79, 124, 125]. However, systematic changes in the breathing pattern, like irregular breathing or baseline drifts, have to be compensated by additional safety margins, spoiling the advantage in dose conformity. It was shown that interfractional motion variation requires lateral safety margins of up to 7 mm to maintain target coverage [80]. Additional intrafractional motion variations including baseline drifts of the respiratory tumor motion can further deteriorate the dose distribution. The aim of this work was to develop a new, improved motion mitigation strategy by combining MP4D with lateral beam tracking to correct for motion variation. In the following, the new proposed strategy is denoted as 'multi-phase 4D dose delivery with residual tracking (MP4DRT)'.
In this chapter, the general approach of MP4DRT is outlined and the technical implementation into the dose delivery system (DDS) of the clinical particle therapy center Centro Nazionale di Adroterapia Oncologica, Pavia, Italy (CNAO), is detailed. Preliminary tests to ensure the functionality of the implementation were performed and are presented here. The DDS does not comprise a specific motion monitoring system. Therefore, the inclusion of clinically available motion monitoring as described in section 2.4 was out of the scope of this work. However, a framework is established to experimentally assess the requirements on the precision of such a system.
In the subsequent chapter 5, potential benefits of the new motion mitigation technique are investigated in

a complex, anthropomorphic phantom anatomy.

4.2 Multi-phase 4D delivery with residual tracking (MP4DRT)

This work proposes a new motion mitigation technique, 'multi-phase 4D dose delivery with residual tracking (MP4DRT)'. It extends the 'multiphase 4D synchronized delivery (MP4D)' technique that was first published as '4D rescanning' or 'single phase uniform dose (SPUD)' approach [78] and was implemented at GSI and CNAO [10]. The concept of this technique was introduced in section 2.5.7, but is briefly described here for the convenience of the reader. The technical details relevant for the understanding of the implementation of MP4DRT into the DDS are detailed in section 4.3.
For each phase $i = 0, ..., N-1$ of a 4DCT with N motion phases, a quasi-static 3D dose optimization is performed aiming for a uniform fraction of the overall target dose. This incorporates position, shape and deformations of the tumor and of organs at risk (OARs). The delivered doses in all motion phases add up to the overall target dose. As the target dose in each phase is uniform, a potentially error-prone DIR is not needed during the optimization. During delivery, the current motion phase $i(t)$, is detected and the dose delivery system (DDS) switches between phase plans without delay. The delivery either continues the irradiation of the treatment plan for the current phase or gates the beam, if the requested phase plan was already completed. The delivery advances to the next energy only after all phase plans were fully delivered. In previous publications, MP4D was experimentally validated for periodic motion taken from the planning 4DCT, for which it was able to deliver highly conformal dose distributions [10, 79, 124, 125].
In MP4DRT, the 4D optimized treatment planning strategy of MP4D is maintained, but the beam delivery is extended by lateral beam tracking of the residual motion. The general idea of MP4DRT is illustrated in figure 4.1.

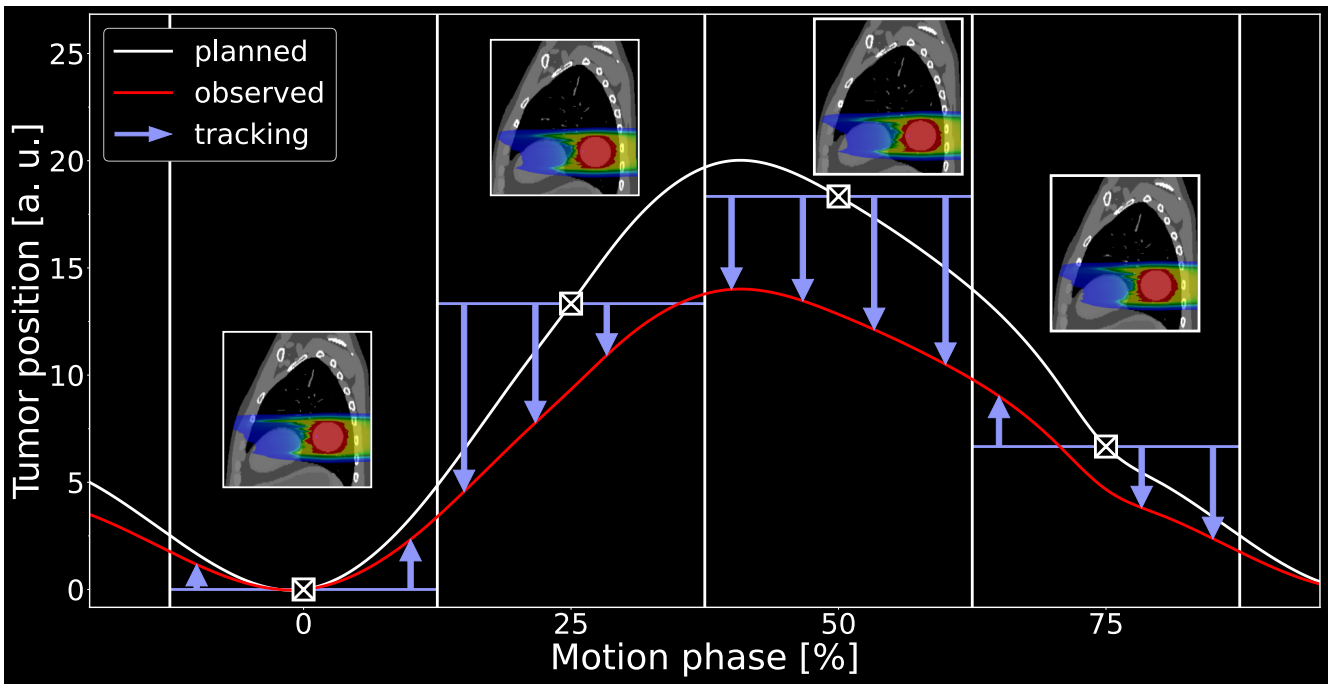

Figure 4.1: The general concept of multi-phase 4D dose delivery with residual tracking. The vertical lines and insets represent the borders of and treatment plans for single motion phases. The lateral tracking of the residual motion illustrated by the blue arrows is the extension on top of MP4D.

Again, there is a dedicated quasi-static treatment plan for each motion phase. In order to react to inter- and intrafractional deviations from the planned motion, like baseline drifts and amplitude variations, lateral beam tracking of the residual, unplanned motion component was added. To do so, not only the motion phase, but also the tumor position has to be determined by a motion monitoring system. The implementation of the new strategy into a dose delivery system is illustrated in figure 4.2.

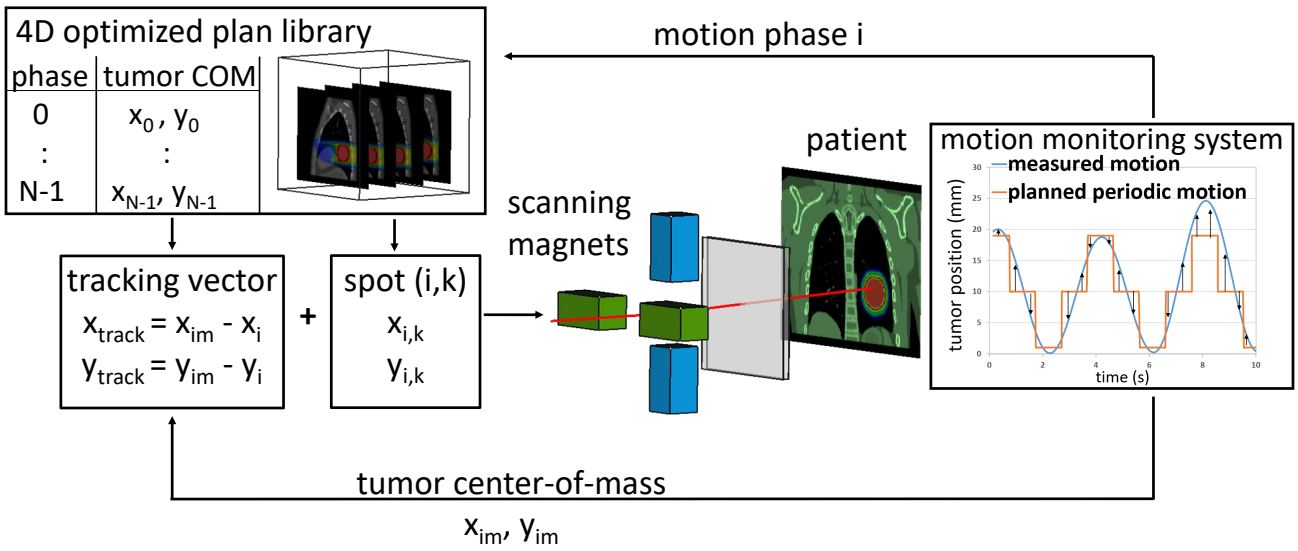

Figure 4.2: Concept of an implementation of multi-phase 4D dose delivery with residual tracking into a dose delivery system: The tumor center-of-mass (COM) is measured by a motion monitoring system. The deviation from the discrete planned COM motion in the planning 4DCT is tracked by adapting the currents of the scanning magnets.

For each motion phase, the planned lateral tumor COM in beam's eye view is defined as the reference position $\vec{x}_i = (x_i, y_i)$. The tumor position is determined continuously by a motion monitoring system, similar as it would be done for conventional lateral beam tracking. In clinical practice, this can be done directly by using an imaging system and extrapolation by a motion prediction algorithm or by a correlation model linking the internal motion to an external surrogate [59, 73, 126]. During delivery, the tracking vector $\vec{x}_{track}(t)$ is calculated as the difference between the observed tumor COM position $\vec{x}_{im}(t)$ and the reference position of the current phase $\vec{x}_{i(t)}$:

$$\vec{x}_{track}(t) = \vec{x}_{im}(t) - \vec{x}_{i(t)}. \tag{4.1}$$

The tracking vector is then added to the planned position $\vec{x}_{i,k_i}$ of the currently irradiated beam spot $k_{i(t)}$ of the treatment plan for phase $i(t)$ to obtain the set value of the beam position:

$$\vec{x}_{beam}(t) = \vec{x}_{i,k_i}(t) + \vec{x}_{track}(t). \tag{4.2}$$

In this way, the currents of the scanning magnets are adapted such that the deflected beam follows the tumor motion. Each phase has its own spot iterator k_i. This implementation also realizes conventional lateral beam tracking, for which the treatment plan library only contains a single phase plan.
The presented approach combines the advantages of MP4D and beam tracking. From MP4D it inherits:

- Conformal quasi-static phase plans
- Compensation of range changes and deformations

- Breath-sampled rescanning with one rescan per motion phase
- Predictability of the out of target dose under the assumption of periodic motion
- A 4D-QA procedure

From beam tracking, it inherits

- Real-time adaptivity to irregular motion
- Compensation of intra-phase motion

This makes MP4DRT a promising candidate for motion mitigation in clinical practice.

4.3 The Dose Delivery System of CNAO

The dose delivery system (DDS) of CNAO is a control system that manages the beam delivery during patient treatment. The beam scanning system including the nozzle detectors are depicted in figure 4.3. A detailed description of the clinical version was published by Giordanengo et al. [127]. A modified research version of CNAO's DDS realizing MP4D was described by Lis et al. [10] and is also in use in the medical Cave M of the GSI [128]. It was further modified in this work to implement MP4DRT.

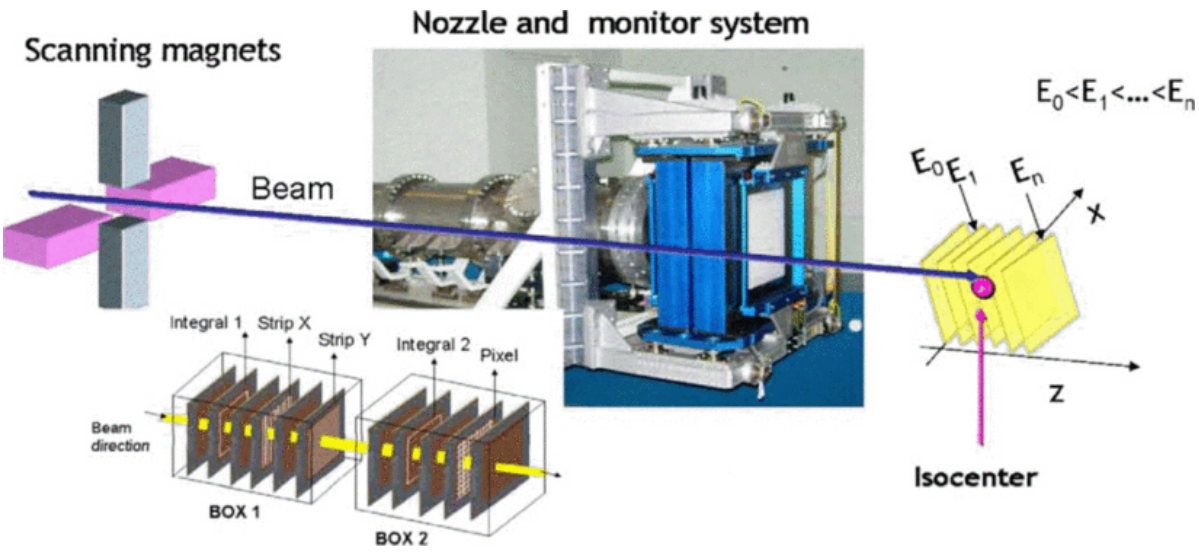

Figure 4.3: The nozzle at CNAO and its detectors. The position detectors Strip X, Strip Y and Pixel and the two integral ionization chambers (ICs) chambers are placed inside the two blue boxes. A ripple filter can be placed on the right after the detectors. Figure reproduced from [129]. ©2011 IEEE

The DDS communicates with nozzle detectors that monitor particle rate and position and steers the scanning magnets. In the following, the components of the DDS important for this work and their tasks are presented. Then, the beam delivery process is described. Afterwards, the technical implementation of MP4D as described by Lis et al. [10] is briefly summarized.

4.3.1 Components

The DDS is programmed in LabVIEW™and has a modular design. The hardware components relevant for this work are a central processing unit (CPU) (PXIe-8840 Quad Core controller) and six field programmable gate arrays (FPGAs) in an peripheral component interconnect eXtensions express (PXIe) crate (PXIe-1085 24GBps; National Instruments; Austin; USA). The host software is called **fast control** and runs on the CPU. It is a state machine that handles tasks for which a microsecond time resolution is not crucial. This includes:

- User interaction.
- Loading of treatment plan including crosschecks of plan validity.
- Conversion of physical units in treatment plan (beam position in mm, particle number) to internal detector units (currents in the scanning magnets, expected strip chamber and pixel detector signal, IC counts).
- Initialization of beam delivery.
- Reading of log messages from the FPGAs via a direct memory access (DMA) FIFO. The log messages are written by the fast control to log-files, the so-called dose delivery data (DDD) files. The log-messages are also published to a user interface called local control room.
- Post processing of log files including safety checks.

The delivery process, as well as communication with detectors and scanning magnets, is handled by six FPGAs. The data flow already including the new elements for MP4DRT is illustrated in figure 4.4. The FPGAs have the following tasks:

- **Memo FPGA** stores the treatment plan and sends the corresponding set values to other FPGAs. It is also the interface to receive motion information.
- **Int FPGA** reads the signal of the two integral ionization chamber detectors in the nozzle. It is the main event and interlock handler and gives the command when to proceed with the next raster scanning spot or create log-files in case of a timeout.
- **Scan FPGA** sets and measures the currents in the two scanning magnets of the nozzle. Magnet currents may be adapted by a feedback loop with position information provided by the Pos1 FPGA. The scan FPGA also communicates with a chopper magnet that can be used to gate the beam.
- **Pos1 FPGA** reads out the beam position from a strip chamber detector in the nozzle and provides the position information to scan FPGA for the feedback loop. It can interlock the delivery if the beam deviates too much from the set position.
- **Pos2 FPGA** reads the beam position from a pixel detectors Strip X and Strip Y in the nozzle and provides redundant information to Pos1 FPGA.
- **Timing FPGA** communicates with the accelerator system. It is omitted in figure 4.4 for better readability.

4.3.2 Beam delivery process

During delivery, iso-energy slices (IESs) are irradiated sequentially in order of increasing beam energy. The beam delivery process of each IES is illustrated in figure 4.4 including the additional elements described in section 4.3.3 and section 4.4. The following elements describe the sequence for a delivery without real-time adaptation:

1. **Start of slice:** The memo FPGA sends IES specific information like the conversion from beam position to magnet currents to the other FPGAs. The beam is requested from the accelerator at the desired energy and intensity.

2. **Spot selection** The Memo FPGA picks the next spot to be delivered. Without MP4D and MP4DRT this is simply the next spot in the treatment plan.

3. **Spot setting:** The Memo FPGA sends initial set values for the selected raster spot to the other FPGAs. Those are the expected number of IC counts N for Int, the scanning magnet currents $\vec{I} = (I_x, I_y)$ for Scan, and the lateral spot position $\vec{x} = (x, y)$ for Pos1 and Pos2 FPGA.

4. **Spot delivery:** Pos1 FPGA measures the beam position and sends the displacement from the set value $\delta\vec{x}_{corr}$ as feedback to Scan FPGA, which adapts the currents in the scanning magnets accordingly by $\delta\vec{I}_{corr}$. Int FPGA reads out the ICs to check if the spot was already completed and waits for a timeout which is usually set to 50 ms. In case of those events, the sequence proceeds to the event handling.

5. **Event handling:** Int FPGA informs the other FPGAs via a backplane trigger line of the PXIe chassis about the event. Int, Scan, Pos1, and Pos2 report current measurement values via DMA FIFOs to the fast control, which writes the messages to a DDD log-file. In the case of a timeout event, the spot delivery is continued. If a voxel was irradiated completely, the DDS proceeds with a new stop. The delivery sequence ends with the completion of the last spot.

6. **End of slice:** The Scan FPGA sends a message to the accelerator to abort the beam.

4.3.3 Implementation of multi-phase 4D dose delivery

The motion mitigation technique multi-phase 4D dose delivery was implemented by Lis et al. [10] and realizes online switching between several treatment plans of a 4D-optimized treatment plan library in order to synchronize the planned beam delivery sequence with the actually observed motion. This had been achieved by adding a new FPGA, the **Motion FPGA**, to the same PXIe crate of the DDS [10]. Its task is the data acquisition and preprocessing of the information provided by the motion monitoring system. It calculates motion phase and trace and forwards the information in a standardized format to the Memo FPGA. It needs to be adapted to handle the signals from different motion monitoring systems. To preserve this flexibility, it is not part of the DDS as a CE labeled medical product. Consequently, it is controlled by its own host VI, the **MotionDAQ** which runs on the same CPU as the fast control, but is disjunctive from the CE certified software. The motion information is logged to a separate file, the motion mitigation data (MMD) file. Data logging is triggered by the same events as the log-file data of the other FPGAs. All elements of MP4D are included in figure 4.4.
The adaptation of the beam delivery sequence is implemented by a modification in state 2.a in the now splitted state 2. 'Spot selection'. In addition, the new state 2.b 'Beam gate', was introduced.
4D plan libraries are organized in a single 4D treatment plan. Each IES of the plan contains the corresponding IESs with the same energy of all phase plans. The treatment plan is stored on a dynamic random access memory (DRAM) in the Memo FPGA. For a single IES n, the same amount of memory $s_{phase}(n)$ is

allocated for each of the phase plans. Consequently, the memory address a of spot k_i in phase i can be computed as

$$a(n, i, k_i) = a(n, 0, 0) + i \cdot s_{phase}(n) + k_i \tag{4.3}$$

with $a(n, 0, 0)$ being the first spot address in the plan for phase 0 of the IES. In state 2.a, the Memo FPGA reads the current motion phase provided by the Motion FPGA. It calculates the address a of the current spot k_i in this phase and reads the corresponding set values from the DRAM. If no so far undelivered spot is available in the current motion phase, the beam delivery switches to state 2.b. Memo FPGA requests a beam gate. At CNAO, this is realized by a chopper magnet to which the Scan FPGA serves as intermediate interface. At GSI, another FPGA converts the CNAO timing signals to the corresponding GSI-specific signals and transmits them to the radiofrequency knock-out (RFKO) exciter which is detuned to interrupt the extraction from the synchrotron [128]. The DDS stays in the loop between states 2.a and 2.b until the breathing phase changes and a yet undelivered spot becomes available. It then proceeds to state 3., where the gate is opened. As the beam delivery sequence is not known a priori, the last spot in the IES is labeled on-line by the Memo FPGA to trigger the transition to state 6. 'End of slice' after its delivery (see figure 4.4). During the upgrades presented in this work, a new phase change event was added to ensure the delivery of a beam spot during the right motion phase. This is of special importance if a spot was interrupted by a spill pause. During state 4. 'Spot delivery', the Memo FPGA reads the motion phase from the Motion FPGA. If a phase change appears, the Memo FPGA sends a message to the Int FPGA via a PXI trigger line. The Int FPGA detects if this event coincides with the end of a spot delivery. If not, the current raster spot is aborted. In state 5., the remaining number of particles to be delivered $N - count$ is sent to the Memo FPGA, which updates N of the spot in the treatment plan accordingly and will send it again as soon as the motion returns to the corresponding phase.
The special case of MP4D with a library containing only a single phase plan realizes conventional deliveries without motion synchronization.

4.4 Implementation of MP4DRT and lateral beam tracking

MP4DRT takes over the real-time adaptation of the beam delivery sequence from MP4D, but adds lateral residual beam tracking. This means that also the spot positions have to be updated in real-time.
Figure 4.4 depicts the data flow between the FPGAs and nozzle detectors during MP4DRT deliveries. The following changes were made in order to add the lateral residual tracking on top of MP4D:

Treatment plan: The treatment plan now contains reference target COM positions $\vec{x}_i$ for all motion phases in its header. This is necessary to calculate the residual tracking vectors. A header entry flag activating the lateral beam tracking was added as well.

Motion FPGA: For the calculation of the tracking vectors, a motion trace of the tumor with absolute physical units is needed. For the detection of the motion phase for MP4D alone, arbitrary units for the signal of a motion surrogate had been sufficient. Now, the measured motion trace $\vec{x}_{im}$ is sent in millimeters to the Memo FPGA.

Fast control: The parsing of the treatment plan was updated to handle the adapted plan header. Reference target positions, calibration-dependent conversion factors from physical millimeters to internal detector units, and the flag if tracking is to be applied are set in the Memo FPGA.

Memo FPGA: The Memo FPGA converts the motion signal received from the Motion FPGA into internal machine units and calculates the tracking vector as displacement of the tumor from the phase-specific

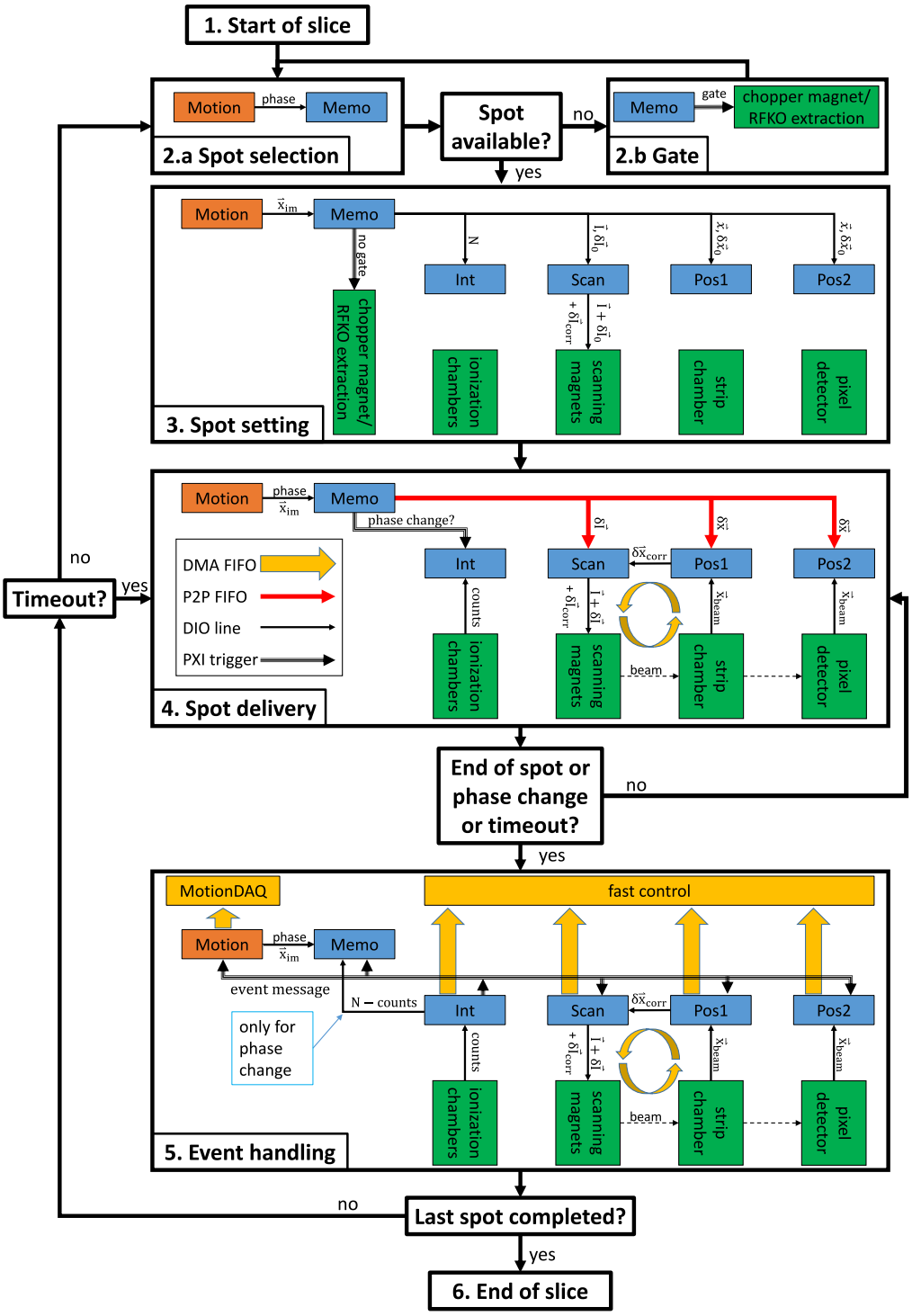

Figure 4.4: Beam delivery process of the DDS for MP4DRT. Blue fields are DDS FPGAs. Nozzle equipment and gating system (chopper magnet at CNAO, RFKO gating at GSI) is labeled in green, the Motion FPGA in red. MP4D is implemented in the spot selection in step 2.a, the gate in state 2.b and 3., and the handling of the phase change event in state 4. and 5. For lateral beam tracking, the following elements were added: In state 3. 'Spot setting', the tracking vectors at the beginning of voxel delivery $\delta\vec{I}_0$ and $\delta\vec{x}_0$ were added. In state 4. 'Spot delivery', the updates of the position tracking vectors $\delta\vec{I}$ and $\delta\vec{x}$ are transfered via P2P FIFOs and applied as set value. MP4DRT contains all elements.

reference position according to equation (4.1). In state 3. 'Spot setting', when providing the new spot information via a digital input/output (DIO) line, initial tracking vectors $\delta\vec{I}_0$ and $\delta\vec{x}_0$ are included in the data packages sent to Scan FPGA, Pos1 FPGA and Pos2 FPGA. During state 4. 'Spot delivery', updates of the tracking vector $\delta\vec{I}$ and $\delta\vec{x}$ are distributed via peer-to-peer FIFO (P2P) as soon as new motion information is provided by the motion monitoring system.

Scan FPGA, Pos1 FPGA and Pos2 FPGA add the tracking vector to the set values of magnet currents and beam position from the original treatment plan. If an update of the tracking vector for the current spot is provided via P2P, it is immediately applied.

Pos1 FPGA shifts the measured beam position of the current raster point by the change of the tracking vector during the delivery of the current point. This is necessary to prevent issues arising from the position feedback loop implemented in the CNAO DDS. Modifying the measured position avoids unnecessary adjustments of the magnet currents in the position feedback loop as the change of current was already implemented into the Scan FPGA and prevents interlocks due to smeared beam spots for beams moved on purpose by the tracking algorithm.

This implementation of MP4DRT already contains lateral beam tracking as the special case of a 4D treatment plan library containing a single motion phase plan.

4.5 Functionality tests

The functionality of the modified dose delivery system was first tested in experiments at the medical Cave M of GSI and later at CNAO. Three questions were investigated:

1. Does the computation of (residual) tracking vectors work correctly?
2. Are tracking and MP4DRT sufficient to mitigate the interplay effect?
3. How sensitive is tracking to errors of the motion monitoring system?

In this chapter, these questions are investigated by irradiating one- and two-dimensional dose patterns onto radiochromic films (gafchromic™EBT3; Ashland Inc., Covington, KY, USA). In chapter 5, the validation in a clinically realistic patient geometry is presented.

4.5.1 Computation of residual tracking vectors

In order to verify the correct computation of the (residual) tracking vectors, the functionality was tested for simple tracking and for MP4DRT in an easy to interpret 1D setup.

1D tests

Vertical lines were scanned with a 290 MeV/u carbon ion beam. The lines were formed by a row of points with 2 mm step size and a total particle number of 2×10^7 per spot that was divided into one, four or ten motion phases depending on the plan. The plans were delivered to radiochromic films on a moving programmable linear stage (PI M-414.2PD, controller PI C-884.4DC; Physik Instrumente, Karlsruhe, Germany). The position was streamed directly from stage controller to the Motion FPGA. Measurements were performed for a periodic sinusoidal motion with an amplitude of 20 mm and a period of 3.9 s. As the simple tracking plans do not include any motion information prior to delivery, only a periodic motion was

considered. For MP4DRT, also an irregular motion pattern with an amplitude variation of ±25 % and a linear baseline drift of 0.03 mm/s was tested. MP4D deliveries were done for both motion scenarios for reference. The films were scanned with a laser scanner (VIDAR DosimetryPRO Advantage Red; VIDAR System Corporation, Herndon, VA, USA) with a resolution of 300 dpi and converted to dose using a calibration curve measured under the same beam conditions.

Results

The calibrated films are displayed in figure 4.5. The RMS of the horizontal projections depicted in figure 4.5

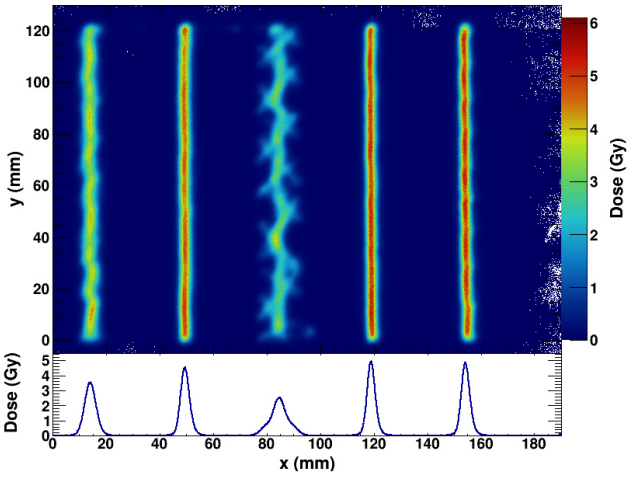

(a) Periodic motion. From left to right: (i) MP4D 10 phases, (ii) MP4DRT 10 phases, (iii) MP4D 4 phases, (iv) MP4DRT 4 phases, (v) tracking (1 phase).

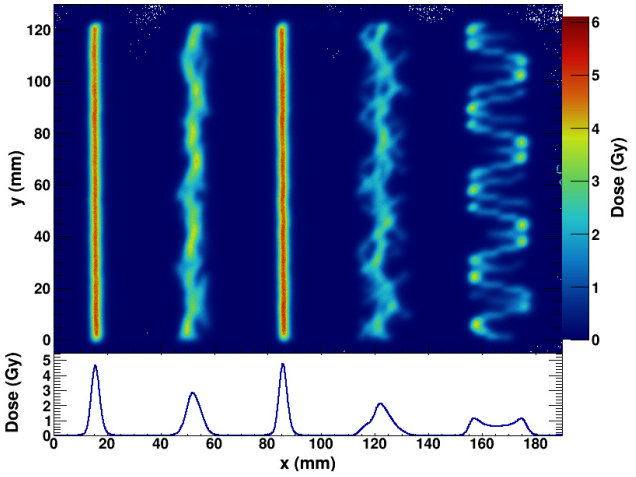

(b) Irregular motion. From left to right: (i) MP4DRT 10 phases, (ii) MP4D 10 phases, (iii) MP4DRT 4 phases, (iv) MP4D 4 phases, (v) interplay with periodic motion.

Figure 4.5: Vertical lines delivered with different motion mitigation techniques. The lower plot shows the x-projection in the y range from 10 mm to 120 mm. The root-mean-squares (RMSs) of the projections are listed in table 4.1.

are listed in table 4.1.

Table 4.1: Root-mean-square of the horizontal projections of the delivered vertical lines depicted in figure 4.5.

Delivery mode	#phases/rescans	motion	RMS (mm)
interplay	1	periodic	7.3
tracking	1	periodic	2.0
MP4D	4	periodic	4.0
	4	irregular	4.2
	10	periodic	2.4
	10	irregular	3.0
MP4DRT	4	periodic	1.9
	4	irregular	1.9
	10	periodic	2.2
	10	irregular	2.0

For deliveries with periodic motion, all motion mitigation techniques show a clear improvement compared to the uncompensated interplay delivery (figure 4.5b(v)). Clearly visible artifacts from intra-phase motion are observed for the MP4D deliveries with both ten and four motion phases, but more pronounced for the latter (figure 4.5a(i) and (iii)). The straight and narrow lines indicate successful motion compensation for the MP4DRT deliveries (ii) and (iv) and simple tracking (v). For irregular motion scenarios, the MP4D delivery with ten motion phases (figure 4.5b(ii)) is clearly more distorted compared to the periodic motion scenario (figure 4.5a(i)). The residual tracking compensates the deviation from the planned motion independent of the number of phases.

Conclusions

The computation of the tracking vectors works for both cases, single tracking and residual tracking (MP4DRT). It compensates for both, intra-phase motion for periodic motion scenarios and for irregular motion scenarios deviating from the planned motion.

4.5.2 Mitigation of the interplay effect

To check if the implemented MP4DRT and tracking are able to compensate the interplay effect, it was tested if it is possible to deliver homogeneous 2D dose distributions.

2D tests

In the same setup as in section 4.5.1, rectangular dose distributions were delivered. The field size was chosen to be 50x60 mm^2 with a raster grid size of 2x2 mm^2 with 5×10^6 particles per spot. For retracking, MP4D, and MP4DRT, the spot weight was divided by the number of rescans or phases, respectively. The following motion scenarios were tested: Static (static delivery and no motion; reference), interplay (static plan with motion and without motion compensation), tracking and four times retracking with periodic motion only, MP4D and MP4DRT, both with four and ten motion phases, for periodic and irregular motion. The scenarios were defined as in section 4.5.1: A 20 mm sinusoidal motion with 25 % amplitude variation and and a linear baseline drift of 0.03 mm/s. In a rectangular region of interest (ROI) of size 40x50 mm^2, the dose inhomogeneity was quantified by the RMS of the dose.

Results

The irradiated films and the regions of interest are depicted in figure 4.6. The measured dose RMS is listed in table 4.2.
The highest dose homogeneity was achieved for MP4DRT with ten motion phases. The result for MP4DRT with four phases is nearly identical to four times retracking. This was also expected as in this setup without range changes, this only corresponds to an alternative calculation of the tracking vectors yielding the same spot positions and a modified timing of the delivery. The dose inhomogeneity decreases with increasing number of rescans or motion phases as remaining errors average out. While for MP4D, the delivery is much more homogeneous for ten phases than for four phases, the difference is small for MP4DRT. The difference for MP4D can be explained by the size of the residual motion and by the number of rescans. For MP4DRT, however, the residual motion is compensated and only the averaging effect of the increased number of motion phases remains. This explanation also holds for the difference between the periodic and the irregular motion scenario. This change only increases the residual motion and therefore the inhomogeneity in MP4D deliveries, but not for MP4DRT.

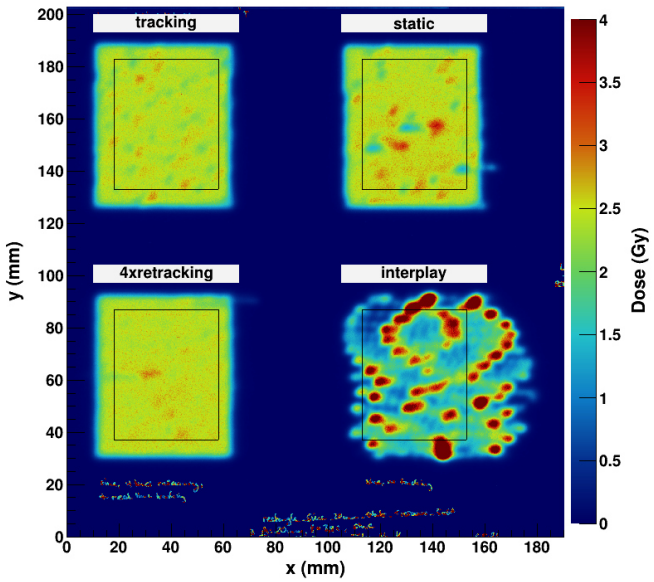

(a) Tracking and no compensation

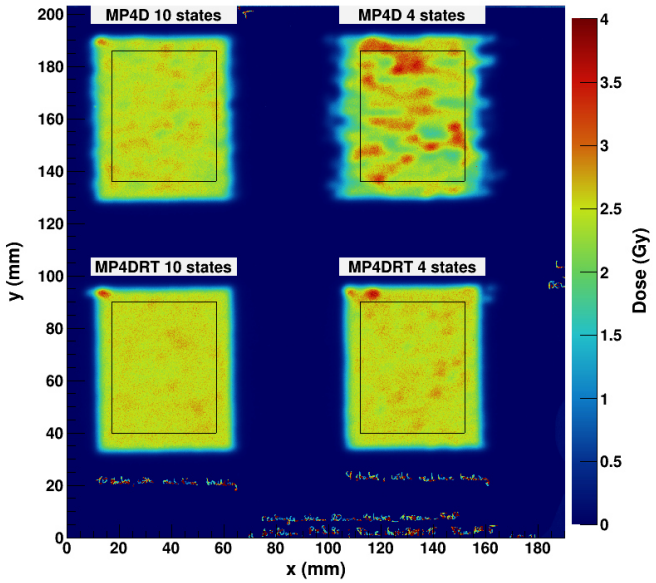

(b) MP4D and MP4DRT for periodic motion

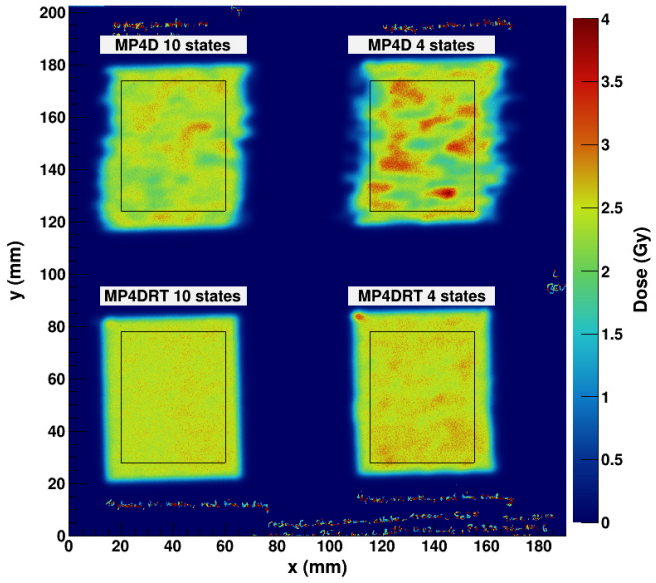

(c) MP4D and MP4DRT for irregular motion

Figure 4.6: Films showing deliveries without motion mitigation, with beam tracking, MP4D, and MP4DRT. (a) (except for static) and (b) show deliveries with periodic motion, (c) for irregular motion. The RMS of the dose in the black rectangles is listed in table 4.2.

Conclusions

For a pure translation, MP4DRT is able to deliver highly homogeneous dose distributions independent of the motion scenario. It reduces the number of necessary motion phases compared to MP4D and makes it robust against deviations from the planned motion. As expected, also (re-)tracking can efficiently compensate for a translation. In general, an increased number of rescans or motion phases improves the compensation of the interplay effect. However, the dose inhomogeneity for the static delivery, which is much higher than for

Table 4.2: RMS of the dose evaluated in the rectangles shown in figure 4.6.

Delivery mode	#phases/ rescans	motion	dose RMS (mGy)	mean dose (Gy)	RMS/mean (%)	film
static	1	-	216	2.47	8.7	1
interplay	1	periodic	718	1.92	37.4	1
tracking	1	periodic	127	2.42	5.2	1
	4	periodic	109	2.48	4.4	1
MP4D	4	periodic	303	2.49	12.2	2
	4	irregular	343	2.42	14.2	3
	10	periodic	123	2.47	5.0	2
	10	irregular	170	2.37	7.2	3
MP4DRT	4	periodic	110	2.53	4.4	2
	4	irregular	114	2.55	4.5	3
	10	periodic	97	2.52	3.8	2
	10	irregular	94	2.48	3.8	3

simple tracking, shows that the beam quality at GSI was not completely stable.

4.5.3 Sensitivity to errors of the used motion monitoring system

The implementation of beam tracking and MP4DRT requires real-time information about the tumor position during the delivery which has to be provided by a motion monitoring and prediction system. Errors in tumor localization lead to the computation of wrong tracking vectors and therefore an interplay effect between the scanning of the beam and the noise of the motion monitoring system. Krieger et al. showed in a simulation study that a specific ultra-sound based motion monitoring and prediction system is sufficiently precise to perform deformable tumor tracking with protons [57]. Here, the amplitude of the error interplay and whether it can be mitigated by rescanning is evaluated experimentally.

Experimental set-up

The option to add artificial noise and latency to the true motion signal was implemented into the motion FPGA. The used imaging noise model is illustrated in figure 4.7. Every 250 ms, a new error vector $\delta\vec{x} = (\delta x, \delta y)$ was generated from a 2D Gaussian distribution and added to the true motion trace. An identical standard deviation σ in horizontal and vertical direction was used. For the 2D Gaussian distribution, σ represents the 2D root mean square error and is connected to the frequently stated mean absolute tracking error TE by the equation

$$TE = \left\langle \sqrt{(\delta x)^2 + (\delta y)^2} \right\rangle = \sqrt{\pi/2} \cdot \sigma \approx 1.25\sigma. \tag{4.4}$$

This procedure mimics a motion monitoring system that takes images with a rate of 4 Hz combined with motion prediction in between images like described in the literature [130, 131].

Tracking and retracking plans were irradiated at CNAO in the same setup as at GSI, but with an additional IC array detector (PTW Octavius 1500XDR; PTW, Freiburg, Germany) behind the films. The standard deviation σ of the noise was set to values between 0 mm and 2 mm. The films were scanned with a flatbed scanner (Epson Expression 10000XL; SEIKO Epson CORPORATION, Suwa, Japan) and the red color channel was converted to dose using a calibration curve. The amplitude of the interplay was evaluated by calculating

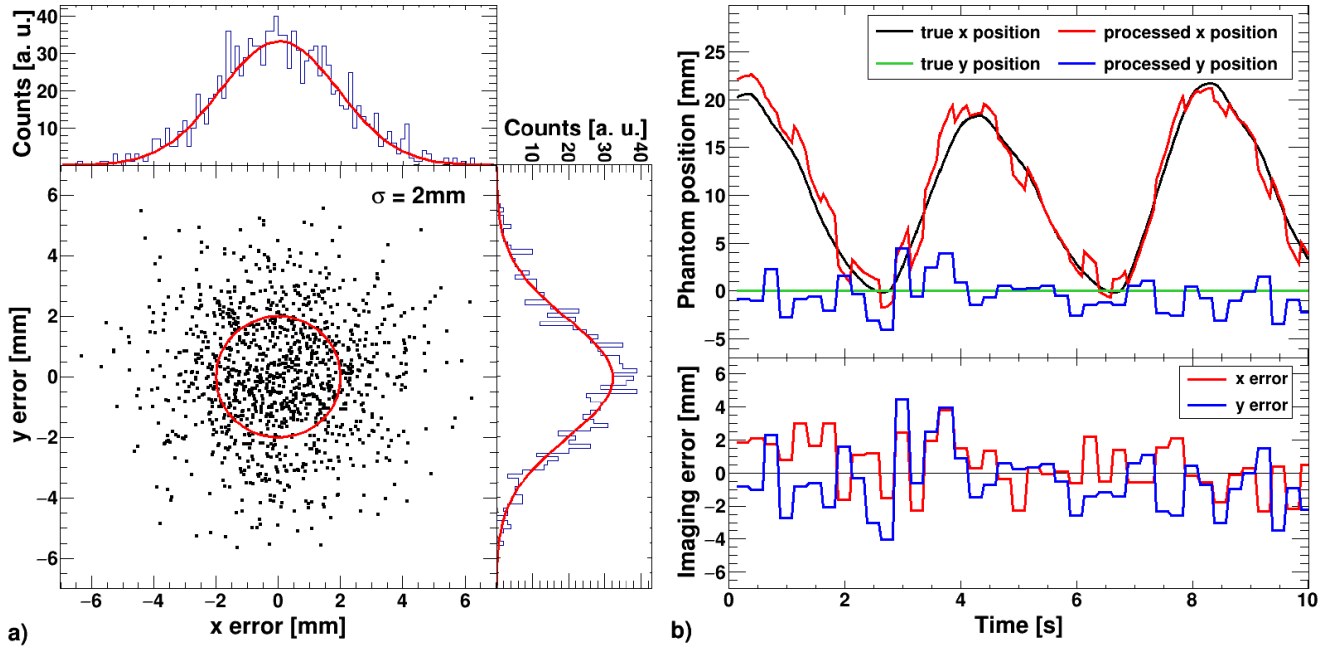

Figure 4.7: Example illustrating the creation of motion traces with artificial motion monitoring errors. a) The tracking error vectors are generated from a 2D Gaussian distribution (Standard deviation $\sigma = 2\,\mathrm{mm}$ in this example). b) New error vectors (lower box) are generated once every $250\,\mathrm{ms}$. The ground truth motion information is received from the motion phantom controller (upper box black and green). The sum of error and true motion (upper box, red and blue) is further processed by the dose delivery system for the computation of the tracking vectors.

the standard deviation of the measured dose in a rectangular ROI divided by its mean. The analysis was performed on both, the films and the IC array detector. The ROI has a size of 35x45 mm^2 and was chosen with the maximal size such that all included ICs are entirely inside the treatment field and not affected by the gradients at the edges.

Results

The calibrated irradiated films and the measured dose RMS on film and IC array detector are displayed in figure 4.8. For perfect motion monitoring, the measured dose distribution was very homogeneous with a slight improvement of the measurement with four rescans compared to the single scan. For both numbers of rescans, the RMS increases strongly with the level of the imaging noise. Rescanning reduces the effect of the imaging noise considerably. Results on the films and on the IC array detector are consistent. The films intrinsically contain some noise due to variations in the density of the active dye and noise of the scanner. Therefore, there is a component of the relative dose RMS on the film that does not vanish even in the case of the dose distribution on the IC array detector being perfectly homogeneous. For a dose distribution that is truly inhomogeneous on a length scale that can be resolved by the IC array detector, the measured dose inhomogeneity on both types of detectors is linearly correlated. Therefore, figure 4.8d was fitted with a function of the form $y = \sqrt{a^2 + (b \cdot x)^2}$ with the coefficients $a = (1.57 \pm 0.17)\,\%$ and $b = 0.746 \pm 0.025$.

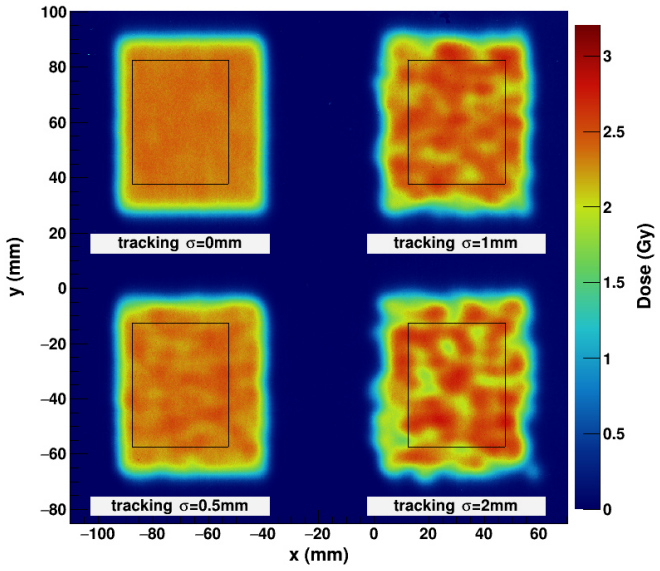

(a) Tracking single scan

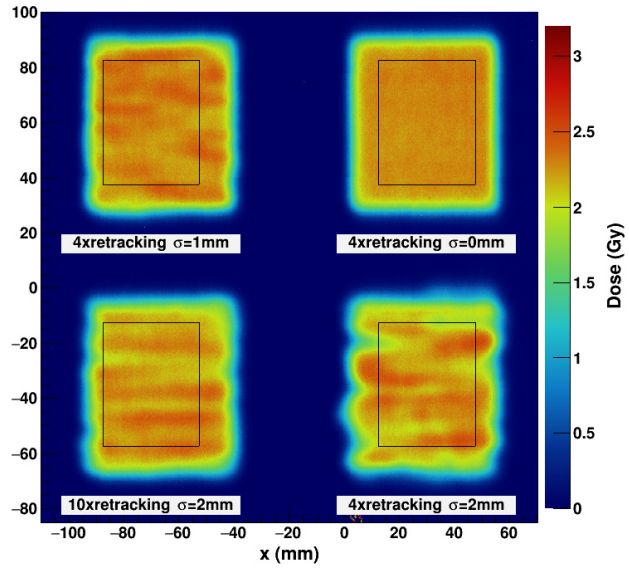

(b) Retracking

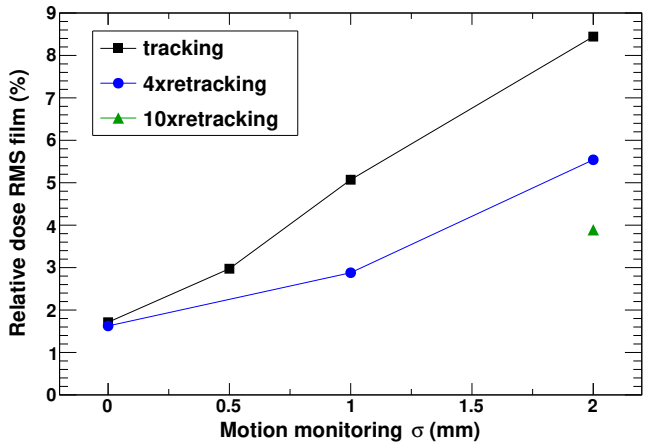

(c) Relative dose RMS on films

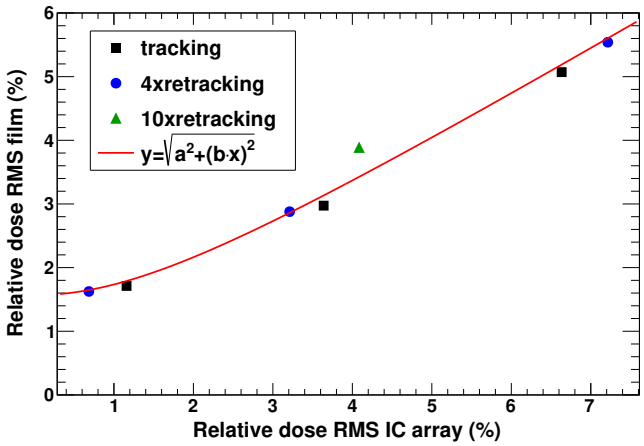

(d) Film vs IC array measurement

Figure 4.8: (a) and (b): Films with tracked film deliveries for 1, 4 and 10 rescans with imaging errors. The RMS of the dose measured in the marked rectangles is displayed in (d) and compared to the RMS of the IC chambers in the same ROI in (d).

Conclusions

The interplay between the scanning of the pencil beam and noise on the motion monitoring signal can strongly affect the homogeneity of dose distributions in treatments with beam tracking. This effect can be efficiently mitigated by additional rescanning. For efficient statistical averaging, the position errors during the subsequent rescans have to be uncorrelated. Consequently, the time span between rescans should be greater then the length between two imaging frames of the motion monitoring system. In this experiment, deliveries took on average (120.9 ± 1.4) s. So, this was given for the rescanning already. Therefore, no significant difference to MP4DRT treatments are expected. In a real treatment, the effect of the motion monitoring errors is expected to affect mainly the distal and lateral edges of the target volume, where only few iso-energy slices contribute. As can be seen on the films in figure 4.8, the errors on the motion

signal affect the contour of the treatment field. To assure target coverage at the edge of the tumor, safety margins have to be increased accordingly [132]. Retracking can help reduce the corresponding safety margin and spare organs next to the treatment field. However, if the particle number in the relevant slices is low and the rescanning therefore faster than the imaging frame rate, errors will not cancel out properly. This problem is resolved in MP4DRT through the intrinsic breath-sampled rescanning. As this is a statistical effect, it can also be mitigated by treating with several fields and by fractionation.

4.6 Discussion

In this chapter, the new motion mitigation technique multi-phase 4D dose delivery with residual tracking (MP4DRT) was presented. It is a synthesis of the conformal MP4D strategy with real-time adaptive lateral beam tracking. In this section, the technical implementation and presented functionality tests are discussed.

4.6.1 The implementation

MP4DRT was successfully implemented into the research version of the dose delivery system of CNAO and used at two carbon ion facilities. However, the strategy can be used for any kind of particle accelerator including proton cyclotrons.
A strength of the presented DDS is its flexibility. With rescanning, lateral beam tracking, MP4D, and MP4DRT, it is able to use four different beam delivery strategies for motion mitigation. This enables comparative studies that so far could only take place with different systems at different therapy facilities having a very diverse system layout. The beam delivery techniques can also be combined with several treatment planning strategies. For example, MP4D with identical treatment plans in each motion phase corresponds to breath-sampled rescanning. A technique that has been shown to bring dosimetric improvements compared to other rescanning techniques [41, 42], but so far lacks a straightforward delivery technique and therefore experimental validation and clinical use. Similarly, identical treatment plans with MP4DRT would correspond to a so far untested breath-sampled retracking.
The modularity of the DDS enables a high portability of the system. This was demonstrated by using the system at two facilities. All hardware is commercially available and can therefore be easily maintained or upgraded. The motion mitigation techniques currently implemented into the DDS are planned to be included into the next iteration of CNAO's clinical DDS [133], which is a CE certified medical product that can be bought by other centers. The current clinical version is in use at CNAO and MedAustron, Wiener Neustadt, Austria. A spread of the DDS and its conversion into a clinical system also facilitates access for patients and research.
The minimal communication protocol between Motion FPGA and Memo FPGA that contains only the transmission of motion phase and tumor COM position in beam's eye view allows a flexible adaptation of the Motion FPGA to any arbitrary motion monitoring system without changing the core FPGAs of the DDS itself. This facilitates the implementation in existing centers and increases the system flexibility, as different motion monitoring systems are suited for different patient sites.

4.6.2 The experiments

All measurements were performed with simple treatment plans for lines and rectangles. On the one hand, this made the results easy to interpret and to show that the technical implementation of MP4DRT is working

properly. On the other hand, it is difficult to translate the results to more complex patient cases with multiple beam energies, range changes, and deformations. Therefore, an experimental study comparing MP4DRT with the motion mitigation techniques MP4D, beam retracking and ITV rescanning on a virtual patient CT was performed and is presented in chapter 5.
The correct calculation of tracking vectors from a motion monitoring signal was verified with vertical lines that were delivered perpendicular to the applied motion. It was shown that MP4DRT is able to efficiently mitigate the interplay caused by translational motion lateral to the beam even on the level of single spots. In contrast to MP4D, it also mitigates intra-phase motion and deviations from the planned motion pattern. The potential reduction of required phase plans in MP4DRT compared to MP4D has a positive impact on clinical applicability as each phase plan requires quality assurance. Therefore, a reduction in the number of motion phase plans corresponds to less workload in the clinic. In addition, less phases correspond to higher spot weights which reduces the required scanning speed.
Lateral beam tracking combined with rescanning showed similar performance as MP4DRT. This was expected, as the experimental set-ups included only translations without range changes or deformations. It was shown that noise of the motion monitoring causes an interplay effect in treatments with beam tracking. This effect can be partially mitigated by rescanning. The results were confirmed by two detector systems that showed consistent results. This underlines the necessity to include the effects of motion detection errors into the evaluation of motion mitigation systems and to define requirements on the precision of the motion monitoring system.
The model used for the motion monitoring errors is a simplistic approach accounting for the temporal correlation of those errors. In a real system, there is an error at the moment when the image is taken. Starting from this value, the accuracy of the motion prediction decreases over time until the next image is taken and processed. The accuracy of motion prediction algorithms is typically assessed by comparing the predicted tumor position with the measured one on the next image [130]. Consequently, comparing this model with stated precision of motion monitoring systems of the same size is a conservative approach, as the worst error was assumed for the whole imaging period. The model includes the temporal correlation of motion detection errors, but it is independent of characteristics of the exact motion monitoring system or the tumor site. Therefore, the results can be easily generalized to an arbitrary motion monitoring system. In contrast to a medical imaging system, the motion monitoring precision in the presented experimental implementation can be set to arbitrary values. At the same time, ground truth motion information is available. This enables systematic, experimental studies of the required motion monitoring precision of any real-time adaptive motion mitigation strategy.

4.7 Conclusions

A new motion mitigation technique combining lateral beam tracking with MP4D was successfully implemented into the research version of a clinical system. Simplified tests demonstrated the functionality of the system in the compensation of target motion and its flexibility to use several motion mitigation techniques. The presented DDS is an efficient tool for comparative studies of different active motion mitigation techniques and to experimentally quantify their requirements on motion monitoring. Such a study is presented in the following chapter 5.

5 Experimental validation of MP4DRT and comparison with other motion mitigation techniques

In the previous chapter 4, the concept and implementation of the new motion mitigation strategy MP4DRT was described. In this chapter, the potential benefits are investigated in an inhomogeneous, anthropomorphic anatomy. MP4DRT is compared with the following motion mitigation techniques: ITV rescanning, lateral beam tracking and MP4D in the presence of irregular anatomical motion. First, a short introduction reviews existing beam delivery strategies designed to mitigate motion. Then, the selected test case and the treatment planning are detailed in section 5.2. Next, the used experimental setup and data analysis strategy are described in section 5.3 and section 5.4. Dosimetric results are presented in section 5.5 and discussed in section 5.6. Large fractions of this and the previous chapter are part of a submitted manuscript.

5.1 Introduction

Locally advanced non-small cell lung cancer (NSCLC) has a poor prognosis with limited treatment options. It is often inoperable and the applicable dose in conventional radiotherapy is limited due to toxicity [4]. Particle therapy, especially with carbon ions, can deliver more conformal dose to the tumor. Highly conformal and accurately delivered treatment beams are essential for aggressive hypofractionated treatment schemes that have yielded promising clinical outcomes in respiratory gated therapy [134] and for immobilized patients [27]. For early stage NSCLC, carbon ion therapy was safely delivered in a single fraction [135].
Treating moving tumors with ion beams necessitates handling several aspects, including range changes, tumor deformations and interplay between motion of the tumor and of the scanned ion beam. Variable breathing patterns during and between fractions [39] and organ drifts [38] cause irregular target motion, with a discernible impact on 4D-dose distributions[81]. Several motion mitigation strategies have been developed [136], but all have drawbacks.
Clinically-used beam gating reduces the active beam delivery time and requires manual intervention to handle organ drifts. Rescanning of the internal target volume (ITV) averages interplay patterns by scanning the ion beam several times over the entire volume, which the tumor is expected to occupy throughout a respiratory cycle. Thus, a substantial dose is delivered to healthy tissue around the tumor [137]. Unfortunate temporal correlation between respiratory motion and beam extraction or too short irradiation time per slice can prevent efficient statistical averaging. Thus, several strategies have been investigated, like phase-controlled rescanning (PCR) [68, 138], breath-sampled rescanning (BSR) [41, 42], and volumetric repainting. While the first two increase treatment time, studies investigating if the latter one provides an advantage over layered rescanning led to contradictory results [70].
Substantial efforts were made to develop beam tracking for particle therapy [54, 73, 75], but they did not lead to clinical use. With this technique, the tumor position is monitored [57, 59, 126] and the beam position is adapted online to follow the tumor. However, this technique cannot properly compensate for range changes in the beam path and deformations of the tumor over the course of the respiratory cycle. Further, differences between the motion of the tumor and tissue in the entrance channel can cause hot spots outside the target volume. This is known as ‘inverse interplay’ effect [75]. The combination of beam

tracking with rescanning is denoted as 'retracking' [54]. In simulations, lateral beam retracking of the tumor COM was shown to deliver dose distributions of similar quality to moving tumors than 3D tracking, but was not able to restore the planned static dose distributions [54, 57].
In the previous chapter 4, the general concept and implementation of the new motion strategy multi-phase 4D dose delivery with residual tracking (MP4DRT) was presented, that combines MP4D with lateral beam tracking. It was shown that the technique is working properly and able to compensate irregular motion in a homogeneous geometry. It was also outlined that the quality of the dose delivery depends on the precision of the used motion monitoring system. However, it was unclear how this translates to 3D volumes for which the contributions from several iso-energy slices overlap and beam spot weights are strongly heterogeneous. In this chapter, the ability of MP4DRT to mitigate irregular motion in an inhomogeneous, anthropomorphic lung geometry is experimentally verified. In order to quantify potential benefits compared to other motion mitigation techniques, treatments were also planned and delivered for the same patient case for ITV deliveries with and without rescanning, lateral beam retracking, and MP4D. The precision and latency of a motion monitoring system required for clinically acceptable target coverage is determined for the online adaptive strategies MP4D, MP4DRT and lateral beam tracking. Also the effect of undetected target rotation on the target coverage was investigated. All experiments were performed at the clinical particle therapy facility CNAO with scanned carbon ion beams.

5.2 Treatment planning

In the following section, the creation of virtual patient CT data and the treatment planning process for the different motion mitigation techniques are described. A quantitative comparison of the treatment plan quality is presented together with the experimental evaluation in figure 5.12 in section 5.5.4.

5.2.1 The virtual test patient

All treatments were planned for a single virtual 4D extendended cardiac-thorso phantom (XCAT) 4DCT [9, 102]. A spherical tumor with a diameter of 50 mm was placed in the lower left lung. In total, 25 states covering a diaphragm motion range of 40 mm were created. The tumor performed a translation along a straight line of 40 mm in CC direction and 10 mm in anterior-posterior (AP) direction with constant step size per state. The conversion into periodic 4DCTs with four and ten motion phases is illustrated in figure 5.1d. For a motion trace with a cranio-caudal (CC) amplitude of 20 mm, the tumor position was deduced at phases equally spaced in time. Based on the CC displacement, the corresponding state CT was assigned to the motion phase. The end-exhale phase was defined as the reference state and assigned to state 7, in which the tumor is placed 12.5 mm from the maximum cranial position to allow for baseline drift in this direction. The in total 20 mm motion range not used in treatment planning in the full 4DCT was used for dose calculation with irregular motion during delivery. Vector fields to all other states and their inversion were exported from XCAT. The left lung and the heart were segmented and defined as organ at risk. The tumor was defined as GTV. The reference state is depicted in figure 5.1 together with a static treatment plan to illustrate the field definition. The inhomogeneity of the geometry was assessed by calculating the water equivalent range changes of all GTV voxels relative to the reference state. The resulting distributions are displayed in figure 5.2. The mean water equivalent depth changes only by 1.34 mmH_2O, which is in agreement with values reported for intrafractional range changes caused by variations of the posterior chest wall [139]. For single voxels variation in water equivalent depth by more than 5 mmH_2O are observed. For a volume including 3 mm isotropic margins around the GTV, range changes of more than 25 mm were observed, which is in agreement with measurements from patient lung 4DCTs [140]. The XCAT patient can

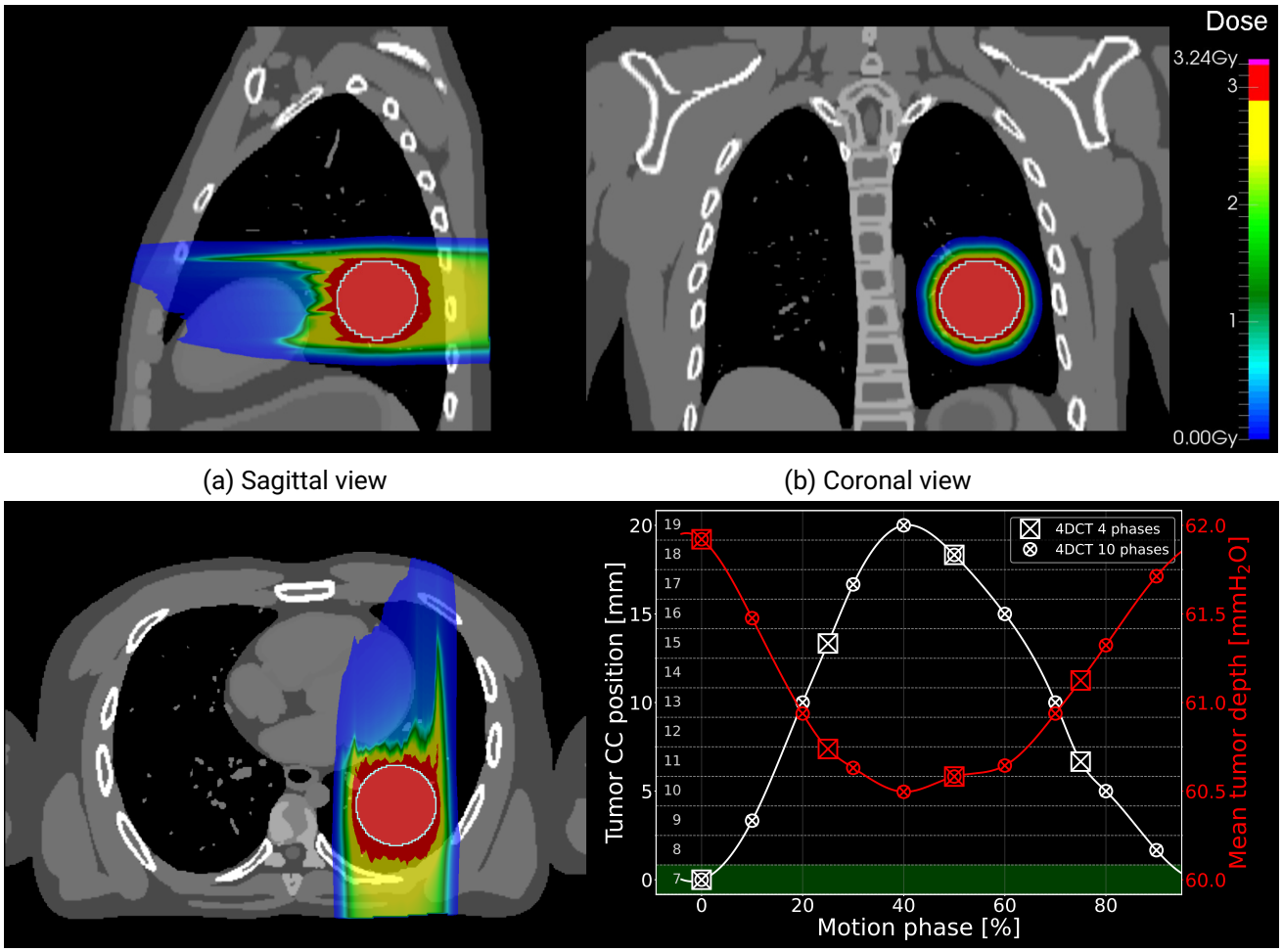

(a) Sagittal view (b) Coronal view

(c) Axial view (d) Planned tumor motion

Figure 5.1: (a)-(c): Virtual XCAT-CT with the static treatment plan to illustrate the definition of the irradiation field. The bright contour marks the spherical tumor GTV. (d): Tumor trajectory in CC direction and water equivalent depth averaged over all tumor voxels for the planned tumor motion. The horizontal lines mark the borders between corresponding XCAT CT states. The reference state 7 is highlighted in green. Squares and circle mark the state CTs selected for the four and ten phase subsets used as planning 4DCTs.

therefore be considered a realistic representation of the inhomogeneities present in real patients. The PTV was defined by adding isotropic margins of 3 mm to the GTV. Those small safety margins were selected as no clinical uncertainties like imaging artifacts, anatomical changes between CT imaging and treatment, patient mispositioning and in the conversion from HU of the CT image to relative stopping power were considered in this study. A single, dorsal treatment field was chosen. In beam's-eye-view, the lateral tumor motion is purely horizontal with the heart positioned behind the tumor. Treatment planning was done using the research software TRiP98 [22, 23, 34, 107, 108, 109]. To facilitate experimental validation, the plans were optimized to a homogeneous absorbed target dose of 3 Gy without consideration of RBE. As the focus of this work is on the technical abilities of dose delivery, this simplification is considered to be tolerable.

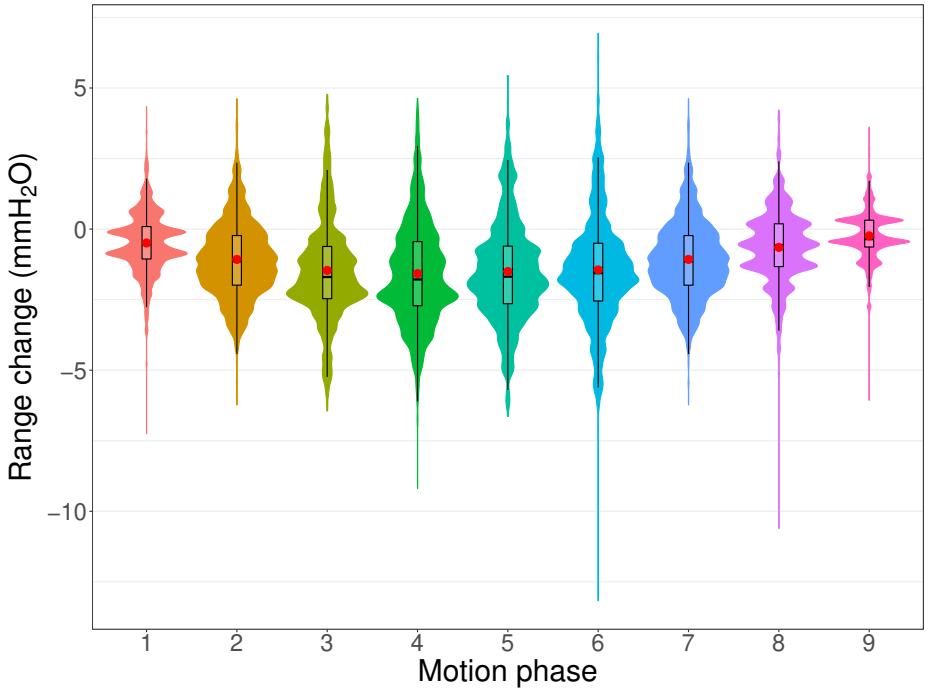

Figure 5.2: Motion induced water-equivalent range changes of all GTV voxels in the reference state after transformation to the other motion states of the 10 phase 4DCT.

5.2.2 Static deliveries

A single plan was created on the reference state CT and also delivered without motion. It therefore serves as reference for the achievable treatment quality. The treatment plan is depicted in figures 5.1a to 5.1c.

5.2.3 ITV rescanning and interplay

An ITV plan was created by simultaneous 4D optimization of the PTV dose in each motion phase in the ten state 4DCT [33]. The unmodified plan was used for interplay assessment, otherwise ten times scaled slice-by-slice rescanning was applied. The planned 4D dose distribution was calculated assuming the idealized timing of one rescan per motion phase and is depicted in figures 5.3a and 5.3b.

5.2.4 Beam tracking

For lateral beam tracking, this work uses a new definition of the target region that is proposed to guarantee target coverage for the motion expected from the periodic planning 4DCT. In the following, it is denoted as trackingITV. It was constructed in four steps:

1. For each motion state in the periodic ten state planning 4DCT, all voxels in the GTV are first translated transversal to the beam direction such that their COM coincides with the one from the reference state in the lateral projection.

2. Each voxel is shifted in longitudinal beam direction such that its water equivalent depth in the reference CT is the same as it was in the original position in the state CT.

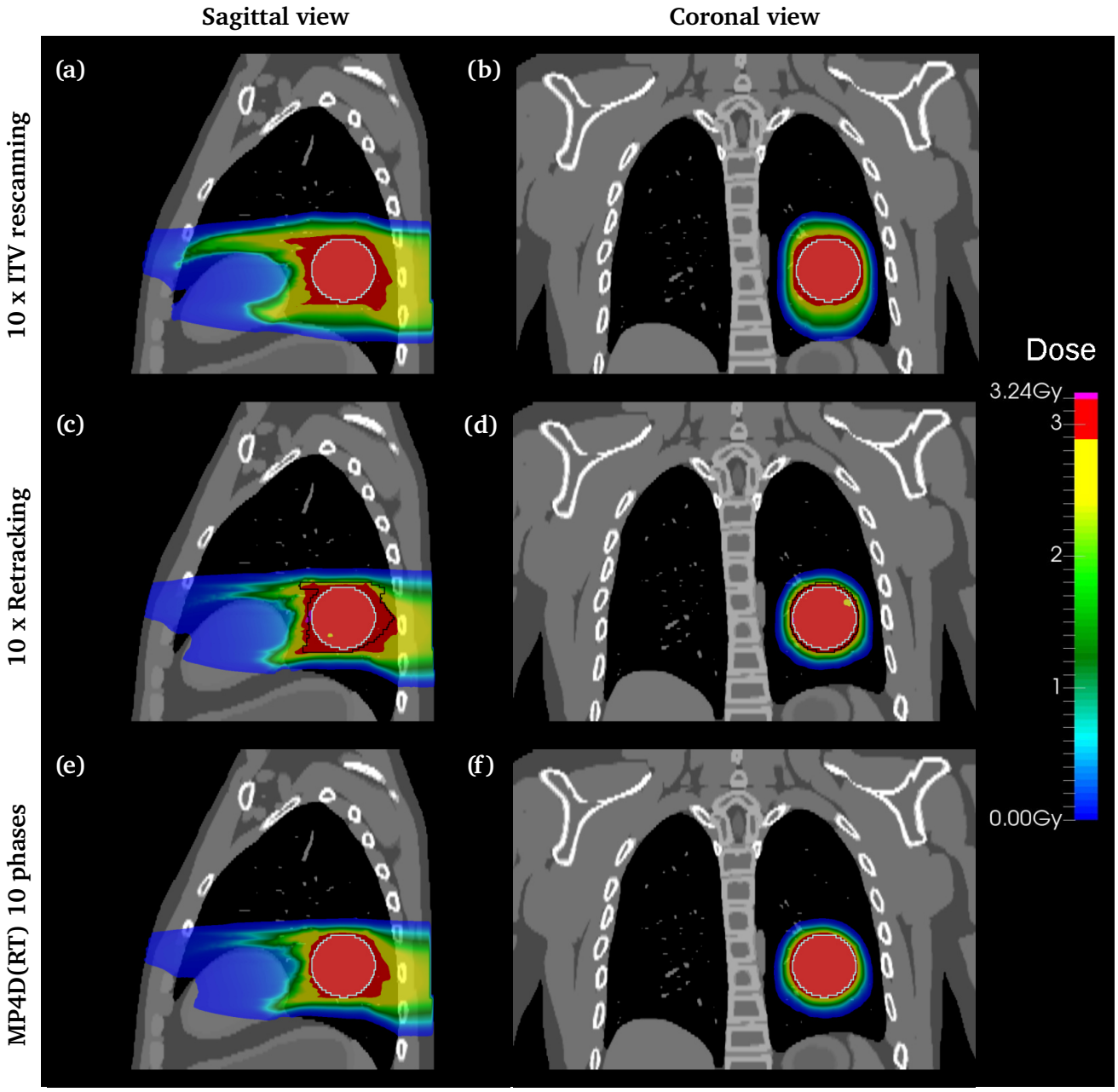

Figure 5.3: Planned 4D dose distributions (a) and (b) for ITV rescanning, (c) and (d) 10x lateral beam retracking, and (e) and (f) MP4D with and without residual tracking. The light contour marks the GTV, the black contour in (c) and (d) is the trackingITV.

3. The union of all transformed state GTVs is formed.

4. An isotropic safety margin of 3 mm is added.

Consequently, the extension of the trackingITV in longitudinal direction is similar to a range ITV[32], but the lateral extent is reduced significantly. The treatment plan was optimized for this target volume on the reference CT for a single scan as well as four and ten layered rescans with adapted minimal spot weights. The planned 4D dose distribution was calculated assuming the idealized case of one rescan per phase of

the ten states 4DCT. The 4D dose for the plan designed for ten times retracking is depicted in figures 5.3c and 5.3d. Due to range changes between motion phases, the 4D dose distribution is not conformal to the trackingITV, but target coverage of the GTV is maintained, as expected from an ITV.

5.2.5 MP4D and MP4DRT

A separate treatment plan was created for each of the motion states for the periodic planning 4DCT with $N = 4, 10$ phases. The uniform target dose for each phase plan was set to $3\,\mathrm{Gy}/N$. The state PTV was defined as the target volume. The same treatment plans were used for MP4D and MP4DRT. The planned 4D dose distributions were calculated on the 4DCT they were optimized on. The 4D dose distribution for the plan with ten phases is displayed in figures 5.3e and 5.3f.

5.3 Experimental setup and procedure

5.3.1 Experimental setup

The treatment plans were delivered in a QA-like setup at CNAO illustrated in figure 5.4. An ionization chamber array detector (PTW Octavius 1500XDR; PTW, Freiburg, Germany) was mounted on a programmable linear stage (PI M-414.2PD, controller PI C-884.4DC; Physik Instrumente, Karlsruhe, Germany). The IC

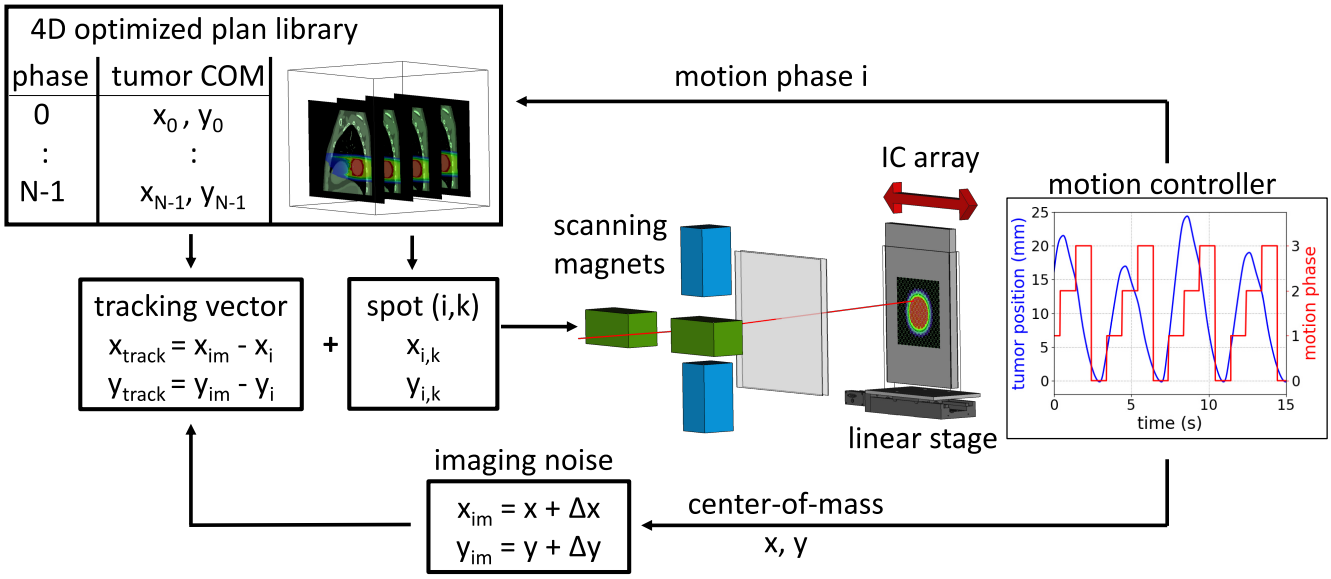

Figure 5.4: Schematic of the implementation of MP4DRT and the experimental setup used for the experiments. The value Δx and Δy of the noise was updated every 250 ms.

array detector was placed behind PMMA plates such that the active plane was at 44 $\mathrm{mmH_2O}$ in order to maximize the number of ICs receiving dose. The placement of the detector is illustrated in figure 5.5. The stage controller served as idealized motion monitoring system (encoder resolution 0.5 µm) and streamed the axis position and motion phase directly to the Motion FPGA at a frequency of 1 kHz.

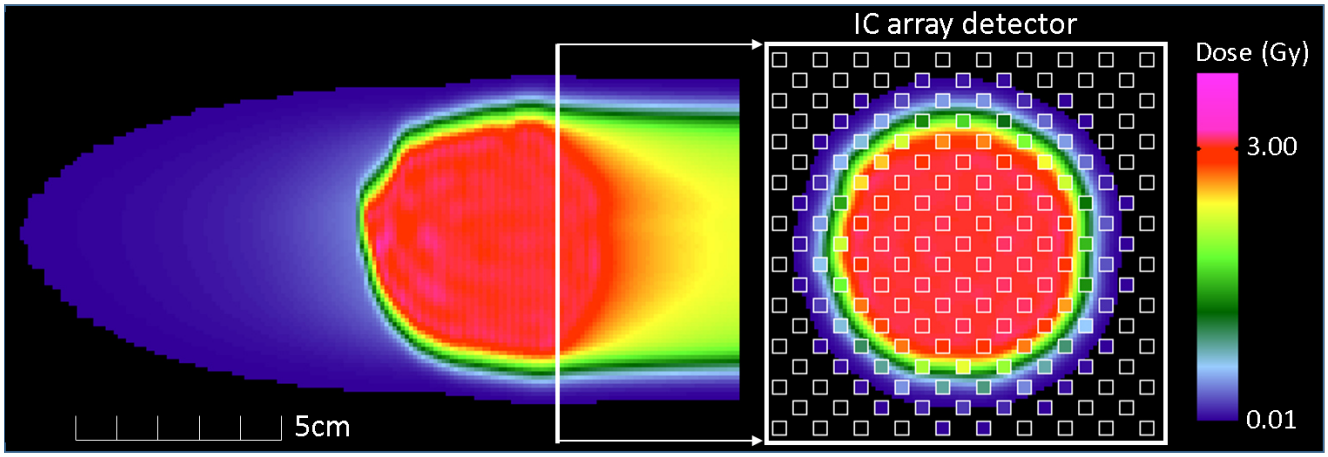

Figure 5.5: Left: Longitudinal central plane through planned dose distribution for a static delivery calculated in water. The vertical line represents the water equivalent placement of the active IC detector plane. Right: Transversal detector plane. The white squares in hte foreground represent ionization chambers and their filling corresponds to measured doses for a static delivery. The planned dose distribution is displayed in the background.

5.3.2 Motion scenarios

The linear stage was programmed to perform motions selected from three scenarios:

Regular: Periodic motion, identical to the one considered during treatment planning. The motion amplitude was set to 20.45 mm and the motion period was set to 3.9 s. The motion trace was chosen such that the time averaged position for all ten states with equal length was identical to the CC displacement of the tumor in the corresponding phase of the periodic planning 4DCT with ten phases.

Irregular: The motion amplitude was scaled to uniformly distributed random values in a range of ±25 % and the period in a range of ±10 % around the values from the regular motion. Identical irregular motion patterns were used for subsequent measurements with different motion mitigation techniques. Several sets of measurements with different irregular motion patterns were conducted.

Drift: A linear baseline drift with a velocity of 0.02 mm/s in cranial direction was added to the irregular motion scenario. The drift velocity was selected to result in a 6 mm drift after five minutes, which represents a realistic patient scenario [38, 39].

Examples for the three motion scenarios are displayed in figure 5.6.

5.3.3 Measurement of required motion monitoring precision

To measure the required precision of the motion monitoring system used in conjunction with the DDS, temporally correlated motion tracking errors were added to the motion signal with the same implementation as described in section 4.5.3. Measurements with position root mean square errors between 0 mm and 4 mm were performed for MP4DRT and tracking deliveries. According to equation (4.4), this corresponds to mean absolute tracking errors TE ranging from 0 mm to 5 mm. New tracking errors were generated

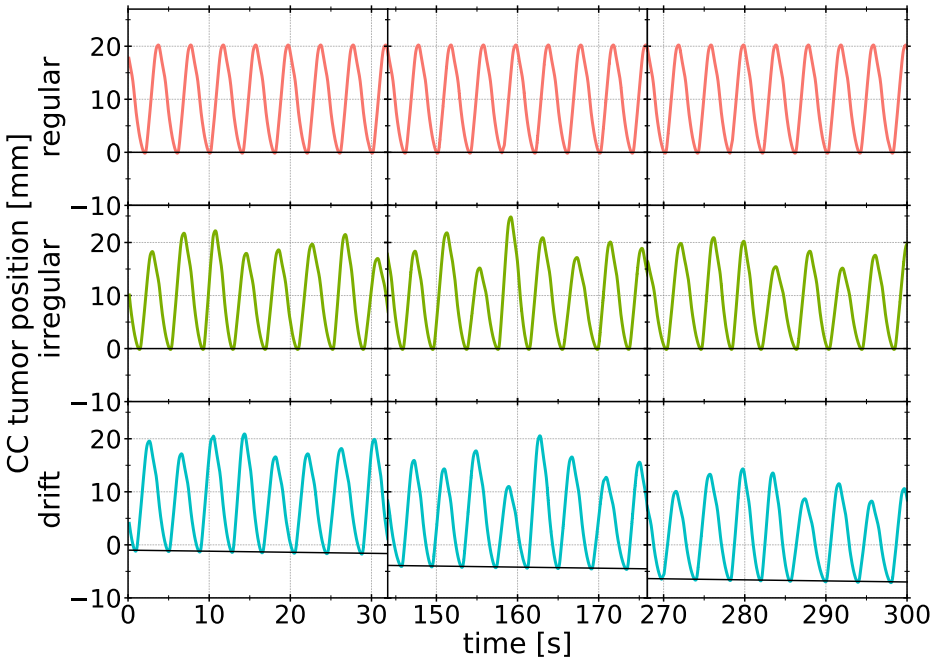

Figure 5.6: Examples for the three investigated motion scenarios.

once every 250 ms. Measurements with the motion phase and trace delayed by 100 ms and 200 ms were performed for MP4D, MP4DRT, and beam tracking in order to evaluate the effect of latency. Both, the manipulated motion information processed by the Memo FPGA, and the ground truth transmitted by the stage controller were logged by the Motion FPGA in the MMD file. The ground truth was used for the data analysis by post-hoc dose reconstruction.

5.4 Data analysis

Given the experimental setup, two data sets were available for analysis: The IC array detector data and log-files of the DDS. Both sources were analyzed separately and combined for crosschecks. The analysis contains four steps:

1. The treatment time for the different motion mitigation techniques was deduced from the log-files.
2. Dose homogeneity and agreement to the planned 4D-dose distribution was analyzed on the detector data.
3. Log-file based 4D dose reconstructions were verified on the experimental geometry by comparison to the measurements.
4. Log-file based 4D dose reconstructions on the patient anatomy are performed and evaluated dosimetrically.

5.4.1 Treatment time

The treatment time for the deliveries is determined based on the log-files. As beginning of treatment, the point in time when the DDS enters the treatment mode was defined. Treatment end was defined as the

delivery of the last raster spot. Mean and standard deviation were calculated.

5.4.2 Analysis of detector data

For each delivery mode, the expected dose distribution on the ionization chamber array detector assuming perfect motion mitigation was calculated in water. Those dose distributions in the water equivalent plane of the IC array detector were compared to the measurement using a generalized Gamma(3 mm/3 %) analysis (dose threshold 5 %, absolute dose criterion 0.08 Gy) [112, 141]. All ICs receiving dose were considered. For the measurement of the delivered dose homogeneity, a circular region of interest with a diameter of 45 mm was defined in the center of the IC array detector. It was chosen such that the same 31 ionization chambers on the moving IC array are completely inside the target region transferred to water for all planned motion phases. Therefore, the gradients at the edges of the target region were excluded from the analysis. As a metric for the dose inhomogeneity, the standard deviation of the measured IC doses normalized by their mean was used.

5.4.3 Verification of 4D dose reconstructions in experimental geometry

For each delivery, log-file based 4D dose reconstructions were performed in water. For this purpose, the delivered raster points were assigned to the 25 motion states from the virtual XCAT 4DCT based on motion amplitude. If the strip detector measured enough particles to measure the beam position, this value was used. In the few other cases, the beam position was calculated from the magnet currents. To account for intra-state motion, beam spots are shifted in lateral direction by the difference between the actual position of the linear stage and the COM target position for this motion state. Calculated dose distributions were compared to the measurement on the IC array detector in the corresponding water equivalent plane. Dose reconstructions for which more than 90 % of all irradiated ionization chambers pass a generalized Gamma(3 mm/3 %) criterion [112] were considered valid.

5.4.4 Evaluation of 4D dose reconstructions on patient CT

For valid dose reconstructions, the dose distribution was reconstructed with the same input files on the 25 states XCAT CT. Treatment quality was quantified by four dose-volume histogram (DVH) metrics:

1. Target coverage (D95)
2. Dose conformity (conformity number CN, [142])
3. Dose homogeneity (D5-D95)
4. Dose to organs at risk (heart and left lung V20).

Here, D5 and D95 denote the dose that was exceeded in 5 % and 95 % of the GTV, respectively. Values are given in percent of the target dose. For D95, a value of 95 % is the requirement for clinical acceptance. A small value of D5-D95 corresponds to a homogeneous dose and therefore good mitigation of the interplay effect. V20 denotes the fraction of the volume of an organ, that receives more than 20 % of the target dose. This value should be as low as possible. The conformity number [142] is defined as

$$CN[\%] = \frac{V_{95,target}}{V_{target}} \cdot \frac{V_{95,target}}{V_{95,total}} \cdot 100 \tag{5.1}$$

with the target volume V_{target}. $V_{95,target}$ and $V_{95,total}$ denote the volume absorbing more than 95 % of the target dose inside the target volume and in the entire body. The closer the conformity number to 100 %, the more restricted is the high dose region to the target volume.

5.4.5 Tumor rotations

In real patient cases, tumor motion does not only comprise a pure translation, but also rotation and deformation. Especially lung tumors attached to the chest wall cannot translate with the adjacent lung tissue and are consequently rotated [143]. Tumor rotations are in general difficult to detect which can cause errors in the DIR. This affects the outcome of dose calculations. In addition, it was shown that tumor rotations and deformations challenge beam tracking, especially for big tumors, as the relative motion of different portions of the tumor cause inverse interplay inside the tumor [76, 144]. In this study, only the tumor COM motion was tracked. It is equal to the motion of all single tumor voxels in the case of pure translation, but this is not the case in the presence of an additional tumor rotation. It is therefore expected that an additional rotation will reduce target coverage. For MP4D and MP4DRT, this effect is mitigated due to the intrinsic breath-sampled rescanning that distributes the dose evenly over all motion phases while preserving the 3D raster grid. In order to investigate this, additional tumor rotation was added to the deformable vector fields used for the dose reconstruction. For this purpose, an updated version of the XCAT software [9] was used. The rotation axis was chosen perpendicular to the tumor translation and beam direction, thus introducing range changes for specific tumor voxels over the course of a breathing cycle. The rotation angle was fixed to be proportional to the tumor translation. The rotation corresponding to the nominal translation amplitude of 20 mm was set to values between 0° and 30°. Because of the spherical shape of the tumor, the rotation does not have any impact on the treatment planning. For deliveries with the irregular motion scenario and without additional imaging errors, the doses were reconstructed with the modified vector fields. The effect of the rotation amplitude on the target coverage (D95) was assessed.

5.5 Results

5.5.1 Treatment time

In total, 82 irradiations were delivered to the IC array detector. They are listed in table 5.1 classified by delivery mode and number of phases (MP4D and MP4DRT) or rescans (Static, ITV, Tracking). The measured duration of the delivery starts when the dose delivery system enters into the treatment state and stops with the last point being irradiated. Hence, it does not contain preprocessing of the treatment plan, safety checks and postprocessing of the log-file data.

Table 5.1: Number of deliveries per mode and the mean (standard deviation) duration of the irradiation.

Delivery mode	Static	ITV		Tracking			MP4D		MP4DRT	
Phases/Rescans	1	1	10	1	4	10	4	10	4	10
#Measurements	2	5	5	5	12	13	4	10	10	16
Duration (s)	115	181	262	131	127	124	255	343	246	324
(stddev)	(4)	(21)	(15)	(8)	(8)	(5)	(29)	(47)	(24)	(30)

5.5.2 Evaluation of detector data

In figure 5.7, the results of a Gamma(3 mm/3 %) analysis comparing measured and planned dose distributions on the IC array detector are shown for all measurements with ideal motion information.

For ITV interplay and rescanning deliveries, the interplay causes severe dose degradation compared to the planned dose. The rescanning was not able to compensate for the drift that was greater than the 3 mm

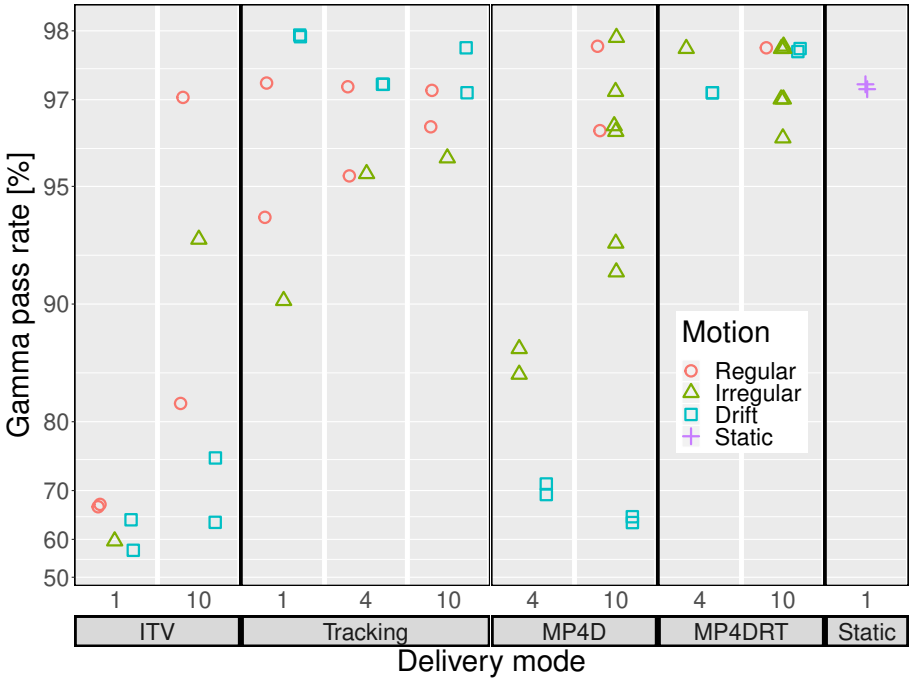

Figure 5.7: Gamma($3\,\%/3\,\mathrm{mm}$) comparison of planned dose distributions with measurements on the IC array detector for all deliveries with perfect motion information. The y scale is logarithmic in the difference to $100\,\%$.

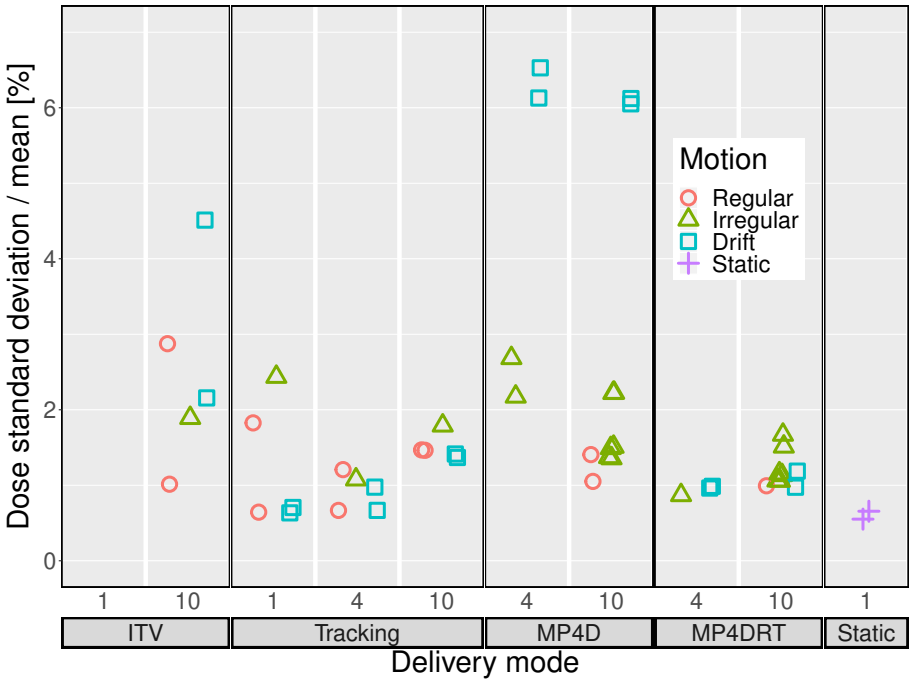

Figure 5.8: Measured dose inhomogeneity in the ROI for the tested delivery techniques. Interplay deliveries were omitted for better visibility.

distance criterion. In addition, the big discrepancy between the two ITV deliveries with regular motion shows that interplay without active control of the temporal correlation between delivery progress and motion phase is a severe challenge to quality assurance. The high pass rate for tracking is expected as the detector only performs a lateral translation without range changes or deformation. This is the ideal case for tracking. Tracking performs well for all motion scenarios as it also reacts to unexpected motion. Retracking clearly reduced the spread of the measurements with little difference between four and ten retracks. The performance for MP4D with ten phases is similar to retracking in absence of a drift, but shows a substantial spread for measurements with different irregular motion traces. Residual motion in MP4D deliveries with four phases, however, causes severe dose degradation. In the baseline drift scenarios, MP4D fails to reproduce planned dose distributions. With MP4DRT, agreement between measurement and treatment planning $>96\,\%$ could be restored for all motion scenarios and is on par with static deliveries. The standard deviation of the measured IC doses in the ROI normalized by their mean is depicted in figure 5.8. For the MP4D and ITV deliveries with baseline drift, the dose homogeneity is reduced due to the target miss. For a periodic motion, tracking, MP4D and MP4DRT with ten phases were able to deliver dose distributions of similar homogeneity. For the irregular motion scenario, however, MP4D, especially with four motion phases, delivered less homogeneous doses. For MP4DRT, no significant difference is found between four and ten motion phases and all three motion scenarios. As the improvement of MP4DRT over MP4D is more pronounced for four motion phases than for ten, it can be concluded that the residual tracking could significantly reduce the interplay caused by intra-phase motion in MP4D.

5.5.3 Verification of 4D dose reconstructions

The $\Gamma(3\,\%/3\,\mathrm{mm})$ pass rate between measured and reconstructed dose for all measurements is shown in figure 5.9. The mean pass rate was 97.5 % with a standard deviation of 1.4 %. The minimal pass rate was 90.8 %. Consequently, all measurements are considered valid and are included in the following analysis.

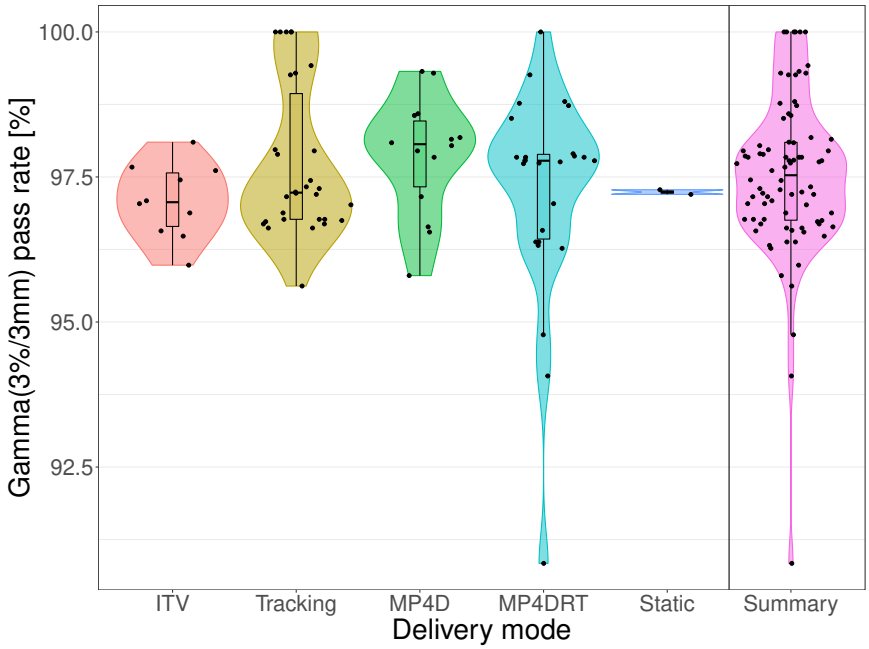

Figure 5.9: Gamma($3\,\%/3\,\mathrm{mm}$) pass rate between measured and reconstructed dose distributions. The summary violin on the right shows the merged distributions of all delivery techniques.

5.5.4 Evaluation of dose reconstructions on patient CT

The 4D dose distributions for all deliveries were calculated on the XCAT 4DCT. Reconstructed dose distributions are compared for MP4D and MP4DRT in figure 5.10 and for ITV and beam tracking in figure 5.11. The quantitative analysis of the DVHs follows in figure 5.12.

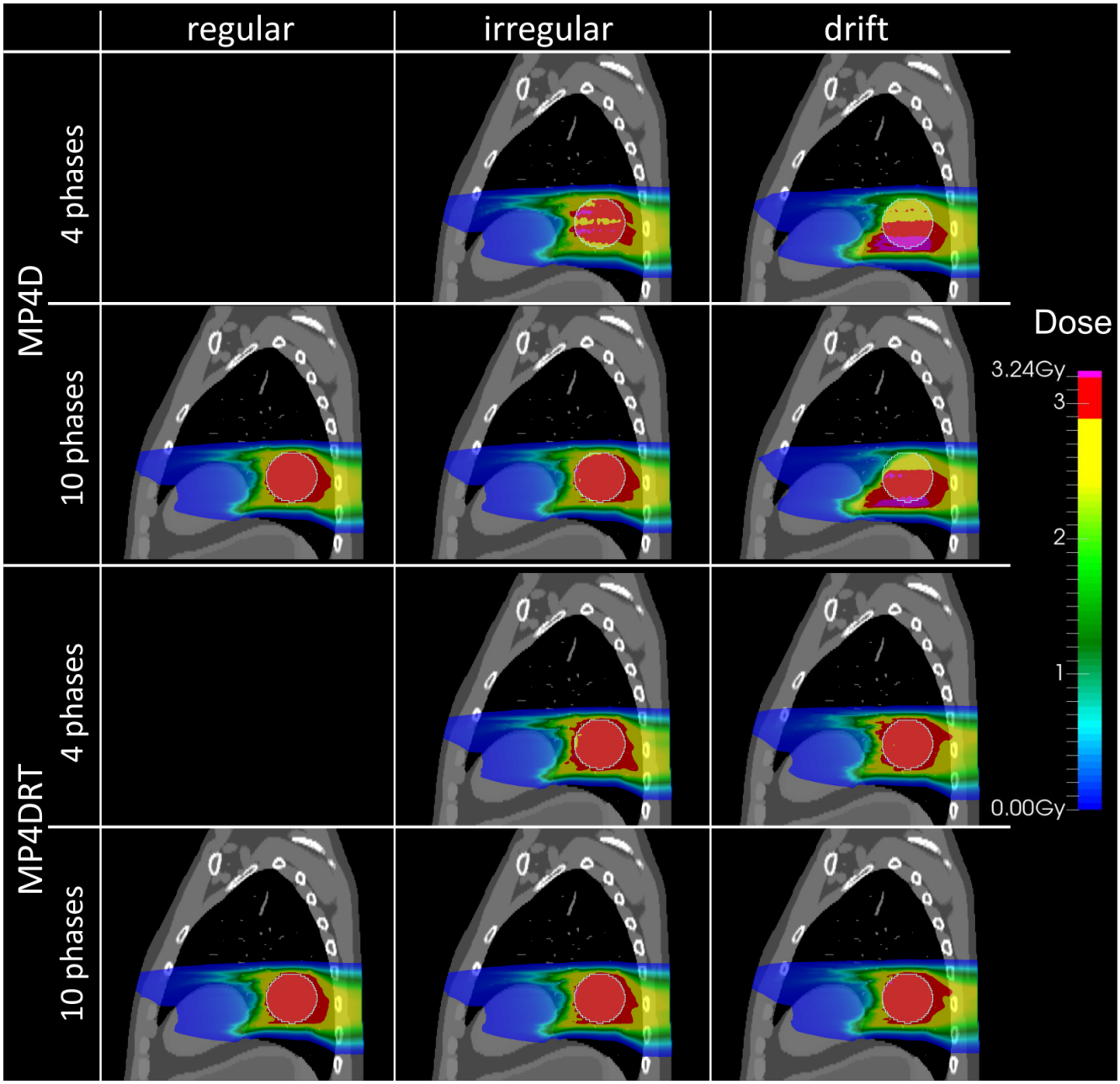

Figure 5.10: Reconstructed dose distributions for MP4D and MP4DRT deliveries. The cuts show the central sagittal plane of the tumor.

Interplay deliveries resulted in highly inhomogeneous dose distributions. As already seen on the detector in figures 5.7 and 5.8, rescanning can improve the dose distribution, but a partial target miss is observed as the baseline drift exceeds the safety margins. Consequently, the beam missed the tumor when it was in the

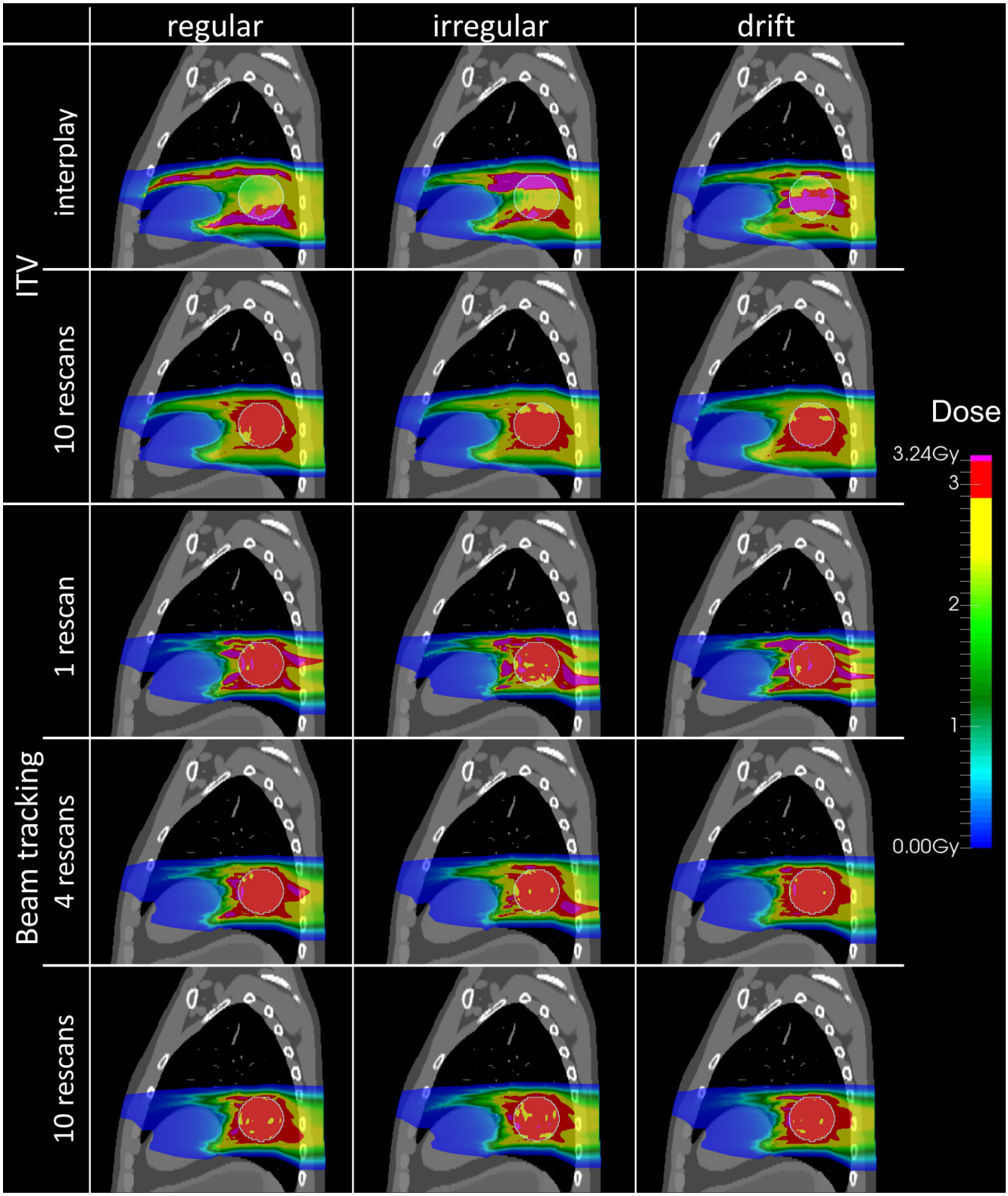

Figure 5.11: Reconstructed dose distributions for interplay, ITV rescanning and beam tracking deliveries. The cuts show the central sagittal plane of the tumor.

end-exhale state. The overshoot at both edges in the motion lead to a high dose to the surrounding lung and the heart behind the tumor for all motion scenarios. Beam tracking leads to a significant reduction of the irradiated volume and compensates for the drift. However, the range changes during the motion cause cold spots inside the target volume. For a single scan over the tumor, severe inverse interplay leads to high dose regions outside the tumor. The dose homogeneity inside and outside the tumor is clearly improved by applying rescanning. No further improvement was achieved when switching from four to ten rescans. MP4D with ten motion phases was able to deliver highly conformal and homogeneous doses for the periodic and irregular motion scenario. A clear advantage over deliveries with only four motion states was observed for the irregular motion case. For the drift scenario, however, the tumor was missed in all motion states when the high energies are delivered. Consequently there was a large loss in target coverage. By applying residual tracking, high dose conformality and homogeneity could be restored. There was little difference between MP4DRT deliveries with four and ten motion phases.
For all measurements without introduced imaging errors, the reconstructed target coverage, dose homogeneity, conformity number and organ at risk dose are displayed together with the corresponding values from the treatment planning in figure 5.12.
As expected, interplay deliveries performed worst in all scenarios and metrics. ITV rescanning was able to recover target coverage to D95 > 90 % for all deliveries except one scenario with drift. However, D95 > 95 % could not be guaranteed and the V20 in the organs at risk is on par with uncompensated interplay deliveries.
Beam tracking guarantees target coverage for all scenarios, due to the longitudinal safety margins introduced by the construction of the trackingITV. This comes with the expense of a high dose region outside the tumor of similar size than for ITV rescanning and therefore similar conformity numbers. However, the volume with medium and low dose lateral to the tumor is greatly reduced which leads to improved organ at risk sparing. Especially the heart located behind the tumor is efficiently protected.
MP4D was shown to deliver highly conformal and homogeneous dose distributions that allow efficient OAR sparing in the cases of periodic and irregular motion with stable baseline. Target coverage was significantly better for deliveries with ten phases instead of only four phases, demonstrating the adverse effect of larger residual intra-phase motion and fewer rescans. The target coverage was clearly higher for periodic motion than for lateral beam tracking and similar to it in the irregular motion scenario. However, in the motion scenario with baseline drift, the performance of MP4D is greatly affected. As the drift was bigger than the used safety margin of 3 mm, it caused target miss in all motion phases. Thus, target coverage was insufficient, the dose gradients inside the tumor led to a high D5-D95 and the heart was hit by the beam.
MP4DRT performed best among all motion mitigation techniques considered in this study with results closest to the ones for static deliveries. A target coverage of D95 > 95 % was achieved for all motion scenarios. Deliveries with four motion phases performed similar to deliveries with ten phases even though they were slightly less conformal. MP4DRT also allowed for efficient organ at risk sparing similar to a static delivery. The quality of MP4DRT deliveries was highly reproducible which will allow for reliable QA protocols in clinical practice.
All observations were in agreement with the detector measurements described in the previous section.

5.5.5 Tumor rotations

The 4D dose reconstructions of deliveries with four and ten times retracking and for MP4DRT with ten phases with tumor rotation angles between 0° and 30° are depicted in figure 5.13. It is apparent that the inhomogeneity of the retracking deliveries increases with the rotation amplitude. The dose degradation is more severe in the delivery with four rescans than in the one with ten rescans. In contrast, the effects of the rotation on the MP4DRT delivery are marginal. This finding is confirmed by the quantitative analysis.

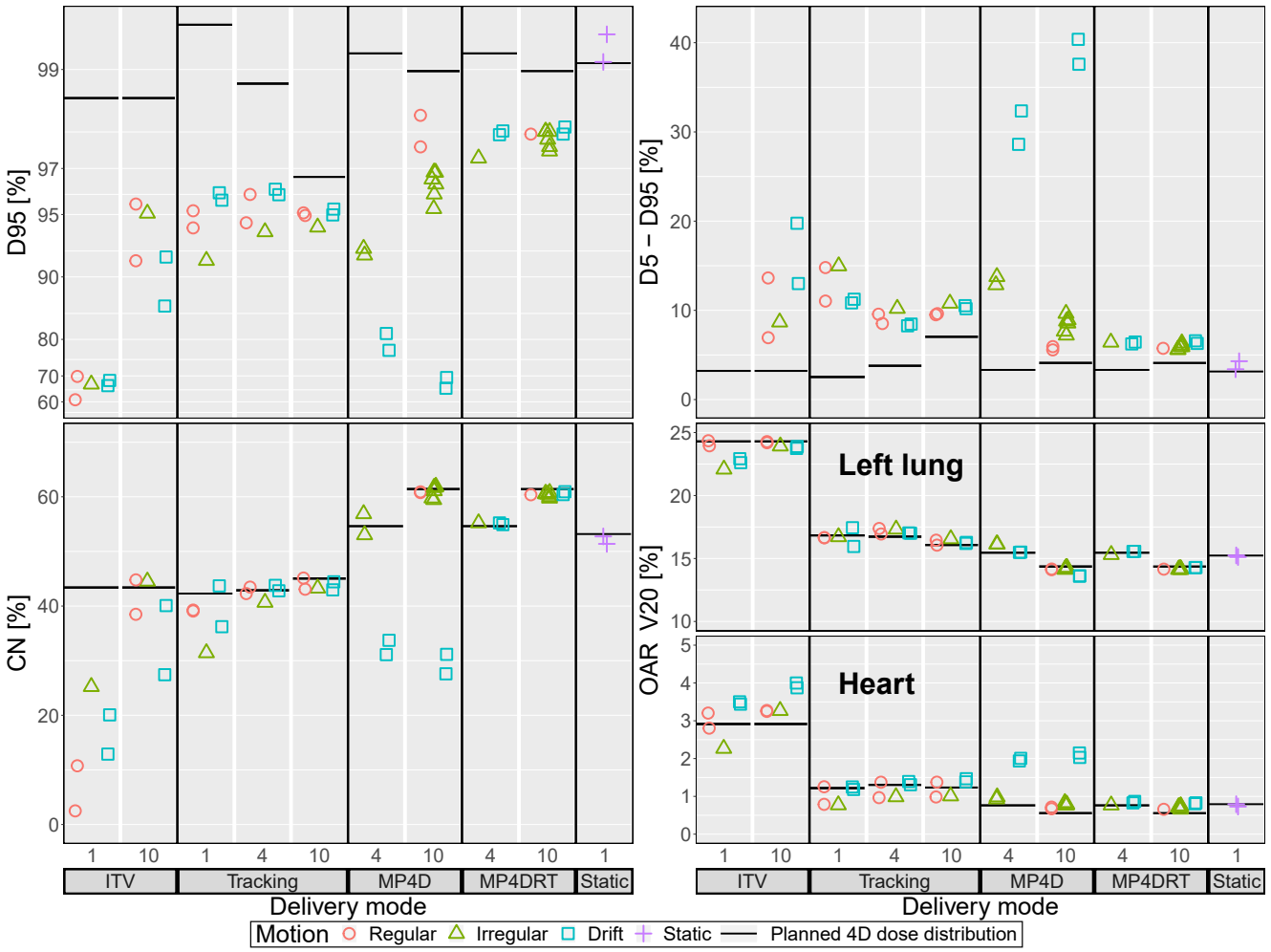

Figure 5.12: DVH metrics for reconstructed deliveries with perfect motion information. Each marker represents a measurement. Horizontal lines are the planned dose distributions and are identical for MP4D and MP4DRT. Top left: Target coverage (D95): For this plot, the y scale is logarithmic in the difference from 100 %. Top right: Dose homogeneity (D5-D95). Interplay was omitted for better visibility. All ITV interplay deliveries had a D5-D95 between 51 % and 101 %. Bottom left: Dose conformity (CN). Bottom right: Organ at risk V20 for the left lung (upper half) and the heart (lower half).

The dependence of the target coverage on the tumor rotation amplitude is depicted for all delivery modes in figure 5.14.
For beam tracking, the expected reduction of target coverage was observed. For one and four rescans, target coverage is substantially reduced already for rotation amplitudes of 10°. An increase of the number of rescans to ten reduces this dependence, but did not eliminate it completely. For MP4D, target coverage was independent of tumor rotation amplitude. This also shows that the MP4D target coverage is largely independent of underlying DIR errors - the rotation was introduced after treatment planning, completely changing the vector fields used in dose calculation. For MP4DRT, only a small decrease in target coverage with increasing rotation amplitude is observed, but it remains the technique with the highest target D95 for rotations up to 30°.

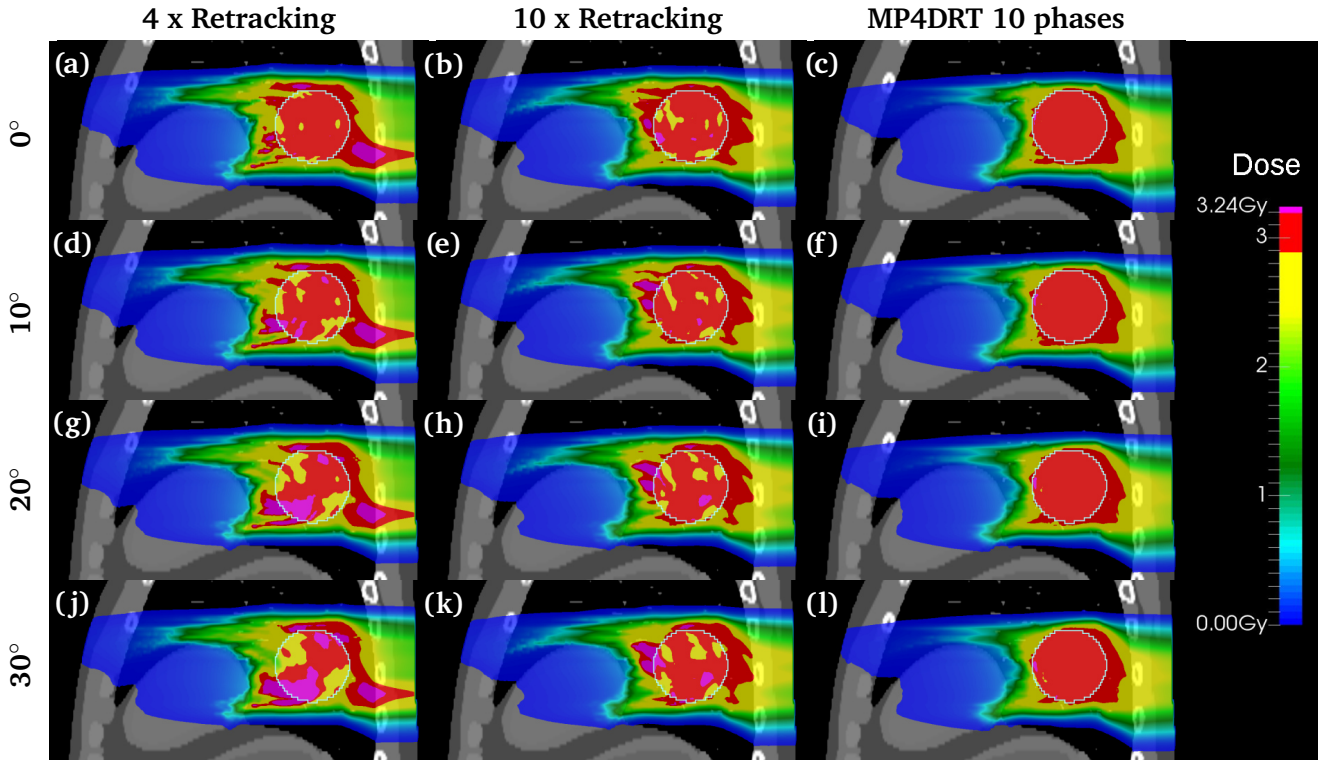

Figure 5.13: Reconstructed 4D dose distributions for deliveries with four and ten times retracking and for an MP4DRT delivery with ten phases. For the same delivery, vector fields including tumor rotation amplitudes between 0° to 30° were used for the dose calculation. The bright contour labels the spherical GTV.

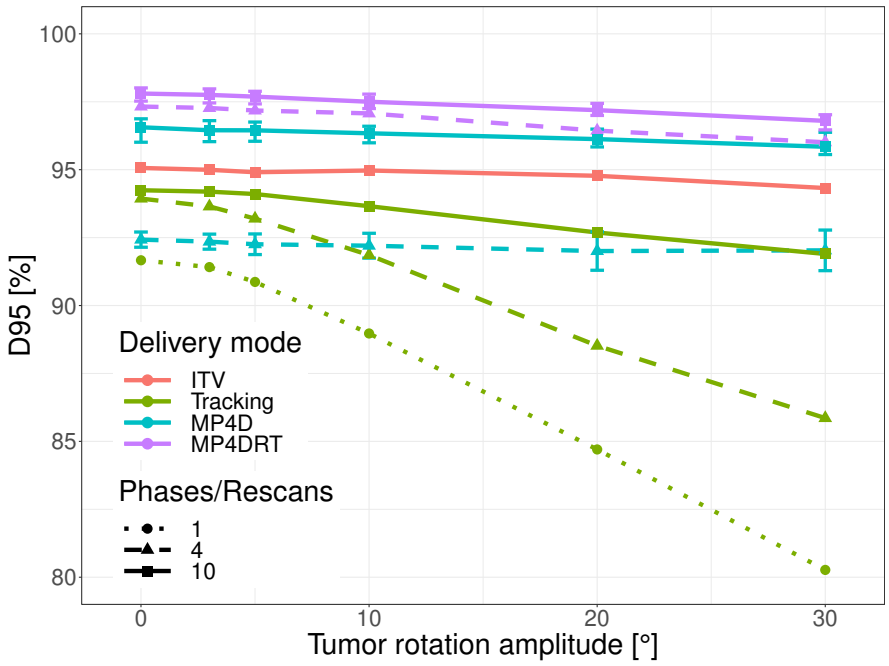

Figure 5.14: Dependence of the reconstructed D95 on the additional tumor rotation amplitude. Error bars represent minimum and maximum value for repeated deliveries.

5.5.6 Required motion monitoring precision

The deliveries with the irregular motion scenario with and without artificial noise and latency on the motion signal were evaluated in the same steps. The ground truth motion information was used as input for the 4D dose reconstructions.
On the left of figure 5.15, the results of the Gamma(3 mm/3 %) analysis comparing the planned and measured dose distribution on the IC array detector are displayed. In this measurement, MP4DRT with ten phases is the most robust online adaptive delivery mode. The relative standard deviation of the measured dose in the ROI is depicted on the right of figure 5.15. For small motion monitoring errors, the measured dose homogeneity is similar for tracking and MP4DRT as the homogeneity is mainly dominated by the intrinsic inhomogeneity of the treatment plans and the beam quality. For increasing tracking errors, the number of rescans and the time structure of the delivery becomes important. As the beam is regularly gated for MP4DRT, corresponding spots in different motion phases are delivered with different random imaging errors. Consequently, errors average out to a higher extend than for tracking, where the several rescans are made with only a single random error for slices with low particle number.

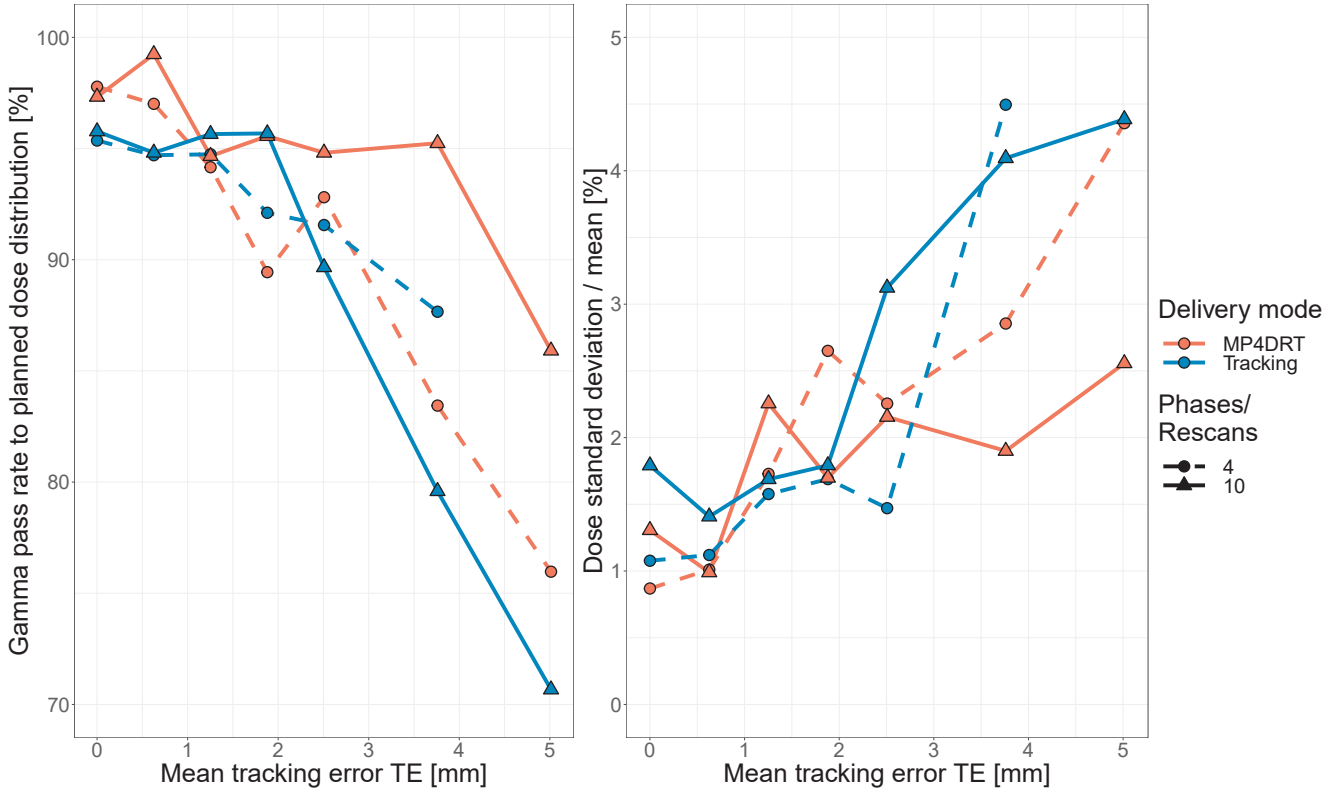

Figure 5.15: Left: Dependence of the Gamma(3 mm/3 %) pass rate between measured and planned dose distribution on the IC array detector on the precision of the motion information processed by the dose delivery system. Right: Relative standard deviation of the measured IC doses in the region of interest.

The corresponding dose volume histograms for the MP4DRT deliveries are depicted in figure 5.17. Figure 5.16 displays the dependence of the reconstructed target coverage and dose homogeneity on noise level of the imaging signal for MP4DRT and beam tracking with four and ten phases or rescans, respectively, for the irregular motion scenario. All four curves show a similar trend. MP4DRT with ten phases is the

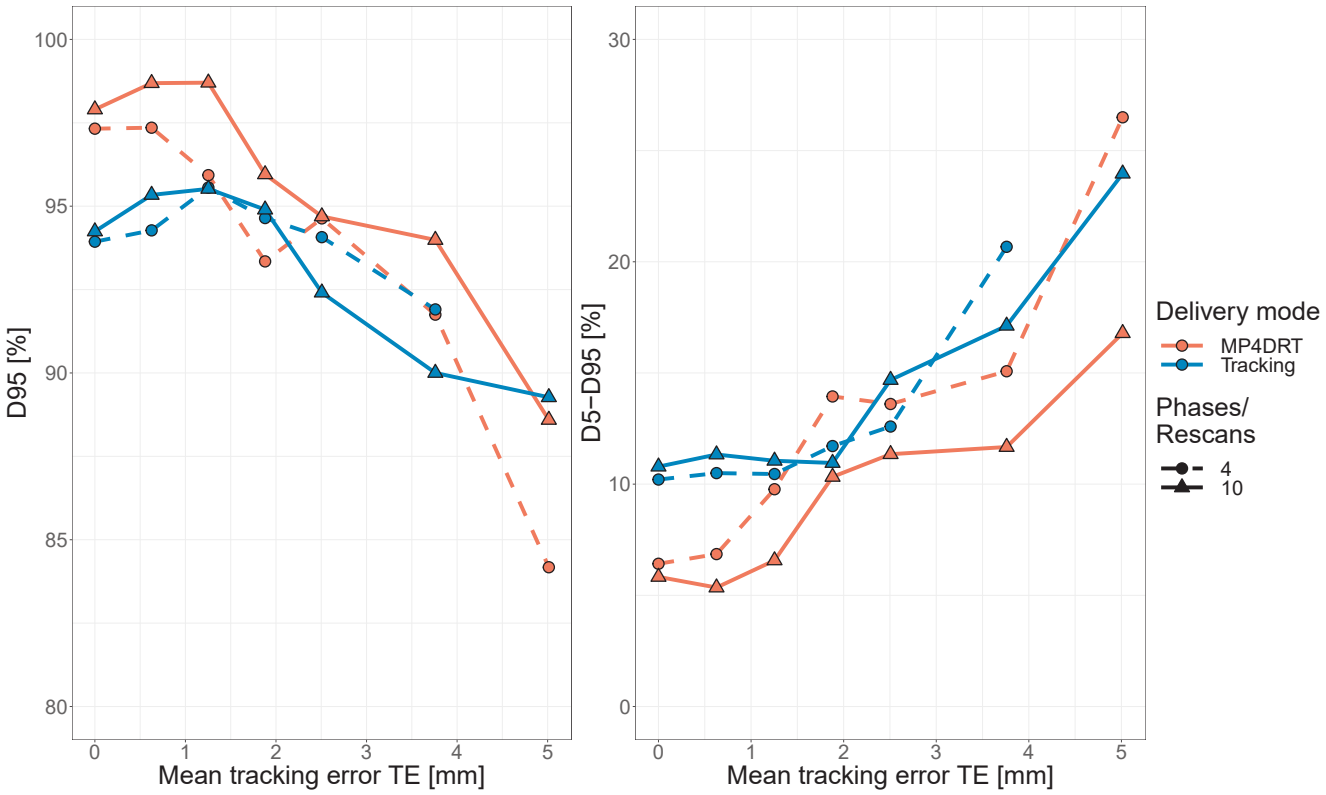

Figure 5.16: Dependence of the reconstructed target coverage (D95, left) and dose homogeneity (D5-D95, right) on the precision of the motion information processed by the dose delivery system.

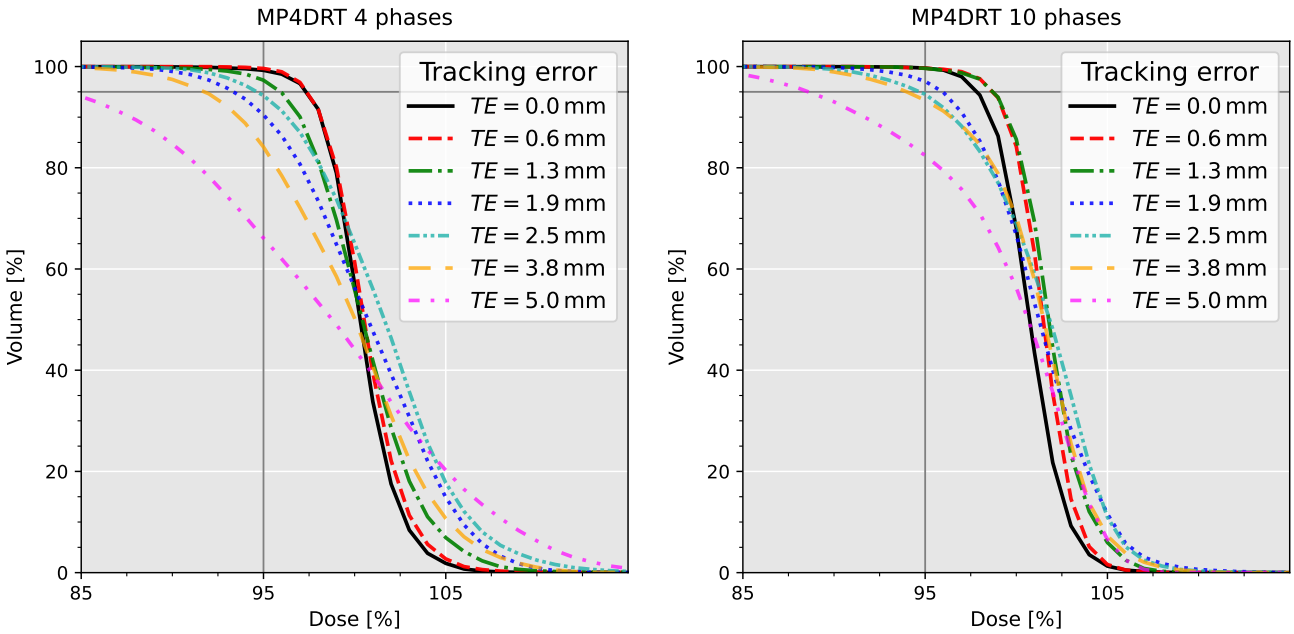

Figure 5.17: DVHs for MP4DRT deliveries depending on the noise level of the motion monitoring. Curves that are partially on the top right of the crosshair fulfill D95>95 % and V95>95 %.

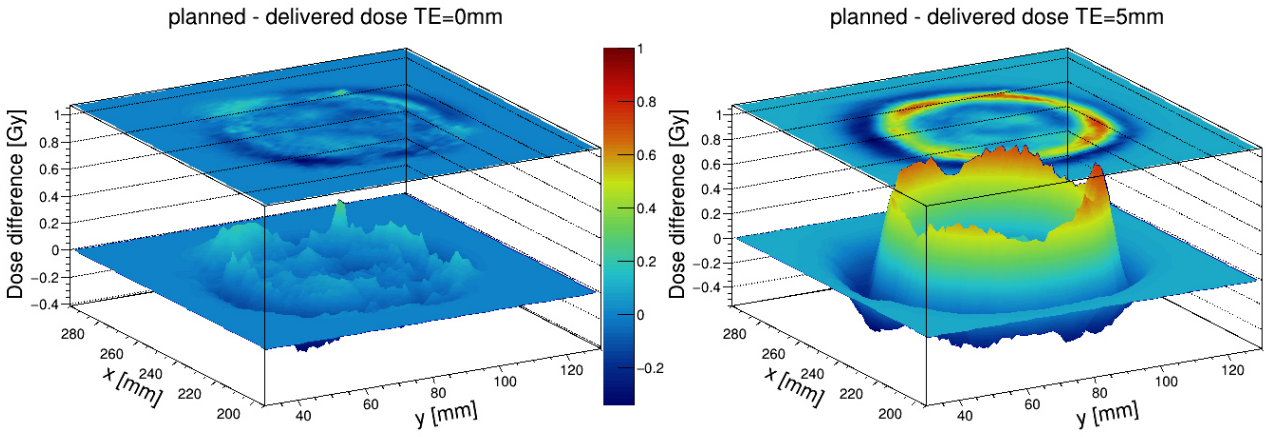

Figure 5.18: The reconstructed dose difference between planned and delivered dose for MP4DRT deliveries with 10 motion phases. The figure shows the central coronal plane of the tumor which is lateral to the beam. Left: Delivery with perfect motion signal. Right: Delivery with mean absolute tracking error of 5 mm. The color scale in the center is equalt to the z-axis and applies to both subfigures.

most robust delivery mode for target coverage and dose homogeneity. Clinically acceptable target coverage of D95 $>$ 95 % could be achieved for a mean absolute tracking error TE of up to 1.9 mm.
The dose degradations appear mainly at the edges of the target volume where the tracking errors shift pencil beams out of the target volume, but not vice versa. This is illustrated by the difference between planned and reconstructed dose distribution for MP4DRT deliveries with perfect motion information and with a mean absolute tracking error of 5 mm in figure 5.18. This suggests, that the effect of motion monitoring errors can be partly mitigated by increased safety margins.
In figure 5.19, the target coverage is shown depending on an introduced motion monitoring latency. Here,

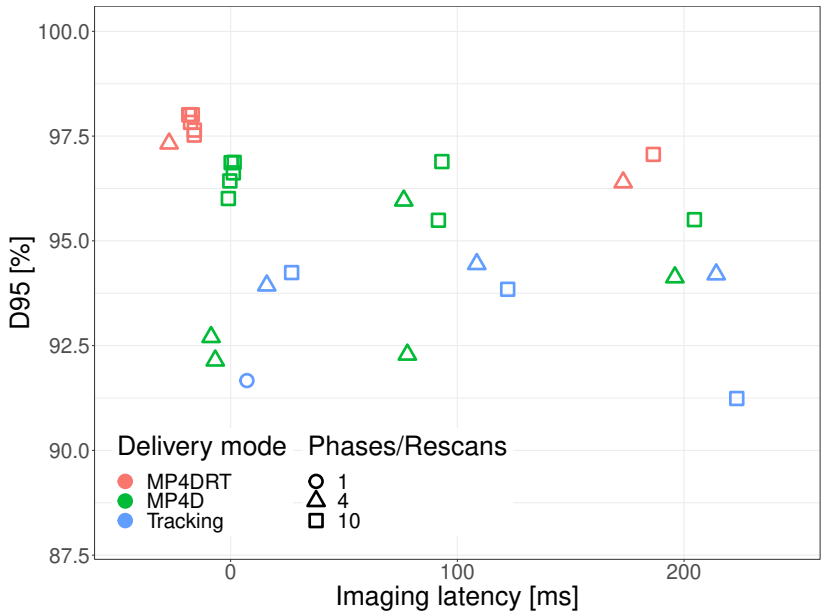

Figure 5.19: Dependence of the reconstructed D95 on the latency of the motion signal processed by the DDS.

MP4D is also included as latency of the motion signal affects the timing when the DDS switches between motion phases. Only little dependency of treatment quality on the imaging latency could be observed.

5.6 Discussion

The new motion mitigation strategy MP4DRT was experimentally validated by delivering treatment plans optimized for an inhomogeneous, anthropomorphic anatomy that were delivered to a QA-like setup. It was compared to the other motion mitigation techniques ITV rescanning, lateral beam retracking and MP4D. In this section, the performance of the tested strategies is compared. Next, the strengths and limitations of the presented study are described. Finally, the clinical prospects of the new MP4DRT technique are discussed.

5.6.1 Comparison between motion mitigation techniques

In this study, it was demonstrated that MP4DRT can deliver dose distributions superior to the compared clinically applied or proposed motion mitigation techniques, namely ITV rescanning, lateral beam tracking and MP4D.
The observed performance of the compared motion mitigation techniques is in agreement with the literature, but also highlighted the limitations of those techniques. ITV rescanning could partly restore the planned dose distributions compared to interplay. This, as well as the degradation by a baseline drift, is consistent with the simulation study described in chapter 3. The strong variability between measurements was caused by different temporal correlation of delivery and motion and demonstrates the need to account for the time structure during treatment delivery [41, 42].
MP4D with ten phases shows more reproducible results and was able to compensate for random changes of the motion amplitude thanks to its intrinsic breath-sampled rescanning. The study underlines the high potential of this technique to efficiently spare healthy tissue, which was achieved by the conformal treatment planning strategy [10, 79, 80, 124, 125]. However, the vulnerability to systematic drifts indicates the necessity for a safety mechanisms for the use in clinical practice.
Lateral beam tracking was robust against irregular motion. Target coverage was consistent amongst different numbers of rescans. The appearance of dose degradation due to range changes and inverse interplay in the deliveries reported in the literature [54] could be confirmed by the observations. Since retracking partly mitigated inverse interplay, as well as tumor rotations, as was observed in section 5.5.5, it is recommended for any future use of a beam tracking strategy. But it is also apparent that the lack of compensation of range changes limited the achievable target coverage. The discrepancy to the planned 4D dose implies that a breath-sampled rescanning method could lead to improved results.
When utilizing a tumor tracking system, the presented MP4DRT provides a more conformal alternative. As demonstrated, this new technique synergizes the robustness to irregular motion of beam tracking with the conformity of MP4D. Also the robustness of MP4D against rotations could be preserved. MP4DRT was superior to the other techniques in target coverage, dose homogeneity and conformity, OAR sparing, and reproducibility. Only MP4DRT was able to deliver a clinically acceptable target coverage of $D95 > 95\,\%$ irrespective of the motion scenario.
MP4D and MP4DRT showed an increased delivery time compared to static or tracked deliveries. This was caused by the spill length of 3 s at CNAO. As this was shorter than the motion period, more than one spill cycle was necessary to cover all motion phases for each energy. In comparable deliveries at CNAO and GSI with a spill length longer than the motion period, delivery time increased only 61 % [10] and 21 % [124] compared to static deliveries. The duty cycle for MP4D and MP4DRT increases with integral dose. For a

specific iso-energy slice, the treatment time is nearly independent of the particle number as long as each phase plan can be delivered during one visit of this motion phase. This limit is much higher than for gated deliveries, where only a subset of the respiratory cycle is available for deliveries. Since the duration of spills are somewhat tunable parameters at medical synchrotrons, future clinical implementation of MP4DRT could also investigate an optimization of these values. The trend towards the use of RFKO extraction from the accelerator enables dynamic intensity control and gating that is non-destructive to the stored beam in the synchrotron ring [68, 145]. Reducing the loss of particles during the beam gates reduces the number of acceleration cycles and consequently increases the duty cycle in MP4DRT. The maximum spill duration should be tuned to be long enough to cover typical breathing periods, which would enable to irradiate each IES in a single spill. After the IES, the spill is aborted anyways, such that a longer spill duration would not be problematic. If the spill is shorter than a breathing period, the combined duration of the spill and spill pause needs to be sufficiently different to the breathing period for efficient delivery.
Also advanced rescanning strategies would prolong treatment time. For protons, it was shown that breath-sampled layered rescanning greatly improves delivery quality at the expense of an increase in treatment time of a factor of 2-2.5 compared to conventional layered rescanning [41, 42]. A similar pattern was reported for phase-controlled layered rescanning with carbon ions, in which coverage of an entire breathing cycle by the rescanning is achieved by reducing the beam intensity [68, 138].

5.6.2 Strengths and limitations

In this study, direct detector measurements of the delivered dose were combined with log-file based dose reconstructions. Even though the measurements with the IC array detector were limited to a single water equivalent plane, the number of ICs in the treatment field was higher than for other studies using pinpoint detectors [34, 146, 147, 148]. The dose reconstructions were validated in this plane and extend the analysis to the entire 3D volume. In contrast to pure simulation studies, the reconstructions contain the real-time behavior of the DDS, including the online switching of phase plans, and the beam positions measured with the nozzle detectors. The analysis of the IC array data alone lead to results that are in good agreement with the log-file based dose reconstructions on the patient CT. On the detector, beam tracking performed better than on the patient anatomy due to the lack of range changes. The parallel analysis of data from two sources (DDS logfiles and detector data) was a useful cross-check and supports the reliability of the results.
The study was performed with an idealized motion monitoring system. This had several advantages. First, it enabled accurate dose reconstructions, resulting in the good agreement with the detector measurements and therefore trustworthy dosimetric results. Second, different noise levels could be added to the motion signal in order to determine the required tumor tracking precision. Third, the motion monitoring signal was not distorted by systematic biases that are specific to the used imaging system, motion phantom, or tumor site. Therefore, the suitability of an arbitrary system can be assessed easily. In a clinical environment, the motion monitoring system can be chosen based on availability and tumor location.
For this study, a few limiting compromises had to be made. Only a single, virtual case with one field was investigated. Before clinical application, more studies with real patient data will be necessary. For a first proof of principle, however, the XCAT phantom was chosen as it made it possible to perform the dose reconstructions for irregular motion with high spatial resolution and without imaging artifacts.
The purely translational tumor motion was an artificially favorable scenario for beam tracking of the tumor COM, as there was no residual intra-tumor motion of voxels relative to each other. This was shown by the loss in target coverage with an additional tumor rotation. For MP4DRT, in contrast, more complex motion is no significant challenge, as tumor deformations and rotations are accounted for during treatment planning or mitigated by the intrinsic breath-sampled rescanning that makes MP4DRT also robust against

the temporal structure of the delivery.
In our study, the effect of RBE present in carbon ion therapy was neglected. This was done to simplify the dosimetric interpretation of the measurements. Optimization for a homogeneous absorbed dose yielded a flat dose for efficient motion mitigation measured by the IC array detector and therefore immediate feedback during data acquisition. Planning and delivery of RBE-weighted doses is feasible with MP4D [80] and will be validated in upcoming experiments.
The system was tested with a carbon ion beam but can also be used for protons. The increased scattering and range straggling of protons leads to bigger spot sizes. This yields a loss in conformity, but also reduces sensitivity to motion and the lateral beam position [149]. Consequently, proton deliveries are expect to be less sensitive to tumor tracking errors than carbon treatments.

5.6.3 Clinical prospects

The new technique was implemented into the research version of the DDS of CNAO. This simplifies future clinical implementation at this facility [133].
The required tumor tracking precision of a motion monitoring system for MP4DRT treatments was investigated by adding artificial noise to the ground truth motion signal. For deliveries with ten motion phases, a D95>95 % could be maintained up to a mean absolute tracking error of 1.9 mm. This is in the range of several systems using X-ray radiography [53, 123], MRI [46, 130, 131], ultra-sound [55, 57, 150], or hybrid systems, that build a correlation model optical surface markers and the internal motion. For photon radiotherapy, such systems are already in clinical use, for example the CyberKnife XLTS [60, 61] and the COSMIK system [62].
The used error model for the motion monitoring considers the temporal correlation of errors in a real system. For systems, in which the tumor position is extrapolated from a measured image, the precision is typically measured by comparing the prediction with the measurement in the next frame. As deviations are expected to increase with prediction time, the constant error used in our study is a conservative approach.
The high reproducibility of the dosimetric results for MP4DRT allows for patient-specific 4D-QA [79] even in the case of irregular motion compensated with a complex mitigation strategy. For this, a setup similar to the one in this study could be used.
The next step towards clinical implementation is a simulation study to identify patient groups benefiting from the new delivery technique. This study should be based on imaging data displaying irregular motion. Such data sets can be created from 4DMRI [8, 57, 151]. For selected cases, the setup used in this study can be used with the linear stage performing the tumor motion observed in the patient. In addition, the DDS should be tested using an anthropomorphic phantom [103, 104] observed by a clinical motion monitoring system.

5.7 Conclusions

In the work presented in this chapter, the new motion mitigation MP4DRT was evaluated for the first time on an inhomogeneous, anthropomorphic anatomy. It can deliver highly conformal and homogeneous dose distributions to irregularly moving and rotating tumors, as was experimentally demonstrated. By combining a 4D treatment planning and motion synchronized rescanning strategy with real-time adaptive beam tracking, it was possible to overcome the limitations that so far prevented the application of scanned particle therapy to moving tumors for freely breathing patients. For currently used treatment techniques, fractionation is necessary to average out motion defects in the dose distributions from single deliveries.

Successful motion mitigation in a single delivery therefore is an important step towards the application of promising hypofractionated treatment schemes.

6 Summary and conclusions

In this final chapter, the results presented in the previous chapters are reviewed and discussed. Firstly, a recapitulation defines how the presented work relates to previous work in the field of motion mitigation for scanned ion beam therapy. Secondly, the conclusions reached for the research hypotheses formulated in chapter 1 are summarized. After discussing the strengths and limitations of this thesis, an outlook is given on the next steps towards clinical use of MP4DRT, other possible use cases of the presented dose delivery system and the potential impact of this thesis on the field.

6.1 Context of this work in the field

Radiotherapy treatments of moving tumors would benefit from a conformal dose delivery in order to reduce side effects, enable dose escalation as well as hypofractionated treatment schemes.
Scanned particle therapy enables more conformal treatments than photons thanks to the more favorable depth-dose profile. However, the fundamental properties of ion beams concerning beam range and the interplay between scanning beam and anatomical motion, and the sharp dose gradients challenge the robustness of this technique for moving tumors.
Most particle therapy centers treating moving tumors use beam gating. This yielded good clinical outcomes [48], but increases the treatment time drastically compared to free breathing. Consequently, this limits the patient throughput for the clinics and deteriorates the cost-benefit ratio for particle therapy. A reduction in treatment time would therefore increase accessibility for patients to this form of therapy. In addition, residual motion inside the gating window reduces dose conformity. Baseline drifts are neglected entirely in phase-based gating and further reduce the time efficiency of amplitude based gating [64].
At other centers, deep inhalation breath-hold [65] techniques are the current standard for moving tumors. This technique requires maximal patient collaboration and compliance and a sufficient pulmonary reserve. Also the reproducibility of the breath-hold position needs to be considered. Therefore, this strategy does not suit for all patients [152].
Most treatments in free breathing are currently based on ITVs combined with rescanning. Various 4D optimization strategies have been developed to improve the robustness of target coverage [32, 37, 72, 88, 137]. However, the use of internal margins also necessary for this technique causes dose to healthy tissue. A minimal target volume can be achieved by adapting in real-time to the observed anatomical motion, which can be subject to severe irregularities such as motion amplitude variations and baseline drifts. For photons, real-time adaptive motion mitigation was achieved by beam tracking [60, 153]. However, the achievable dose conformity in photon radiotherapy is limited by the unfavorable depth-dose profile of photons. In addition, photon beam tracking requires the mechanical movement of either a collimator, the patient couch or the entire linear accelerator.
Scanned ion beam therapy offers a much simpler implementation of lateral beam tracking than photons as only magnet currents need to be adapted in order to steer beam positions in real-time. However, so far presented beam tracking strategies could not overcome the ion beam specific challenges.
3D-deformable tracking reacts beam spot by beam spot. This leads to a distortion of the optimized beam grid and thus dose errors [144, 154]. Consequently, it did not perform substantially better than 2D tracking

of the tumor center-of-mass (COM) combined with rescanning [54]. A system using range corrections from the planning 4DCT and lateral tracking vectors directly from the observed motion showed improved dose distributions for a rigid, periodic and translational motion compared to a 4DCT phase only implementation [120], thus proving the potential benefit of such a hybrid approach. A problem of this system was that it used a wedge system for beam range adjustments that needed several milliseconds to adapt for a new spot and therefore was a bottle neck for delivery speed [74]. In addition, the system could not correctly compensate for tumor rotations without the use of real-time corrections highly-dependent on pre-treatment deformable image registration (DIR) [144].
In contrast, the 4D-optimized and motion-synchronized delivery strategy MP4D was shown to be a time efficient motion mitigation technique that was able to deliver highly conformal dose distributions to periodically moving targets. No online adaptation of the beam energy is necessary, which facilitates clinical implementation, and no error-prone DIR is necessary for treatment planning. However, the technique requires additional margins to compensate interfractional changes of the tumor motion [80]. Studies of the effect of intrafractional motion variability were missing, but dose degradations due to irregular motion had to be expected especially from systematic baseline drifts as they are observed in patients [38, 39].
The goal of this work was to develop a new motion mitigation technique for scanned ion beam therapy that combines the conformity of MP4D with the adaptivity of beam tracking to irregular motion, and to develop a framework, both for simulations and experiments, to evaluate its performance in the presence of irregular anatomical motion. A proof-of-principle experiment should demonstrate potential clinical benefits of the new strategy.
This goal was reached with the new real-time adaptive motion mitigation technique MP4DRT. Range changes expected from the planning 4DCT are included into the treatment plan and lateral beam tracking is done in real-time. As the beam energy of single spots is not adapted during delivery and the tracking of the tumor COM is applied to all beamlets, the optimized raster scanning grid is maintained. The implementation does not require a system for real-time range adjustments, which makes it easier to integrate into existing clinical installations. Finally, the synchronization between delivery and anatomical motion imposes a straight-forward implementation of breath-sampled rescanning. In contrast to the already clinically used PCR [138] and the implementation proposed by Poulsen et al. [41], it can even adapt online to variations of the motion period which further increases the robustness of this technique.
The abilities of the MP4DRT implementation were demonstrated in a proof-of-principle experiment. Efforts towards clinical implementation of MP4DRT require clinically feasible motion monitoring systems that are able to track the tumor COM with an accuracy better than 2 mm, see chapter 5. Such systems can built on the previous work on motion monitoring designed for beam tracking [44, 59, 121, 123] and photon treatments [60, 62].
In summary, MP4DRT is a new beam tracking strategy that can compensate range changes and deformations without the need of real-time range adaptations. It enables highly conformal time-resolved treatment planning and incorporates a robust rescanning strategy. An experimental validation suggests, that it can overcome the challenges, that so far prevented the clinical use of real-time adaptive beam tracking. This enables conformal and hypofractionated radiotherapy of moving tumors at acceptable treatment time.

6.2 Research hypotheses

In chapter 1, three research hypotheses were formulated to define the scope of this work. In this section, the corresponding answers given in the previous chapters are discussed.

6.2.1 Hypothesis I

> **Hypothesis I:**
> 4D dose calculation for carbon ion therapy can be precisely performed for irregular motion.

The radiobiological effectiveness of heavy ions like carbon requires dedicated models that account for their relative biological effect, which is non-linear with absorbed dose. Several algorithms implementing these models exist, but they were unsuited to process long series of imaging data depicting irregular anatomical motion. An extension of the dose calculation algorithm TRiP98 to handle irregular motion was presented and experimentally validated in chapter 3. It was demonstrated, that it cannot only reproduce integral dose distributions, but it can even give insight into the time structure of a treatment on timescales as short as 100 ms.
In parallel to this work, one alternative dose calculation algorithm for RBE-weighted doses was published by Meschini et al. [99]. It uses a simplified geometrical model to enable dose calculation when only the motion component of the tumors is known, but not the one of the surrounding tissue. This makes this algorithm useful for a clinical situation, but it limits the precision of the results. In addition, it was only validated with simulations.
The algorithm presented in this thesis uses the 4D-motion information of the entire patient geometry. Its clinical applicability during treatment is therefore challenging, but feasible with advanced image processing strategies [56, 123] or future implementations of MR-guided particle therapy [44]. For research purposes, when full anatomical motion information is available, this enables studies without the limitation of a simplified geometry. This is relevant as the anatomical changes in the entrance channel have a much stronger impact on the dose distribution compared to photons. It was experimentally validated that the algorithm is a working extension of a preexisting 4D dose calculation engine that can now handle irregular motion. The implementation enables future experiments and simulation studies on irregular patient data that were outside the scope of this work.
In summary, both currently available dose calculation algorithms for RBE-weighted doses and irregular motion have different strengths and complement each other. The algorithm presented in this work can be used as ground-truth to validate the algorithm presented by Meschini et al. Where Meschini et al. offers a more straightforward clinical applicability, the implementation in this work enables more detailed insights especially for challenging cases of deforming tumors and inhomogeneous geometries.

6.2.2 Hypothesis II

> **Hypothesis II:**
> The compensation of irregular motion is technically feasible by a combination of multi-phase 4D dose delivery with lateral beam tracking.

In the chapters 4 and 5 of this work, it was demonstrated experimentally that the new motion mitigation technique multi-phase 4D dose delivery with residual tracking (MP4DRT) is able to compensate for irregular motion. In chapter 4, the technical implementation of MP4DRT into the dose delivery system of CNAO was described. The existing implementation of MP4D was extended by adding residual tracking. First, simplified tests in a simple 2D-geometry without range changes demonstrated the ability of the system to adapt the beam delivery in real-time to a motion signal. Both, lateral beam tracking and MP4DRT, achieved similar results. The effects of irregular motion on MP4D deliveries was successfully mitigated by the additional residual tracking. As another important result of this thesis, it was demonstrated that the

homogeneity of the delivered dose distribution depends on the precision of the motion monitoring system, and the precision requirements were quantified. Additional rescanning effectively mitigated this source of error. This suggests that MP4DRT with its intrinsic breath-sampled rescanning is more robust against motion monitoring errors than simple beam tracking.
Those findings could be confirmed in chapter 5. Again, the measured dose homogeneity on the detector behind homogeneous material was similar for lateral retracking and MP4DRT and superior to MP4D with irregular motion. However, the dose reconstructions in an inhomogeneous anthropomorphic geometry revealed a clear advantage in dose homogeneity and target coverage of MP4DRT over lateral beam tracking for all considered motion scenarios. No significant difference between regular and irregular motion scenarios was found in the treatment quality of MP4DRT and excellent target coverage was achieved. It can therefore be concluded, that MP4DRT, which is a combination of MP4D with lateral beam tracking, can successfully mitigate irregular motion in anthropomorphic geometries.

6.2.3 Hypothesis III

> **Hypothesis III:**
> The motion mitigation strategy MP4DRT is able to deliver highly conformal and homogeneous dose distributions to irregularly moving tumors. It synergizes the strengths of beam tracking and MP4D and therefore outperforms more established strategies.

In chapter 5, it was demonstrated that the new MP4DRT technique can deliver highly conformal and homogeneous dose distributions in a complex anthropomorphic geometry including irregular motion, resulting range changes and tumor rotations.
MP4DRT was compared to ITV deliveries with and without rescanning, lateral beam tracking and MP4D. The presented study therefore covers the range from current clinical standard over earlier presented active motion mitigation techniques to the completely new MP4DRT. The experimental validation for irregular motion is the first of its kind and no other experimental study in literature provides a similarly complete comparison over available dose delivery strategies for motion mitigation. The presented study therefore fills an important gap in the development and dosimetric comparison of motion mitigation techniques.
The dosimetric results confirm the research hypothesis. With MP4DRT, it was possible to deliver highly conformal and homogeneous dose distributions to an irregularly moving tumor. Organ at risk sparing similar to a static delivery was possible. MP4DRT outperformed both tracking and MP4D for irregular motion by combining complementary strengths of both previously described methods. Lateral beam tracking yielded a major improvement in OAR sparing and robustness against irregular motion including drifts compared to clinically used ITV rescanning. However, the longitudinal margin needed to maintain target coverage limited the conformity of the high dose volume. In a comparative clinical trial between photons and passively scattered protons, it was shown that the volume of healthy tissue receiving high dose is of special importance for the appearance of severe side effects [5]. While the target coverage in the study presented here was high, it was still limited by range changes. In addition, tracking deliveries were vulnerable to tumor rotations. The treatment planning suggested that higher target coverage could be achieved by combining lateral beam tracking with phase-controlled or breath-sampled rescanning. This result is relevant also to other research groups, who work on the implementation of beam tracking, without a modification of the delivery sequence as it is done in MP4DRT.
MP4D achieved high target coverage and efficient OAR sparing for periodic motion and random changes of the motion amplitude. Tumor rotations do not affect target coverage. However, a systematic drift of the tumor exceeding the PTV margins was a major safety issue for this technique. If for complex cases the

real-time motion monitoring required for MP4DRT is not feasible, MP4D with a slow tracking of only the tumor baseline could be an option. The presented study is only the fifth publication related to experiments with MP4D and the first one considering irregular motion. It therefore significantly extends the knowledge about this strategy.
MP4DRT combined the conformity, target coverage and robustness against rotations achieved by MP4D for periodic motion with the robustness of beam tracking against irregular motion. A sufficient target coverage of D95>95 % was achieved up to a mean absolute tracking error of 1.9 mm for an isotropic target margin of 3 mm. Imaging systems designed for beam tracking in particle therapy or even already in clinical use for photon radiotherapy can already achieve this level of precision, which will facilitate clinical translation. The measurements suggest that a higher tolerance could be achieved by larger margins at the expense of dose conformity. In a clinical setting, the effects of the used motion monitoring system have to be taken into consideration during treatment planning to reach the best dosimetric results.

6.3 Strengths and limitations

The work presented in this thesis has a strong focus on experiments. This was necessary, as the main goal of the thesis was to provide a dose delivery system that can deliver MP4DRT treatments together with a proof-of-principle that the strategy can mitigate irregular motion. The strong experimental focus has considerable benefits for future clinical translation of the methods in this thesis, but also imposed several limitations of the presented work.
The greatest strength of this thesis is that it established a working implementation of the new motion mitigation technique MP4DRT within a research version of a clinical dose delivery system. This allowed to demonstrate the great potential of the newly developed motion mitigation concept beyond a mere theoretical concept. It works also in the reality of a real-time implementation in hardware. The modularity of the design facilitates upgrades and maintenance. The described implementation therefore can be directly imported to the next generation of CNAO's DDS [133] and can serve as an example for independent implementations elsewhere.
An obstacle for testing and validating the DDS implementation of MP4DRT was the limitation of available beamtime at the research facility GSI and limited access to the therapy center CNAO because of the ongoing Covid-19 pandemic. This restricted the possible experiments to only one digital patient case. Also the setup with only a single treatment field was a necessary simplification. More data from a broader, representative group of patients is needed to identify patient groups that will profit most from the new technique. A corresponding simulation study therefore is the first logical step towards clinical use.
At the same time, the used digital XCAT phantom offered opportunities that would not have been available for real patient data. Densely-sampled 4DCT data could be created that enabled amplitude-based dose reconstructions with a high spatial resolution for arbitrary irregular tumor motion. Different motion scenarios could be investigated in the same geometry, thus eliminating the challenge of different anatomies in comparisons between different patients. Also the post-hoc addition of an arbitrary tumor rotation without spoiling of the treatment plans was only possible for the spherical shape of the tumor and the modified vector fields from the updated XCAT software. The inhomogeneity of the phantom was shown to reflect reported measurements from real patient 4DCTs. The size and irregularity of the investigated motion scenarios were in a realistic range [39], even though bigger than on average. The fact that MP4DRT performed well in this rather unfavorable scenario underlines the expected safety of this method also for less extreme cases.
The experimental setups where kept simple on purpose in order to maximize the number of measurements during limited beamtime and to facilitate the debugging of the modified dose delivery system. The focus of

the experiments in chapter 5 was on a virtual lung cancer case as those tumors often have a large motion amplitude and are more frequent than liver or pancreatic tumors. It is a known issue that pencil beam dose calculation algorithms have difficulties with the inhomogeneous lung tissue [155, 156] and sharp density gradients even though these problems are less pronounced for carbon ions compared to protons. The experimental setup was chosen to relate the observed quality of the measured dose distribution directly to the performance of the dose delivery system while neglecting potential deficits of the dose calculation algorithm used for treatment planning and dose reconstructions. Also an idealized, perfect conversion from Hounsfield units to stopping power and no anatomical changes and setup errors between planning 4DCT and irradiation was assumed. A consideration of all clinically relevant error sources were outside the scope of this work. The necessary additional safety margins would spoil the high dose conformity for MP4DRT reported in this study, but also affect the other delivery strategies in a similar fashion [80]. The additional margins would increase the robustness of ITV and MP4D deliveries against baseline drifts, but would not reduce the loss of target coverage of lateral tracking caused by the range changes.

The high target coverage of lateral beam tracking during the 4D treatment planning was achieved by a new target volume definition for lateral beam tracking that was proposed in section 5.2.4. This new trackingITV was constructed in a similar way as a rangeITV and therefore ensures target coverage for lateral beam tracking. It incorporates range margins, but avoids the lateral target extension of the original ITV. The presented treatment planning and dose reconstructions confirm that the loss of target coverage in lateral beam tracking was not caused by underdosage at the proximal and distal edges of the tumor, but rather because of uncompensated longitudinal distortion of the optimized raster grid caused by the anatomical changes in the entrance channel. This demonstrates that the goal of the internal longitudinal margins of the trackingITV was fulfilled. A further development of an implicit definition of a trackingITV by 4D optimization similar to the ITV used for rescanning is current work in progress. Such a definition would also incorporate the expected motion of organs at risk as well as enable the simultaneous optimization of multiple fields.

A significant effort was invested into the accurate computation of log-file based dose calculations. This resulted into a high agreement between measured and reconstructed dose distributions, as was presented in chapters 3 and 5. Thus, reliable volumetric evaluations could be achieved for the experimental validation of MP4DRT and its comparison to other motion mitigation techniques. For every single measurement, the dose reconstruction was confirmed by crosschecks with detector data. As experiments contain the real-time behavior of dose delivery system and accelerator system, they are intrinsically more reliable than simulations.

No realistic motion monitoring system was used at the early demonstration stage of MP4DRT. Instead, artificial errors were added to a motion signal, that is precise enough to be considered ground truth. To the best knowledge of the author, so far no other experimental study used this approach to assess the robustness of a beam tracking strategy against motion monitoring errors. Particular attention was given to the expected temporal correlation of motion monitoring errors. As a result, the study presented in chapter 5 defines the requirements on an arbitrary motion monitoring system rather than demonstrating the suitability of a special system. It was demonstrated that the accuracy reported for several different and already clinically available motion monitoring system is sufficient for an isotropic safety margin as small as 3 mm. It was also shown that the robustness of the target coverage against imperfect motion information can be increased by larger target margins, but this is at the expense of dose conformity.

6.4 Outlook

This sections gives an outlook on the next steps towards clinical use of MP4DRT, alternative uses of the existing DDS implementation and the potential impact of this thesis on the field of particle therapy.

6.4.1 Steps towards clinical use of MP4DRT

The scope of this work was the technical implementation of MP4DRT and a proof that this technique can deliver dose distributions that are dosimetrically superior to other techniques. For this purpose, a single digital lung phantom was sufficient. The next step is a simulation study based on imaging data from real patients. The required data sets showing volumetric irregular motion become available through 4DCT(MRI) [8, 151]. Such a study would give insight about patient groups that will profit most from the new strategy. Open questions are:

1. Is there a lower threshold for the tumor motion amplitude, above which there is a significant improvement of MP4DRT over ITV rescanning?
2. Are there differences between treatments with one and with several fields?
3. The study was performed for the highly irregular lung tissue. What is the effect for the more homogeneous liver or also the pancreas, where interfractional changes pose a significant issue?
4. Is there an effect of RBE on interplay and the performance of motion mitigation techniques?
5. Is the dosimetric advantage of the highly conformal therapy clinically relevant? This could be assessed by NTCP models prior to a clinical transition.

After such a simulation study, the next step would be an experimental confirmation for a subset of cases. For this purpose, the same setup and procedure as described in chapter 5 can be used.
The work presented in chapter 5 contains treatment planning, dose delivery and quality assurance in the sense of an evaluation of detector measurements and log-file based dose reconstructions. Nevertheless, it is not a complete end-to-end study. Missing elements are the creation of 4DCT images from a real, anthropomorphic phantom, that would also be used for dosimetric tests and has to be monitored by a clinical motion monitoring system. Such a study would be a key step before animal and patient studies on the way towards clinical use.
The work presented in this thesis contributes to the development of the next generation of CNAO's dose delivery system [133]. The technical requirements of a clinical implementation at this center are therefore planned to be fulfilled within the next few years. CNAO's DDS is a commercial product that can also be transferred to other synchrotron centers.

6.4.2 MP4DRT beam delivery with alternative plan optimization strategies

In this thesis, one treatment planning strategy per delivery technique was used.This approach was made in order to reduce the number of parameters for the experimental comparison as deliveries were limited by the amount of available beamtime. For the MP4D and MP4DRT delivery technique, the single phase uniform dose optimization was used for treatment planning. In principle, the technical implementation of MP4D and MP4DRT is open to other treatment planning and gating strategies. This can be useful for further developments of those strategies themselves and can be used as reference for other motion mitigation

strategies. The following combinations can be achieved without further modifications of the dose delivery system and are therefore proposed for future investigation:

Respiratory gating with residual tracking: MP4DRT with beam spots only in those plans dedicated to a single or few phases. The phase would be detected based on a motion surrogate. The residual tumor motion would be mitigated by lateral beam tracking. This would allow for a conformal gating window safe-guarded against baseline drifts. It would avoid the phases of fast tumor motion between in- and exhale, and could also be useful for patients with a highly variable end-inhale peak.

Breath-sampled rescanning: MP4D delivery with identical phase plans optimized for an ITV. It was reported, that breath-sampled rescanning improved delivery quality significantly over conventional rescanning in experiments and simulations [41, 42]. This is in agreement with the observed difference in target coverage and dose homogeneity between planned and reconstructed dose for the ITV rescanning deliveries in chapter 5. This would be the most conservative use of MP4D and therefore most easy to implement into clinical practice.

Breath-sampled retracking: MP4DRT delivery with identical phase plans. The treatment planning in chapter 5 suggests that breath-sampling would improve the target coverage compared to simple retracking. In a more homogeneous geometry than the lung, for example for liver cancers, the disadvantage in dose conformity compared to MP4DRT might be reduced and outweighed by the simpler planning of only a single treatment plan.

Phase-IMPT: MP4D, but instead of optimizing all phase plans separately (single phase uniform dose), all phase plans could be optimized simultaneously. This would enable the exploitation of differential motion between organs at risk and the target. In the past, a similar approach was proposed for a less efficient beam delivery strategy [154].

Phase-IMPT with residual tracking: Same as Phase-IMPT, but with the residual tracking implemented in MP4DRT in order to react to irregular motion.

Even though creating new challenges and requiring a major redesign of the DDS, the concept of MP4DRT can in principle be combined with a global range adjustment for the entire tumor or with deformable 2D and 3D tracking instead of the only lateral tracking of the tumor COM. As the tracking would only correct the residual deviation between planned and observed motion, smaller corrections than for conventional deformable tracking are expected.

6.4.3 Potential impact on the field

There are many research groups worldwide that perform simulation studies for conventional delivery techniques available with the commercial treatment machines routinely used at the corresponding clinical particle therapy facilities. Only few of them have low-level access to the dose delivery system at their center. This presents a bottleneck in the development and experimental test of new motion mitigation techniques. The flexibility of the DDS designed to apply different motion mitigation strategies presents the ideal platform to test such techniques. This was demonstrated by selecting conventional static and ITV deliveries, lateral real-time tracking, the adaption of the beam delivery sequence of MP4D alone or together with lateral tracking as MP4DRT. Thus, the DDS can also serve as a platform for new, so far unknown treatment planning strategies.
Successful clinical trials using MP4DRT at CNAO might trigger the interest of vendors to offer similar abilities within commercial systems. The detailed description of the implementation given in this thesis

can serve as a model for imitation. At this point, it has to be underlined that the concept of MP4DRT can be applied without major modification also to proton cyclotrons. For an accelerator providing a continuous particle beam, an even higher duty cycle compared to synchrotron with spill pauses has to be expected, reducing setbacks in treatment delivery time with MP4DRT at synchrotrons. No additional hardware than the DDS itself and a motion monitoring system are necessary for an implementation into an existing facility. In summary, the work presented in this thesis has the potential to be a major step towards the clinical implementation of conformal, real-time adaptive particle therapy. As this would enable and improve the treatment of several moving cancer types with a poor prognosis, such as lung, liver or pancreatic tumors, it would also increases the cost-benefit ratio of particle therapy. This could motivate the construction of new centers and therefore increase accessibility to particle therapy in general.

6.5 Summary

The new motion mitigation technique multi-phase 4D dose delivery with residual tracking presented in this work is able to deliver highly conformal dose distributions to irregularly moving tumors using ion beams. The technique was implemented into the research version of a clinical dose delivery system. Its potential benefits and the technical feasibility were demonstrated based on a digital lung phantom. It was shown that the new technique overcomes limitations inherent to other motion mitigation techniques presented in the past. This poses an important step towards the clinical implementation of real-time adaptive particle therapy. The new technique enables conformal particle therapy for moving tumors. It therefore has the potential to improve the prognosis for many patients, especially those suffering from lung, pancreas and liver cancer. The validation of a dedicated dose calculation algorithm enables further simulation studies on non-periodic patient data which is the next step towards clinical use of the new strategy.

Bibliography

[1] Robert Koch Institut (ed.) and the Association of Population-based Cancer Registries in Germany (ed.) *"Cancer in Germany in 2015/2016"*. 12th ed. Berlin: Robert Koch-Institut, 2020, pp. 1–158. DOI: 10.25646/6825.

[2] William D. Travis. "Update on small cell carcinoma and its differentiation from squamous cell carcinoma and other non-small cell carcinomas". In: *Modern Pathology* 25 (2012). DOI: 10.1038/modpathol.2011.150.

[3] Peter Goldstraw et al. "The IASLC Lung Cancer Staging Project: Proposals for Revision of the TNM Stage Groupings in the Forthcoming (Eighth) Edition of the TNM Classification for Lung Cancer". In: *Journal of Thoracic Oncology* 11.1 (2016), pp. 39–51. DOI: 10.1016/J.JTHO.2015.09.009.

[4] Jeffrey D. Bradley et al. "Standard-dose versus high-dose conformal radiotherapy with concurrent and consolidation carboplatin plus paclitaxel with or without cetuximab for patients with stage IIIA or IIIB non-small-cell lung cancer (RTOG 0617): A randomised, two-by-two factorial p". In: *The Lancet Oncology* 16.2 (2015). DOI: 10.1016/S1470-2045(14)71207-0.

[5] Zhongxing Liao et al. "Bayesian Adaptive Randomization Trial of Passive Scattering Proton Therapy and Intensity-Modulated Photon Radiotherapy for Locally Advanced Non–Small-Cell Lung Cancer". In: *Journal of Clinical Oncology* 36.18 (2018), p. 1813. DOI: 10.1200/JCO.2017.74.0720.

[6] Shohei Kawashiro et al. "Multi-institutional Study of Carbon-ion Radiotherapy for Locally Advanced Pancreatic Cancer: Japan Carbon-ion Radiation Oncology Study Group (J-CROS) Study 1403 Pancreas". In: *International Journal of Radiation Oncology*Biology*Physics* 101.5 (2018), pp. 1212–1221. DOI: 10.1016/J.IJROBP.2018.04.057.

[7] Giorgia Meschini et al. "Virtual 4DCT from 4DMRI for the management of respiratory motion in carbon ion therapy of abdominal tumors". In: *Medical Physics* 47.3 (2020), pp. 909–916. DOI: 10.1002/mp.13992.

[8] Alisha Duetschler et al. "Synthetic 4DCT(MRI) lung phantom generation for 4D radiotherapy and image guidance investigations". In: *Medical Physics* (2022). DOI: 10.1002/MP.15591.

[9] W. P. Segars et al. "Realistic CT simulation using the 4D XCAT phantom". In: *Medical Physics* 35.8 (2008), pp. 3800–3808. DOI: 10.1118/1.2955743.

[10] Michelle Lis et al. "A modular dose delivery system for treating moving targets with scanned ion beams: Performance and safety characteristics, and preliminary tests". In: *Physica Medica* 76 (2020), pp. 307–316. DOI: 10.1016/j.ejmp.2020.07.029.

[11] Gabrielle LeDoeuff. "Beam tracking for compensation of irregular motion (MSc Thesis)". Master thesis. Darmstadt: Technical University of Darmstadt, 2018.

[12] M. Krämer and M. Durante. "Ion beam transport calculations and treatment plans in particle therapy". In: *European Physical Journal D* 60.1 (2010). DOI: 10.1140/epjd/e2010-00077-8.

[13] R. Serber. "Nuclear reactions at high energies". In: *Physical Review* 72.11 (1947). DOI: 10.1103/PhysRev.72.1114.

[14] Dieter Schardt, Thilo Elsässer, and Daniela Schulz-Ertner. *Heavy-ion tumor therapy: Physical and radiobiological benefits*. 2010. DOI: 10.1103/RevModPhys.82.383.

[15] Bruno Benedetto Rossi. *High-energy particles*. Prentice-Hall Physics Series. Englewood Cliffs: Prentice-Hall, 1952.

[16] Marco Durante and Harald Paganetti. "Nuclear physics in particle therapy: a review". In: *Reports on Progress in Physics* 79.9 (2016), p. 096702. DOI: 10.1088/0034-4885/79/9/096702.

[17] Upadhyayula Sai Srinivas et al. "ROS and the DNA damage response in cancer". In: *Redox Biology* 25 (2019), p. 101084. DOI: 10.1016/J.REDOX.2018.101084.

[18] Ben Milborne et al. "The Use of Biomaterials in Internal Radiation Therapy". In: *Recent Progress in Materials 2020, Vol. 2, Page 1* 2.2 (2020), pp. 1–1. DOI: 10.21926/RPM.2002012.

[19] K H Chadwick and H P Leenhouts. "A molecular theory of cell survival". In: *Physics in Medicine and Biology* 18.1 (1973), pp. 78–87. DOI: 10.1088/0031-9155/18/1/007.

[20] Stephen Joseph McMahon. "The linear quadratic model: Usage, interpretation and challenges". In: *Physics in Medicine and Biology* 64.1 (2019). DOI: 10.1088/1361-6560/aaf26a.

[21] Cody D. Schlaff et al. "Bringing the heavy: Carbon ion therapy in the radiobiological and clinical context". In: *Radiation Oncology* 9.1 (2014), pp. 1–19. DOI: 10.1186/1748-717X-9-88/TABLES/1.

[22] M. Scholz et al. "Computation of cell survival in heavy ion beams for therapy: The model and its approximation". In: *Radiation and Environmental Biophysics* 36.1 (1997), pp. 59–66. DOI: 10.1007/s004110050055.

[23] M Krämer et al. "Treatment planning for heavy-ion radiotherapy: Physical beam model and dose optimization". In: *Physics in Medicine and Biology* 45.11 (2000), pp. 3299–3317. DOI: 10.1088/0031-9155/45/11/313.

[24] Tabea Pfuhl, Thomas Friedrich, and Michael Scholz. "Prediction of Cell Survival after Exposure to Mixed Radiation Fields with the Local Effect Model". In: *Radiation Research* 193.2 (2020). DOI: 10.1667/RR15456.1.

[25] Harald Paganetti and Drosoula Giantsoudi. *Relative Biological Effectiveness Uncertainties and Implications for Beam Arrangements and Dose Constraints in Proton Therapy*. 2018. DOI: 10.1016/j.semradonc.2018.02.010.

[26] Henning Willers et al. "Toward A variable RBE for proton beam therapy". In: *Radiotherapy and Oncology* 128.1 (2018), pp. 68–75. DOI: 10.1016/J.RADONC.2018.05.019.

[27] Makoto ANZAI et al. "Safety and Efficacy of Carbon-ion Radiotherapy Alone for Stage III Non-small Cell Lung Cancer". In: *Anticancer Research* 40.1 (2020), 379 LP –386. DOI: 10.21873/anticanres.13963.

[28] Tadashi Kamada et al. "Carbon ion radiotherapy in Japan: an assessment of 20 years of clinical experience". In: *The Lancet Oncology* 16.2 (2015), e93–e100. DOI: 10.1016/S1470-2045(14)70412-7.

[29] Daniel Richter. "Treatment planning for tumors with residual motion in scanned ion beam therapy". PhD thesis. Darmstadt, 2012.

[30] F Bourhaleb et al. "Monte Carlo simulations of ripple filters designed for proton and carbon ion beams in hadrontherapy with active scanning technique". In: *Journal of Physics: Conference Series* 102 (2008), p. 012002. DOI: 10.1088/1742-6596/102/1/012002.

[31] ICRU. “ICRU Report 93: Prescribing, Recording, and Reporting Light Ion Beam”. In: *Journal of the ICRU* 16.1-2 (2016).

[32] Christian Graeff, Marco Durante, and Christoph Bert. “Motion mitigation in intensity modulated particle therapy by internal target volumes covering range changes”. In: *Medical Physics* 39.10 (2012), pp. 6004–6013. DOI: 10.1118/1.4749964.

[33] M Wolf et al. “Robust treatment planning with 4D intensity modulated carbon ion therapy for multiple targets in stage IV non-small cell lung cancer”. In: *Physics in Medicine & Biology* 65.21 (2020), p. 215012. DOI: 10.1088/1361-6560/aba1a3.

[34] D. Richter et al. “Upgrade and benchmarking of a 4D treatment planning system for scanned ion beam therapy”. In: *Medical Physics* 40.5 (2013). DOI: 10.1118/1.4800802.

[35] F Albertini, E B Hug, and A J Lomax. “Is it necessary to plan with safety margins for actively scanned proton therapy?” In: *Physics in Medicine and Biology* 56.14 (2011), pp. 4399–4413. DOI: 10.1088/0031-9155/56/14/011.

[36] Harald Paganetti, Clemens Grassberger, and Gregory C. Sharp. “Physics of Particle Beam and Hypofractionated Beam Delivery in NSCLC”. In: *Seminars in radiation oncology* 31.2 (2021), p. 162. DOI: 10.1016/J.SEMRADONC.2020.11.004.

[37] Kristjan Anderle et al. “Treatment planning with intensity modulated particle therapy for multiple targets in stage IV non-small cell lung cancer”. In: *Physics in Medicine and Biology* 63.2 (2018), p. 025034. DOI: 10.1088/1361-6560/aa9c62.

[38] Seishin Takao et al. “Intrafractional baseline shift or drift of lung tumor motion during gated radiation therapy with a real-time tumor-tracking system a preliminary version of this study was presented at the 55th Annual Meeting of the American Society for Radiation Oncology,” in: *International Journal of Radiation Oncology Biology Physics* 94.1 (2016), pp. 172–180. DOI: 10.1016/j.ijrobp.2015.09.024.

[39] Jennifer Dhont et al. “The long- and short-term variability of breathing induced tumor motion in lung and liver over the course of a radiotherapy treatment”. In: *Radiotherapy and Oncology* 126.2 (2018), pp. 339–346. DOI: 10.1016/j.radonc.2017.09.001.

[40] Christoph Bert, Sven O Grözinger, and Eike Rietzel. “Quantification of interplay effects of scanned particle beams and moving targets”. In: *Physics in Medicine and Biology* 53.9 (2008), pp. 2253–2265. DOI: 10.1088/0031-9155/53/9/003.

[41] Per Rugaard Poulsen et al. “Efficient Interplay Effect Mitigation for Proton Pencil Beam Scanning by Spot-Adapted Layered Repainting Evenly Spread out Over the Full Breathing Cycle”. In: *International Journal of Radiation Oncology Biology Physics* 100.1 (2018). DOI: 10.1016/j.ijrobp.2017.09.043.

[42] E. Engwall, L. Glimelius, and E. Hynning. “Effectiveness of different rescanning techniques for scanned proton radiotherapy in lung cancer patients”. In: *Physics in Medicine and Biology* 63.9 (2018). DOI: 10.1088/1361-6560/aabb7b.

[43] Harald Paganetti. “Range uncertainties in proton therapy and the role of Monte Carlo simulations”. In: *Physics in Medicine and Biology* 57.11 (2012), R99–R117. DOI: 10.1088/0031-9155/57/11/R99.

[44] Aswin Hoffmann et al. “MR-guided proton therapy: A review and a preview”. In: *Radiation Oncology* 15.1 (2020), pp. 1–13. DOI: 10.1186/S13014-020-01571-X/FIGURES/5.

[45] B W Raaymakers, A. J.E. Raaijmakers, and J. J.W. Lagendijk. “Feasibility of MRI guided proton therapy: Magnetic field dose effects”. In: *Physics in Medicine and Biology* 53.20 (2008), pp. 5615–5622. DOI: 10.1088/0031-9155/53/20/003.

[46] Laura I Cerviño, Jiang Du, and Steve B Jiang. “MRI-guided tumor tracking in lung cancer radiotherapy”. In: *Physics in Medicine and Biology* 56.13 (2011), pp. 3773–3785. DOI: 10.1088/0031-9155/56/13/003.

[47] Giorgia Meschini et al. “An MRI framework for respiratory motion modelling validation”. In: *Journal of Medical Imaging and Radiation Oncology* 65.3 (2021). DOI: 10.1111/1754-9485.13175.

[48] Katsuyuki Shirai et al. “Clinical outcomes using carbon-ion radiotherapy and dose-volume histogram comparison between carbon-ion radiotherapy and photon therapy for T2b-4N0M0 non-small cell lung cancer—A pilot study”. In: *PLOS ONE* 12.4 (2017), e0175589. DOI: 10.1371/JOURNAL.PONE.0175589.

[49] K. Laube et al. “4D particle therapy PET simulation for moving targets irradiated with scanned ion beams”. In: *Physics in Medicine and Biology* 58.3 (2013), pp. 513–533. DOI: 10.1088/0031-9155/58/3/513.

[50] Yasushi Iseki et al. “Range verification system using positron emitting beams for heavy-ion radiotherapy”. In: *Physics in Medicine and Biology* 49.14 (2004), pp. 3179–3195. DOI: 10.1088/0031-9155/49/14/012.

[51] Timo Steinsberger et al. “Presentation: Simultaneous cancer treatment and online imaging with radioactive ion beams at FAIR”. In: *1st International Biophysics Collaboration Meeting*. Darmstadt, 2019.

[52] Daria Boscolo et al. “Radioactive Beams for Image-Guided Particle Therapy: The BARB Experiment at GSI”. In: *Frontiers in Oncology* 11 (2021). DOI: 10.3389/fonc.2021.737050.

[53] Ruijiang Li et al. “Real-time volumetric image reconstruction and 3D tumor localization based on a single x-ray projection image for lung cancer radiotherapy”. In: *Medical Physics* 37.6 (2010), pp. 2822–2826. DOI: 10.1118/1.3426002.

[54] Ye Zhang et al. “Online image guided tumour tracking with scanned proton beams: A comprehensive simulation study”. In: 59.24 (2014), pp. 7793–7817. DOI: 10.1088/0031-9155/59/24/7793.

[55] Andrew J. Shepard et al. “A block matching based approach with multiple simultaneous templates for the real-time 2D ultrasound tracking of liver vessels”. In: *Medical Physics* 44.11 (2017), pp. 5889–5900. DOI: 10.1002/MP.12574.

[56] Alina Giger et al. “Liver-ultrasound based motion modelling to estimate 4D dose distributions for lung tumours in scanned proton therapy”. In: *Physics in Medicine and Biology* 65.23 (2020), p. 235050. DOI: 10.1088/1361-6560/abaa26.

[57] Miriam Krieger et al. “Liver-ultrasound-guided lung tumour tracking for scanned proton therapy: a feasibility study”. In: *Physics in Medicine & Biology* 66.3 (2021), p. 035011. DOI: 10.1088/1361-6560/abcde6.

[58] Muyinatu A. Lediju Bell et al. “In vivo reproducibility of robotic probe placement for a novel ultrasound-guided radiation therapy system”. In: *Journal of Medical Imaging* 1.02 (2014). DOI: 10.1117/1.jmi.1.2.025001.

[59] Matteo Seregni et al. “Real-time tumor tracking with an artificial neural networks-based method: A feasibility study”. In: *Physica Medica* 29.1 (2013), pp. 48–59. DOI: 10.1016/j.ejmp.2011.11.005.

[60] W. Kilby et al. *The CyberKnife® robotic radiosurgery system in 2010*. 2010. DOI: 10.1177/153303461000900502.

[61] Jinhong Jung et al. "Verification of Accuracy of CyberKnife Tumor-tracking Radiation Therapy Using Patient-specific Lung Phantoms". In: *International Journal of Radiation Oncology*Biology*Physics* 92.4 (2015), pp. 745–753. DOI: 10.1016/J.IJROBP.2015.02.055.

[62] Jenny Bertholet et al. "Automatic online and real-time tumour motion monitoring during stereotactic liver treatments on a conventional linac by combined optical and sparse monoscopic imaging with kilovoltage x-rays (COSMIK)". In: *Physics in Medicine & Biology* 63.5 (2018), p. 055012. DOI: 10.1088/1361-6560/aaae8b.

[63] Gauthier Bouilhol et al. "Is abdominal compression useful in lung stereotactic body radiation therapy? A 4DCT and dosimetric lobe-dependent study". In: *Physica Medica* 29.4 (2013), pp. 333–340. DOI: 10.1016/J.EJMP.2012.04.006.

[64] Shinichiro Mori et al. "Amplitude-based gated phase-controlled rescanning in carbon-ion scanning beam treatment planning under irregular breathing conditions using lung and liver 4DCTs". In: (2014). DOI: 10.1093/jrr/rru032.

[65] Judit Boda-Heggemann et al. "Deep Inspiration Breath Hold—Based Radiation Therapy: A Clinical Review". In: *International Journal of Radiation Oncology*Biology*Physics* 94.3 (2016), pp. 478–492. DOI: 10.1016/J.IJROBP.2015.11.049.

[66] Michael John Parkes et al. "The feasibility, safety and optimization of multiple prolonged breath-holds for radiotherapy". In: *Radiotherapy and Oncology* 141 (2019), pp. 296–303. DOI: 10.1016/J.RADONC.2019.06.014.

[67] Ch Bert et al. "Rescanning to mitigate the impact of motion in scanned particle therapy *". In: *GSI Scientific Report 2008* (2009), p. 397.

[68] Takuji Furukawa et al. "Design study of a raster scanning system for moving target irradiation in heavy-ion radiotherapy". In: *Medical Physics* 34.3 (2007), pp. 1085–1097. DOI: 10.1118/1.2558213.

[69] Joao Seco et al. "Breathing interplay effects during proton beam scanning: simulation and statistical analysis". In: *Physics in Medicine and Biology* 54.14 (2009), N283–N294. DOI: 10.1088/0031-9155/54/14/N01.

[70] Suresh Rana and Anatoly B. Rosenfeld. "Investigating volumetric repainting to mitigate interplay effect on 4D robustly optimized lung cancer plans in pencil beam scanning proton therapy". In: *Journal of Applied Clinical Medical Physics* 22.3 (2021), pp. 107–118. DOI: 10.1002/ACM2.13183.

[71] Kai Dolde et al. "4DMRI-based investigation on the interplay effect for pencil beam scanning proton therapy of pancreatic cancer patients". In: *Radiation Oncology* 14.1 (2019), pp. 1–13. DOI: 10.1186/S13014-019-1231-2/FIGURES/8.

[72] Takayuki Kanai et al. "Four-dimensional carbon-ion pencil beam treatment planning comparison between robust optimization and range-adapted internal target volume for respiratory-gated liver and lung treatment". In: *Physica Medica* 80 (2020), pp. 277–287. DOI: 10.1016/j.ejmp.2020.11.009.

[73] Marco Riboldi, Roberto Orecchia, and Guido Baroni. "Real-time tumour tracking in particle therapy: Technological developments and future perspectives". In: *The Lancet Oncology* 13.9 (2012). DOI: 10.1016/S1470-2045(12)70243-7.

[74] Nami Saito et al. “Speed and accuracy of a beam tracking system for treatment of moving targets with scanned ion beams”. In: *Physics in Medicine and Biology* 54.16 (2009), pp. 4849–4862. DOI: 10.1088/0031-9155/54/16/001.

[75] Christoph Bert et al. “Dosimetric precision of an ion beam tracking system”. In: *Radiation Oncology* 5.1 (2010). DOI: 10.1186/1748-717X-5-61.

[76] Christoph Bert and Eike Rietzel. “4D treatment planning for scanned ion beams”. In: *Radiation Oncology* 2.1 (2007), pp. 1–10. DOI: 10.1186/1748-717X-2-24/.

[77] Christian Graeff et al. “A 4D-optimization concept for scanned ion beam therapy”. In: *Radiotherapy and Oncology* 109.3 (2013). DOI: 10.1016/j.radonc.2013.09.018.

[78] Christian Graeff. “Motion mitigation in scanned ion beam therapy through 4D-optimization”. In: *Physica Medica* 30.5 (2014), pp. 570–577. DOI: 10.1016/j.ejmp.2014.03.011.

[79] Michelle Lis et al. “A Modular System for Treating Moving Anatomical Targets With Scanned Ion Beams at Multiple Facilities: Pre-Clinical Testing for Quality and Safety of Beam Delivery”. In: *Frontiers in Oncology* 11 (2021). DOI: 10.3389/fonc.2021.620388.

[80] Christian Graeff. “Robustness of 4D-optimized scanned carbon ion beam therapy against interfractional changes in lung cancer”. In: *Radiotherapy and Oncology* 122.3 (2017), pp. 387–392. DOI: 10.1016/j.radonc.2016.12.017.

[81] Timo Steinsberger et al. “Extension of RBE-weighted 4D particle dose calculation for non-periodic motion”. In: *Physica Medica* 91 (2021), pp. 62–72. DOI: 10.1016/j.ejmp.2021.10.009.

[82] Marco Durante and Jay S. Loeffler. “Charged particles in radiation oncology”. In: *Nature Reviews Clinical Oncology* 7.1 (2010), pp. 37–43. DOI: 10.1038/nrclinonc.2009.183.

[83] Cai Grau et al. “Particle therapy in Europe”. In: *Molecular Oncology* 14.7 (2020), pp. 1492–1499. DOI: 10.1002/1878-0261.12677.

[84] C. Bert and M. Durante. “Motion in radiotherapy: Particle therapy”. In: *Physics in Medicine and Biology* 56.16 (2011). DOI: 10.1088/0031-9155/56/16/R01.

[85] Pengbo He and Shinichiro Mori. “Perturbation analysis of 4D dose distribution for scanned carbon-ion beam radiotherapy”. In: *Physica Medica* 74 (2020). DOI: 10.1016/j.ejmp.2020.05.003.

[86] Christoph Bert and Klaus Herfarth. “Management of organ motion in scanned ion beam therapy”. In: *Radiation Oncology* 12.1 (2017), pp. 1–6. DOI: 10.1186/s13014-017-0911-z.

[87] Christian Graeff et al. “Multigating, a 4D optimized beam tracking in scanned ion beam therapy”. In: *Technology in Cancer Research and Treatment* 13.6 (2014), pp. 497–504. DOI: 10.7785/tcrtexpress.2013.600277.

[88] T. Pfeiler et al. “4D robust optimization in pencil beam scanning proton therapy for hepatocellular carcinoma”. In: *Journal of Physics: Conference Series*. Vol. 1154. 1. Institute of Physics Publishing, 2019, p. 012021. DOI: 10.1088/1742-6596/1154/1/012021.

[89] A. Meijers et al. “Log file-based dose reconstruction and accumulation for 4D adaptive pencil beam scanned proton therapy in a clinical treatment planning system: Implementation and proof-of-concept”. In: *Medical Physics* 46.3 (2019), pp. 1140–1149. DOI: 10.1002/mp.13371.

[90] S. S. Vedam et al. “Acquiring a four-dimensional computed tomography dataset using an external respiratory signal”. In: *Physics in Medicine and Biology* 48.1 (2003), pp. 45–62. DOI: 10.1088/0031-9155/48/1/304.

[91] Arturs Meijers et al. “Evaluation of interplay and organ motion effects by means of 4D dose reconstruction and accumulation”. In: *Radiotherapy and Oncology* 150 (2020), pp. 268–274. DOI: 10.1016/j.radonc.2020.07.055.

[92] Tuathan O’Shea et al. “Review of ultrasound image guidance in external beam radiotherapy part II: Intra-fraction motion management and novel applications”. In: *Physics in Medicine and Biology* 61.8 (2016), R90–R137. DOI: 10.1088/0031-9155/61/8/R90.

[93] Ross I Berbeco et al. “Integrated radiotherapy imaging system (IRIS): Design considerations of tumour tracking with linac gantry-mounted diagnostic x-ray systems with flat-panel detectors”. In: *Physics in Medicine and Biology* 49.2 (2004), pp. 243–255. DOI: 10.1088/0031-9155/49/2/005.

[94] Bin Dong et al. “Optimal surface marker locations for tumor motion estimation in lung cancer radiotherapy”. In: *Physics in Medicine and Biology* 57.24 (2012), pp. 8201–8215. DOI: 10.1088/0031-9155/57/24/8201. arXiv: 1204.4719.

[95] Tomasz Kubiak. “Particle therapy of moving targets-the strategies for tumour motion monitoring and moving targets irradiation”. In: *British Journal of Radiology* 89.1066 (2016). DOI: 10.1259/bjr.20150275.

[96] Shinichiro Mori, Antje-Christin Knopf, and Kikuo Umegaki. “Motion management in particle therapy”. In: *Medical Physics* 45.11 (2018), e994–e1010. DOI: 10.1002/mp.12679.

[97] Justin Phillips et al. “Computing proton dose to irregularly moving targets”. In: *Physics in Medicine and Biology* 59.15 (2014). DOI: 10.1088/0031-9155/59/15/4261.

[98] Giorgia Meschini et al. “Validation of a model for physical dose variations in irregularly moving targets treated with carbon ion beams”. In: *Medical Physics* 46.8 (2019), pp. 3663–3673. DOI: 10.1002/mp.13662.

[99] Giorgia Meschini et al. “Modeling RBE-weighted dose variations in irregularly moving abdominal targets treated with carbon ion beams”. In: *Medical Physics* 47.7 (2020), pp. 2768–2778. DOI: 10.1002/mp.14135.

[100] Giorgia Meschini et al. “Virtual 4DCT from 4DMRI for the management of respiratory motion in carbon ion therapy of abdominal tumors”. In: *Medical Physics* 47.3 (2020), pp. 909–916. DOI: 10.1002/mp.13992.

[101] Kinga Bernatowicz et al. “Four-Dimensional Dose Reconstruction for Scanned Proton Therapy Using Liver 4DCT-MRI”. In: *International Journal of Radiation Oncology Biology Physics* 95.1 (2016), pp. 216–223. DOI: 10.1016/j.ijrobp.2016.02.050.

[102] W. P. Segars et al. “4D XCAT phantom for multimodality imaging research”. In: *Medical Physics* 37.9 (2010), pp. 4902–4915. DOI: 10.1118/1.3480985.

[103] Stefanie Ehrbar et al. “Respiratory motion-management in stereotactic body radiation therapy for lung cancer – A dosimetric comparison in an anthropomorphic lung phantom (LuCa)”. In: *Radiotherapy and Oncology* 121.2 (2016). DOI: 10.1016/j.radonc.2016.10.011.

[104] N Kostiukhina et al. “Dynamic lung phantom commissioning for 4D dose assessment in proton therapy”. In: *Physics in Medicine and Biology* 64.23 (2019), p. 235001. DOI: 10.1088/1361-6560/ab5132.

[105] N Kostiukhina et al. “Erratum: Time-resolved dosimetry for validation of 4D dose calculation in PBS proton therapy (2020 Phys. Med. Biol. 65 125015)”. In: *Physics in Medicine & Biology* 65.20 (2020), p. 209601. DOI: 10.1088/1361-6560/abaaba.

[106] Harald Paganetti. “Relative biological effectiveness (RBE) values for proton beam therapy. Variations as a function of biological endpoint, dose, and linear energy transfer”. In: *Physics in Medicine and Biology* 59.22 (2014). DOI: 10.1088/0031-9155/59/22/R419.

[107] M. Krämer and M. Scholz. “Rapid calculation of biological effects in ion radiotherapy”. In: *Physics in Medicine and Biology* 51.8 (2006), pp. 1959–1970. DOI: 10.1088/0031-9155/51/8/001.

[108] Thilo Elsässer, Michael Krämer, and Michael Scholz. “Accuracy of the Local Effect Model for the Prediction of Biologic Effects of Carbon Ion Beams In Vitro and In Vivo”. In: *International Journal of Radiation Oncology Biology Physics* 71.3 (2008). DOI: 10.1016/j.ijrobp.2008.02.037.

[109] Thilo Elsässer et al. “Quantification of the relative biological effectiveness for ion beam radiotherapy: Direct experimental comparison of proton and carbon ion beams and a novel approach for treatment planning”. In: *International Journal of Radiation Oncology Biology Physics* 78.4 (2010). DOI: 10.1016/j.ijrobp.2010.05.014.

[110] Christian Alliger. “Zeitlich aufgelöste Dosisberechnung für gescannte Kohlenstoffionen auf sequentiellen Bilddaten zur Erfassung unregelmäßiger Bewegungen (Master Thesis)”. Master thesis. Darmstadt: Technical University of Darmstadt, 2018.

[111] G. Aricò et al. “Investigation of mixed ion fields in the forward direction for 220.5 MeV/u helium ion beams: Comparison between water and PMMA targets”. In: *Physics in Medicine and Biology* 62.20 (2017). DOI: 10.1088/1361-6560/aa875e.

[112] Lydia J. Wilson, Wayne D. Newhauser, and Christopher W. Schneider. “An objective method to evaluate radiation dose distributions varying by three orders of magnitude”. In: *Medical Physics* 46.4 (2019), pp. 1888–1895. DOI: 10.1002/mp.13420.

[113] Anthony E. Lujan, James M. Balter, and Randall K. Ten Haken. “A method for incorporating organ motion due to breathing into 3D dose calculations in the liver: Sensitivity to variations in motion”. In: *Medical Physics* 30.10 (2003), pp. 2643–2649. DOI: 10.1118/1.1609057.

[114] Jun ichi Saitoh et al. “Hypofractionated carbon-ion radiotherapy for stage I peripheral nonsmall cell lung cancer (GUNMA0701): Prospective phase II study”. In: *Cancer Medicine* 8.15 (2019). DOI: 10.1002/cam4.2561.

[115] Goro Kasuya et al. “Progressive hypofractionated carbon-ion radiotherapy for hepatocellular carcinoma: Combined analyses of 2 prospective trials”. In: *Cancer* 123.20 (2017). DOI: 10.1002/cncr.30816.

[116] Christoph Bert et al. “Scanned carbon beam irradiation of moving films: Comparison of measured and calculated response”. In: *Radiation Oncology* 7.1 (2012). DOI: 10.1186/1748-717X-7-55.

[117] Charalampos Kalantzopoulos et al. “Organ motion quantification and margins evaluation in carbon ion therapy of abdominal lesions”. In: *Physica Medica* 75 (2020), pp. 33–39. DOI: 10.1016/j.ejmp.2020.05.014.

[118] A. Gemmel et al. “Calculation and experimental verification of the RBE-weighted dose for scanned ion beams in the presence of target motion”. In: *Physics in Medicine and Biology* 56.23 (2011), pp. 7337–7351. DOI: 10.1088/0031-9155/56/23/001.

[119] Bjorn Eiben et al. “Consistent and invertible deformation vector fields for a breathing anthropomorphic phantom: A post-processing framework for the XCAT phantom”. In: *Physics in Medicine and Biology* 65.16 (2020). DOI: 10.1088/1361-6560/ab8533.

[120] G. Fattori et al. “Commissioning of an Integrated Platform for Time-Resolved Treatment Delivery in Scanned Ion Beam Therapy by Means of Optical Motion Monitoring”. In: *Technology in Cancer Research & Treatment* 13.6 (2014), pp. 517–528. DOI: 10.7785/tcrtexpress.2013.600275.

[121] G. Fattori et al. “Real-time optical tracking for motion compensated irradiation with scanned particle beams at CNAO”. In: *Nuclear Instruments and Methods in Physics Research Section A: Accelerators, Spectrometers, Detectors and Associated Equipment* 827 (2016), pp. 39–45. DOI: 10.1016/J.NIMA.2016.04.066.

[122] Chiara Paganelli et al. *“Patient-specific validation of deformable image registration in radiation therapy: Overview and caveats”*. 2018. DOI: 10.1002/mp.13162.

[123] Ye Zhang et al. “Deformable motion reconstruction for scanned proton beam therapy using on-line x-ray imaging”. In: 58.24 (2013), pp. 8621–8645. DOI: 10.1088/0031-9155/58/24/8621.

[124] Michelle Lis et al. “Dosimetric Validation of a System to Treat Moving Tumors Using Scanned Ion Beams That Are Synchronized With Anatomical Motion”. In: *Frontiers in Oncology* 11 (2021). DOI: 10.3389/fonc.2021.712126.

[125] Michelle Lis et al. “Preliminary tests of dosimetric quality and projected therapeutic outcomes of multi-phase 4D radiotherapy with proton and carbon ion beams”. In: *Physics in Medicine & Biology* 66.23 (2021), p. 235004. DOI: 10.1088/1361-6560/ac36e7.

[126] Jenny Bertholet et al. “Real-time intrafraction motion monitoring in external beam radiotherapy”. In: *Physics in Medicine & Biology* 64.15 (2019), 15TR01. DOI: 10.1088/1361-6560/ab2ba8.

[127] S. Giordanengo et al. “The CNAO dose delivery system for modulated scanning ion beam radiotherapy”. In: *Medical Physics* 42.1 (2015). DOI: 10.1118/1.4903276.

[128] M. Lis et al. “A facility for the research, development, and translation of advanced technologies for ion-beam therapies”. In: *Journal of Instrumentation* 16.03 (2021), T03004. DOI: 10.1088/1748-0221/16/03/T03004.

[129] Simona Giordanengo et al. “Commissioning operations and performances of the dose delivery system for CNAO”. In: *IEEE Nuclear Science Symposium Conference Record*. 2011. DOI: 10.1109/NSSMIC.2011.6153644.

[130] M. Seregni et al. “Motion prediction in MRI-guided radiotherapy based on interleaved orthogonal cine-MRI”. In: *Physics in Medicine and Biology* 61.2 (2016). DOI: 10.1088/0031-9155/61/2/872.

[131] Florian Friedrich et al. “Stability of conventional and machine learning-based tumor auto-segmentation techniques using undersampled dynamic radial bSSFP acquisitions on a 0.35 T hybrid MR-linac system”. In: *Medical Physics* 48.2 (2021). DOI: 10.1002/mp.14659.

[132] Marcel Van Herk et al. “The probability of correct target dosage: Dose-population histograms for deriving treatment margins in radiotherapy”. In: *International Journal of Radiation Oncology Biology Physics* 47.4 (2000). DOI: 10.1016/S0360-3016(00)00518-6.

[133] Marco Donetti et al. “Current and Future Technologies of the CNAO Dose Delivery System”. In: *IEEE Instrumentation & Measurement Magazine* 24.9 (2021), pp. 61–69. DOI: 10.1109/MIM.2021.9620025.

[134] JUN-ICHI SAITOH et al. “A Phase I Study of Hypofractionated Carbon-ion Radiotherapy for Stage III Non-small Cell Lung Cancer”. In: *Anticancer Research* 38.2 (2018), 885 LP –891.

[135] Takashi Ono et al. “Long Term Results of Single-Fraction Carbon-Ion Radiotherapy for Non-small Cell Lung Cancer”. In: *Cancers 2021, Vol. 13, Page 112* 13.1 (2020), p. 112. DOI: 10.3390/CANCERS13010112.

[136] Julia M. Pakela et al. “Management of Motion and Anatomical Variations in Charged Particle Therapy: Past, Present, and Into the Future”. In: *Frontiers in Oncology* 0 (2022), p. 629. DOI: 10.3389/FONC.2022.806153.

[137] Vicki Trier Taasti et al. “Treatment planning and 4D robust evaluation strategy for proton therapy of lung tumors with large motion amplitude”. In: *Medical Physics* 48.8 (2021), pp. 4425–4437. DOI: 10.1002/mp.15067.

[138] Shinichiro Mori et al. “Systematic evaluation of four-dimensional hybrid depth scanning for carbon-ion lung therapy”. In: *Medical Physics* 40.3 (2013), p. 031720. DOI: 10.1118/1.4792295.

[139] Shinichiro Mori et al. “A serial 4DCT study to quantify range variations in charged particle radiotherapy of thoracic cancers”. In: *Journal of Radiation Research* 55.2 (2014). DOI: 10.1093/jrr/rrt114.

[140] John Gordon Eley et al. “Robustness of target dose coverage to motion uncertainties for scanned carbon ion beam tracking therapy of moving tumors”. In: *Physics in Medicine and Biology* 60.4 (2015), pp. 1717–1740. DOI: 10.1088/0031-9155/60/4/1717.

[141] Daniel A. Low et al. “A technique for the quantitative evaluation of dose distributions”. In: *Medical Physics* 25.5 (1998), pp. 656–661. DOI: 10.1118/1.598248.

[142] Arie Van t. Riet et al. “A conformation number to quantify the degree of conformality in brachytherapy and external beam irradiation: Application to the prostate”. In: 37.3 (1997), pp. 731–736. DOI: 10.1016/S0360-3016(96)00601-3.

[143] Amit Sawant et al. “Investigating the feasibility of rapid MRI for image-guided motion management in lung cancer radiotherapy”. In: *BioMed Research International* 2014 (2014). DOI: 10.1155/2014/485067.

[144] Robert Lüchtenborg et al. “Experimental verification of a real-time compensation functionality for dose changes due to target motion in scanned particle therapy”. In: *Medical Physics* 38.10 (2011), pp. 5448–5458. DOI: 10.1118/1.3633891.

[145] Christian Schoemers et al. “The intensity feedback system at Heidelberg Ion-Beam Therapy Centre”. In: *Nuclear Instruments and Methods in Physics Research Section A: Accelerators, Spectrometers, Detectors and Associated Equipment* 795 (2015), pp. 92–99. DOI: 10.1016/J.NIMA.2015.05.054.

[146] Edoardo Mastella et al. “4D strategies for lung tumors treated with hypofractionated scanning proton beam therapy: Dosimetric impact and robustness to interplay effects”. In: *Radiotherapy and Oncology* 146 (2020). DOI: 10.1016/j.radonc.2020.02.025.

[147] Giuseppe Magro et al. “FRoG dose computation meets Monte Carlo accuracy for proton therapy dose calculation in lung”. In: *Physica Medica* 86 (2021), pp. 66–74. DOI: 10.1016/j.ejmp.2021.05.021.

[148] Franciska Lebbink et al. “The Influence of Motion on the Delivery Accuracy When Comparing Actively Scanned Carbon Ions versus Protons at a Synchrotron-Based Radiotherapy Facility”. In: *Cancers* 14.7 (2022). DOI: 10.3390/cancers14071788.

[149] Daniel Richter et al. “Residual motion mitigation in scanned carbon ion beam therapy of liver tumors using enlarged pencil beam overlap”. In: *Radiotherapy and Oncology* 113.2 (2014). DOI: 10.1016/j.radonc.2014.11.020.

[150] Pu Huang et al. “2D ultrasound imaging based intra-fraction respiratory motion tracking for abdominal radiation therapy using machine learning”. In: *Physics in Medicine & Biology* 64.18 (2019), p. 185006. DOI: 10.1088/1361-6560/ab33db.

[151] Giorgia Meschini et al. “Time-resolved MRI for off-line treatment robustness evaluation in carbon-ion radiotherapy of pancreatic cancer”. In: *Medical Physics* (2022). DOI: 10.1002/MP.15510.

[152] Jenny Dueck et al. “Robustness of the Voluntary Breath-Hold Approach for the Treatment of Peripheral Lung Tumors Using Hypofractionated Pencil Beam Scanning Proton Therapy”. In: *International Journal of Radiation Oncology*Biology*Physics* 95.1 (2016), pp. 534–541. DOI: 10.1016/J.IJROBP.2015.11.015.

[153] Emma Colvill et al. “A dosimetric comparison of real-time adaptive and non-adaptive radiotherapy: A multi-institutional study encompassing robotic, gimbaled, multileaf collimator and couch tracking”. In: *Radiotherapy and Oncology* 119.1 (2016), pp. 159–165. DOI: 10.1016/j.radonc.2016.03.006.

[154] John Gordon Eley et al. “4D optimization of scanned ion beam tracking therapy for moving tumors”. In: *Physics in Medicine and Biology* 59.13 (2014), pp. 3431–3452. DOI: 10.1088/0031-9155/59/13/3431.

[155] Paige A. Taylor, Stephen F. Kry, and David S. Followill. “Pencil Beam Algorithms Are Unsuitable for Proton Dose Calculations in Lung”. In: *International Journal of Radiation Oncology Biology Physics* 99.3 (2017). DOI: 10.1016/j.ijrobp.2017.06.003.

[156] Athena Evalour Simbahon Paz et al. “Compensating for beam modulation due to microscopic lung heterogeneities in carbon ion therapy treatment planning”. In: *Medical Physics* 48.12 (2021). DOI: 10.1002/mp.15292.

[157] Timo Steinsberger et al. “Presentation: PTC58-0207 RBE-weighted non-linear 4D-doses on CT-sequences depicting irregular motion”. In: *Proceedings to the 58th Annual Conference of the Particle Therapy Cooperative Group (PTCOG58)*. Vol. 6. 4. Manchester: International Journal of Particle Therapy, 2020, pp. 45–491. DOI: 10.14338/IJPT.19-PTCOG-6.4.

[158] Timo Steinsberger et al. “Poster: P 097 Experimental validation of a 4D dose calculation algorithm for irregular motion in carbon ion therapy”. In: *Proceedings to the 2020 Online Conference of the Particle Therapy Cooperative Group (PTCOG2020Online)*. Vol. 7. 4. Online: International Journal of Particle Therapy, 2021, pp. 74–199. DOI: 10.14338/IJPT.20-PTCOG-7.4.

[159] Timo Steinsberger et al. “Presentation: V9 Zeitaufgelöste experimentelle Validierung eines 4D Dosisberechnungsalgorithmus für unregelmäßige Bewegungen in der Kohlenstoffionentherapie”. In: *51. Jahrestagung der Deutschen Gesellschaft für Medizinische Physik (DGMP) : Abstractband*. Online, 2020, p. 37.

[160] Timo Steinsberger et al. “Presentation: 3D dose verification for Carbon Ion beams with an EBT3 Gafchromic film stack”. In: *59th Annual Conference of the Particle Therapy Co-operative Group*. Online, 2021.

List of Figures

List of Tables

Publications related to this thesis

Peer-reviewed first author publications

- Timo Steinsberger et al. “Extension of RBE-weighted 4D particle dose calculation for non-periodic motion”. In: *Physica Medica* 91 (2021), pp. 62–72. DOI: 10.1016/j.ejmp.2021.10.009

Submitted first author publications

- Timo Steinsberger et al. ”Experimental validation of an online adaptive 4D-optimized particle radiotherapy approach to treat irregularly moving tumors”. Submitted to: *International Journal of Radiation Oncology · Biology · Physics* (2022)

Co-authorship on peer-reviewed publications

- Michelle Lis et al. “A modular dose delivery system for treating moving targets with scanned ion beams: Performance and safety characteristics, and preliminary tests”. In: *Physica Medica* 76 (2020), pp. 307–316. DOI: 10.1016/j.ejmp.2020.07.029
- Michelle Lis et al. “A Modular System for Treating Moving Anatomical Targets With Scanned Ion Beams at Multiple Facilities: Pre-Clinical Testing for Quality and Safety of Beam Delivery”. In: *Frontiers in Oncology* 11 (2021). DOI: 10.3389/fonc.2021.620388
- Michelle Lis et al. “Dosimetric Validation of a System to Treat Moving Tumors Using Scanned Ion Beams That Are Synchronized With Anatomical Motion”. In: *Frontiers in Oncology* 11 (2021). DOI: 10.3389/fonc.2021.712126
- Michelle Lis et al. “Preliminary tests of dosimetric quality and projected therapeutic outcomes of multi-phase 4D radiotherapy with proton and carbon ion beams”. In: *Physics in Medicine & Biology* 66.23 (2021), p. 235004. DOI: 10.1088/1361-6560/ac36e7
- Marco Donetti et al. “Current and Future Technologies of the CNAO Dose Delivery System”. In: *IEEE Instrumentation & Measurement Magazine* 24.9 (2021), pp. 61–69. DOI: 10.1109/MIM.2021.9620025
- Daria Boscolo et al. “Radioactive Beams for Image-Guided Particle Therapy: The BARB Experiment at GSI”. in: *Frontiers in Oncology* 11 (2021). DOI: 10.3389/fonc.2021.737050

Presented first author conference contributions

- Timo Steinsberger et al. “Presentation: PTC58-0207 RBE-weighted non-linear 4D-doses on CT-sequences depicting irregular motion”. In: *Proceedings to the 58th Annual Conference of the Particle Therapy Cooperative Group (PTCOG58)*. Vol. 6. 4. Manchester: International Journal of Particle Therapy, 2020, pp. 45–491. DOI: 10.14338/IJPT.19-PTCOG-6.4

- Timo Steinsberger et al. “Presentation: Simultaneous cancer treatment and online imaging with radioactive ion beams at FAIR”. in: *1st International Biophysics Collaboration Meeting*. Darmstadt, 2019
- Timo Steinsberger et al. “Poster: P 097 Experimental validation of a 4D dose calculation algorithm for irregular motion in carbon ion therapy”. In: *Proceedings to the 2020 Online Conference of the Particle Therapy Cooperative Group (PTCOG2020Online)*. Vol. 7. 4. Online: International Journal of Particle Therapy, 2021, pp. 74–199. DOI: 10.14338/IJPT.20-PTCOG-7.4
- Timo Steinsberger et al. “Presentation: V9 Zeitaufgelöste experimentelle Validierung eines 4D Dosisberechnungsalgorithmus für unregelmäßige Bewegungen in der Kohlenstoffionentherapie”. In: *51. Jahrestagung der Deutschen Gesellschaft für Medizinische Physik (DGMP) : Abstractband*. Online, 2020, p. 37
- Timo Steinsberger et al. “Presentation: 3D dose verification for Carbon Ion beams with an EBT3 Gafchromic film stack”. In: *59th Annual Conference of the Particle Therapy Co-operative Group*. Online, 2021

Accepted first author conference contributions

- Timo Steinsberger et al. ”Poster discussion PD-0238 Experimental demonstration of conformal carbon ion therapy for irregularly moving tumors”, to be presented at: *ESTRO 2022*. Kopenhagen, 2022
- Timo Steinsberger et al. ”Experimental demonstration of conformal carbon ion therapy for irregularly moving tumors”, to be presented at: ”*60th Annual Conference of the Particle Therapy Co-operative Group (PTCOG60)*”. Miami, 2022

Acknowledgements

At the very end of this thesis, I want to add a few personal words to thank all the people who supported my during my PhD. The results presented in this thesis are the outcome of three and a half years of work in a field, I was completely new to. It contains a lot of data from experiments that were performed under the high pressure of limited beamtime and that required contributions from treatment planning, experimental hardware, data collection and analysis, and finally, of writing. Even though I had my own, clearly delimited PhD project, especially conducting experiments is always a team effort. I really hope that I could give everyone a reasonable amount in return for the support that I received. Because of those reasons, I have to thank all the people, who supported me during those years.
First of all, I have to thank my group leader Christian Graeff for his close supervision. I learned so much from you. Thank you for encouraging and advicing me and helping me to keep more or less cool during the exciting beamtimes.
Next, I need to thank Marco Durante for accepting me as a PhD student and organizing the financial support. Thank you for your advice and for sharing your experience. Thank you also to Marco Riboldi for your advice during our PhD committee meetings and for being the second referee.
All the work would not have been possible without my wonderful colleagues who fill this group with live. This was of special importance during the Covid-19 pandemic. They helped my with their skills, advice, and inspiration to obtain the presented results. As you are all important and I cannot rank your help in any reasonable way, I will simply address you in alphabetical order. Thank you Athena Paz for helping me to keep my head up during our time in a common office and our inspiring discussions. Many thanks to Christoph Hartmann-Sauter who maintains the DDS hardware and interfaces at GSI. The provided simulation environment for the DDS was a necessary tool for debugging of the code. Thank you Lennart Volz for supporting me during the writing process. Michelle Lis, you showed me how to take the lead during beamtimes. This teached me a lesson for live. Many thanks go to Moritz Wolf for his help with treatment planning and batch skripting of the dose reconstructions. Many thanks also to Yinxiangzi 'Joey' Sheng for his helpful clinical perspective.
The implementation of MP4DRT into the DDS and the performance of experiments at CNAO was only possible thanks to our local contact person Marco Donetti. Thank you for supervision my modifications of the DDS code and for helping during the tough night shifts.
I want to thank Elko Schubert and the GSI workshop for manufacturing components of the experimental setups used for this thesis and Christoph Schuy providing the IC array detector.
I am also were grateful for all the paperwork done in the background, that helped me to focus on my research. Here, the most important persons are Martine Kräckmann, who was my contact person for all organizational questions at TU Darmstadt, and her counterparts at GSI, which are Corinna Kausch and Maria Didonna-Schnellbächer.

Of course, this work also profited from the backing I received outside of my working environment. A huge thanks goes to my parents who supported me during all my studies.
And last but not least there is Inga. Thank you so much for always being there when I need you. You are simply wonderful.

Erklärungen laut Promotionsordnung

§ 8 Abs. 1 lit. c PromO

Ich versichere hiermit, dass die elektronische Version meiner Dissertation mit der schriftlichen Version übereinstimmt.

§ 8 Abs. 1 lit. d PromO

Ich versichere hiermit, dass zu einem vorherigen Zeitpunkt noch keine Promotion versucht wurde. In diesem Fall sind nähere Angaben über Zeitpunkt, Hochschule, Dissertationsthema und Ergebnis dieses Versuchs mitzuteilen.

§ 9 Abs. 1 PromO

Ich versichere hiermit, dass die vorliegende Dissertation selbstständig und nur unter Verwendung der angegebenen Quellen verfasst wurde.

§ 9 Abs. 2 PromO

Die Arbeit hat bisher noch nicht zu Prüfungszwecken gedient.

Darmstadt, 5. Mai 2022

T. Steinsberger